Technical Physics Letters, Vol. 30, No. 5, 2004, pp. 349–350. Translated from Pis'ma v Zhurnal Tekhnicheskoĭ Fiziki, Vol. 30, No. 9, 2004, pp. 1–5.

Stibnite–Liquid Crystal Structure: A Strongly Nonlinear Reversible Recording Medium

L. P. Amosova, I. E. Morichev, N. I. Pletneva, and A. N. Chaika*

Vavilov Optical Institute, State Scientific Center of the Russian Federation, St. Petersburg, 190164 Russia

** e-mail: chaika@rbcmail.ru*

Received October 16, 2003

Abstract—It is shown that stibnite can be used as a material for the photosensitive layer in an optically controlled structure of the photosemiconductor–liquid crystal type. The spectral characteristic of stibnite allows a highly sensitive recording medium to be obtained for writing holograms using He–Ne laser radiation. The maximum diffraction efficiency achieved with this medium was 37%. The modulation characteristic of the stibnite–liquid crystal structure exhibits pronounced nonlinearity, with the slope of both rising and falling regions being dependent on the applied bias voltage. © *2004 MAIK "Nauka/Interperiodica".*

The task of creating a medium for the reversible recording of holograms with a nonlinear modulation characteristic is essentially opposite to the traditional trend of ensuring maximum linearity of a holographic recording medium. The need for a new medium is related to the use of a holographic correlator for constructing fuzzy algebra algorithms in artificial intelligence simulations. This requires a medium suitable for writing Fourier holograms and possessing nonlinear properties [1]. Previously [2], it was demonstrated that such media are offered by optically controlled structures of the photosemiconductor (PSC)–nematic liquid crystal (LC) type with a planar initial orientation. In these structures, the modulation characteristic, representing the dependence of the diffraction efficiency on the recording light intensity in the first order of diffraction, has a substantially nonlinear shape with rising and falling regions, provided that the phase modulation depth is sufficiently large.

This study was aimed at evaluating the possibility of obtaining an optically controlled structure of the PSC–LC type using stibnite (Sb_2S_3) as a semiconductor material for the photosensitive layer. Stibnite was never used for this purpose before, but the rather high resistivity of this semiconductor gave us hope to match its impedance with that of an LC layer so as to obtain a resolution acceptable for the problem under consideration. At the same time, coincidence of the position of the spectral sensitivity maximum with the wavelength of recording He–Ne laser radiation could provide for the phase modulation depth required for realization of the nonlinear modulation characteristic with clearly pronounced rising and falling branches at sufficiently large recording radiation intensities.

A high optical quality of the stibnite layer is provided by strict temperature control during thermal deposition. The proposed sandwich structure comprises the following layers sequentially deposited onto glass substrates: 1-μm-thick PSC layer (Sb_2S_3); transparent indium tin oxide (ITO) electrodes; aligning GeO layers (obtained by oblique deposition); and a nematic LC of the ZhKM-1630B type (Δn = 0.13, $\Delta\varepsilon$ = +4.4, ΔT = –20°C…+90°C). The LC layer had a thickness of 10 μm and possessed initial planar orientation.

We have studied the behavior of the first-order diffraction efficiency as dependent on the intensity and spatial frequency of the interference pattern formed at various values of the applied bias voltage. The diffraction efficiency was defined as the ratio $\eta = I_1/I_0$, where I_1 and I_0 are the intensities of light transmitted through the structure in the first order of diffraction and in the absence of the recording light flux. The pattern of interference of two coherent light beams with plane wave fronts was formed in the PSC layer using He–Ne laser radiation (λ = 633 nm). Readout was performed at λ = 814 nm in the transmission mode. The sample structure was arranged in the optical scheme so that the LC director orientation would coincide with the polarization vector direction in the readout beam.

Figure 1 shows a plot of the maximum diffraction efficiency η versus spatial frequency ν of a holographic grating written in the sample structure. These measurements were performed in the range of spatial frequencies from 12 to 65 mm^{-1} for a dc bias voltage of 8 V. The limiting value of the diffraction efficiency in the +1 order amounted to η_{+1} = 37%, while that in the –1 order was η_{-1} = 20%. The observed asymmetry is typical of the regime of hologram recording with asymmetric line profile on structures of the PSC–LC type with initial planar orientation of the nematic LC layer [3, 4].

Figure 2 presents a series of experimental dependences of η on the intensity I_w of one of the two inter-

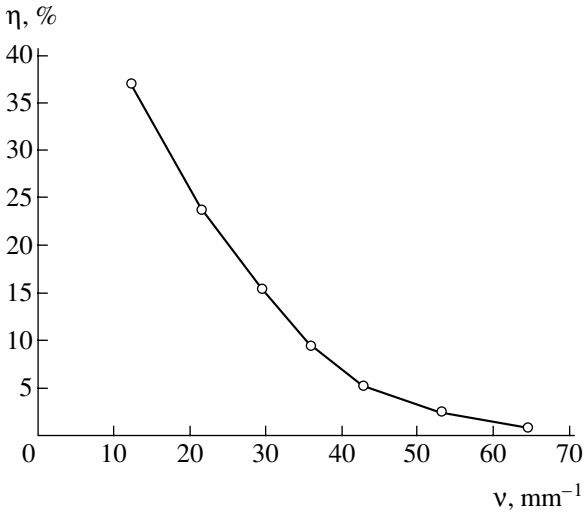

Fig. 1. A plot of the maximum diffraction efficiency η versus spatial frequency ν of a recorded holographic grating, illustrating spatial resolution of the optically controlled stibnite–nematic LC structure.

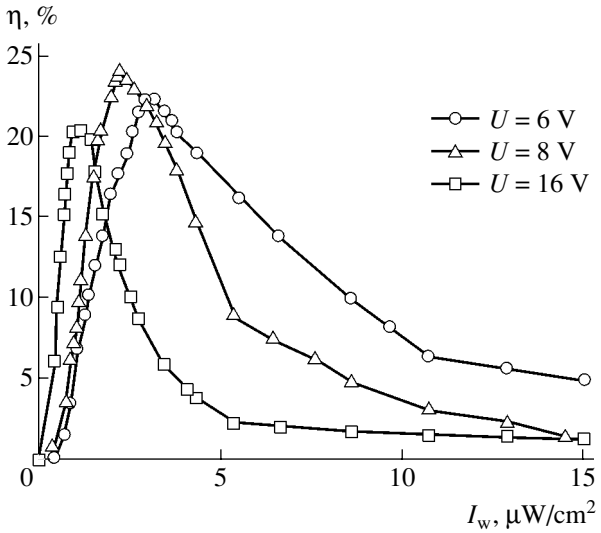

Fig. 2. Experimental dependences of the diffraction efficiency η on the writing beam intensity I_w for various dc bias voltages U, representing modulation characteristics of the optically controlled stibnite–nematic LC structure.

fering write beams for various dc bias voltages. The spatial frequency of recorded grating was 22 mm^{-1}. As can be seen, the curves have rising and falling regions in which the diffraction efficiency drops by a factor of 20 relative to the maximum value, which is evidence of a strong nonlinearity. The slope of the rising and falling branches depends on the applied voltage, which is an important factor for the optical implementation of fuzzy algebra algorithms. For the PSC–LC structures studied, the sensitivity determined on a level of $0.9\eta_{max}$ varied within 0.75–2.5 μW/cm^2.

The operation speed is determined by the electrooptical response time of the nematic LC and the time constant of the PSC–LC structure. We used a PSC material possessing a relatively low level of resistivity. In particular, it was almost ten times as small as that of $As_{10}Se_{90}$ studied previously [2]: 10^{12} versus 10^{13} Ω cm, respectively. The relatively large time constant of the structures studied was related to the presence of a considerable number of vacant states (traps) with large relaxation times at the stibnite–LC interface. On the other hand, it is the presence of these traps and the resulting large time constant that accounts for the good spatial resolution. Indeed, the spatial resolution is better than could be expected for a semiconductor with the given resistivity: the traps prevent a potential relief from blurring.

Another factor leading to an increase in the time constant of the PSC–LC structure studied is the need for obtaining a phase shift of 2π at a given readout radiation wavelength (814 nm). This required a relatively large LC layer thickness (in our case, no less than 6.5 μm [5]), while the operation speed is inversely proportional to the square of this value. For a dc bias voltage of 8 V, the experimentally determined switch-on time was 120 ms (at a switch-off time of 800 ms).

Acknowledgments. This study was supported by the Ministry of Education of the Russian Federation, project no. E02-20-61.

REFERENCES

1. A. V. Pavlov, Opt. Spektrosk. **90**, 515 (2001) [Opt. Spectrosc. **90**, 452 (2001)].
2. A. N. Chaika and F. L. Vladimirov, Pis'ma Zh. Tekh. Fiz. **26** (4), 9 (2000) [Tech. Phys. Lett. **26**, 139 (2000)].
3. N. L. Ivanova, A. P. Onokhov, and A. N. Chaika, Pis'ma Zh. Tekh. Fiz. **27** (16), 57 (2001) [Tech. Phys. Lett. **27**, 647 (2001)].
4. V. A. Berenberg, A. N. Chaika, N. L. Ivanova, *et al.*, Proc. SPIE **4493**, 239 (2002).
5. L. M. Blinov, *Electro-Optical and Magneto-Optical Properties of Liquid Crystals* (Nauka, Moscow, 1978; Wiley, New York, 1983).

Translated by P. Pozdeev

Technical Physics Letters, Vol. 30, No. 5, 2004, pp. 351–353. Translated from Pis'ma v Zhurnal Tekhnicheskoĭ Fiziki, Vol. 30, No. 9, 2004, pp. 6–11.

Theory of Magnetoelectric Effect in Ferrite–Piezoelectric Hybrid Composites

D. A. Filippov

Novgorod State University, Novgorod, Russia

e-mail: fdma@novsu.ac.ru

Received November 3, 2003

Abstract—A theory of the magnetoelectric (ME) effect in a multilayer ferrite-piezoelectric hybrid composite is presented. Proceeding from the material equations and the equations of motion, an expression for the frequency dependence of the ME voltage coefficient is obtained which involves the parameters of the ferrite and piezoelectric phases. In the region of the electromechanical resonance of the composite, the ME voltage coefficient exhibits a sharp increase. The results of calculations for a Terfenol-D–PZT hybrid composite are in satisfactory agreement with experimental data. © *2004 MAIK "Nauka/Interperiodica".*

Multilayer magnetoelectric composites comprise alternating layers of magnetostrictive (ferrite) and piezoelectric components. The thicknesses of these layers are typically much smaller than the characteristic spatial scales of external factors, which allows such materials to be characterized by effective macroscopic parameters [1]. These materials exhibit a magnetoelectric (ME) effect related to the mechanical interaction of ferrite and piezoelectric subsystems. In a magnetic field, the ferrite component exhibits magnetostriction that gives rise to mechanical stresses. Transferred to the piezoelectric phase, these mechanical stresses induce polarization due to the piezoeffect.

The magnitude of the ME effect significantly increases in the region of the electromechanical resonance [2–6]. Recently [5, 6], a theory of this phenomenon was developed using an approach based on the effective parameters of a composite and experimentally verified using samples in the form of disks and plates. This theory is applicable when the material can be considered as a homogeneous medium, that is, when the layer thickness in a multilayer structure or the grain size in a bulk composite is much smaller than the wavelength of sound.

Wan *et al*. [4] presented the results of measurements of the ME voltage coefficient for a hybrid composite representing a mechanical mixture of the magnetostrictive composite based on Terfenol-D and the piezoelectric component based on lead zirconate titanate (PZT) (Fig. 1). The dimensions of the ferrite and PZT phase plates were 6.8 (length) × 6.2 × 0.7 mm and 9.1 (length) × 6.2 × 0.7 mm, respectively. This composite cannot be considered as a homogeneous medium and, hence, the aforementioned theory is inapplicable. The results of numerical modeling of the ME effect in such a hybrid composite structure [6] showed that the ME voltage coefficient exhibits an increase in the vicinity of the electromechanical resonance. However, a relationship between the resonance frequency and the ME voltage coefficient, on the one hand, and the material parameters, on the other hand, was not established.

This Letter presents a theoretical model in which an expression for the ME voltage coefficient of a hybrid composite through the parameters of the magnetostrictive and piezoelectric components is obtained and the frequency dependence of this value is analyzed.

Consider a model of the ferrite-piezoelectric hybrid composite comprising a thin magnetostrictive plate of length L_1 glued to a piezoelectric plate of length L_2 (Fig. 1). The thickness of a junction layer is assumed to be negligibly small. The top and bottom surfaces of the piezoelectric plate bear thin metal contacts. Let the sample be polarized along the normal to the contact planes (parallel to the Z axis). Magnetic fields (a static bias magnetic field and an alternating field with a frequency of ω) are perpendicular to the polarization direction (i.e., parallel to the X axis). Due to magnetostriction, the alternating magnetic field induces oscillations in the ferrite phase that propagate both in depth and in plane of the plate. In what follows, we will consider only oscillations of the lowest frequency, that is,

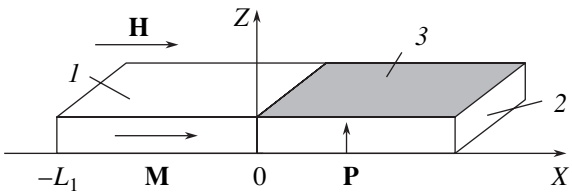

Fig. 1. A schematic diagram of the hybrid composite structure: (*1*) magnetic component; (*2*) piezoelectric component; (*3*) electrode. The arrows **P**, **M**, and **H** show the directions of the polarization, magnetization, and alternating magnetic field, respectively.

1063-7850/04/3005-0351$26.00 © 2004 MAIK "Nauka/Interperiodica"

the volume oscillations propagating along the plate. Reaching the interface, these mechanical oscillations are transmitted to the piezoelectric phase, where the piezoeffect leads to polarization, that is, to the appearance of an electric field.

It is assumed that the plate thickness and width are much smaller than its length. The faces of the plate are free; therefore, the surface stresses are equal to zero. Since the plate is thin and narrow, the stress tensor components T_2 and T_3 are assumed to be zero not only on the surfaces but throughout the volume. Thus, the only nonzero component is T_1. In addition, since the top and bottom faces of the piezoelectric plate are equipotential surfaces, the only nonzero component of the electric field intensity vector is E_z.

For the given field orientation, equations for the strain tensor ${}^mS_i$ in the magnetostrictive plate and for the strain tensor ${}^pS_i$ and the electric induction D_i in the piezoelectric plate can be written as

$$ {}^mS_1 = {}^ms_{11}{}^mT_1 + q_{11}H_1, \tag{1} $$

$$ {}^pS_1 = {}^ps_{11}{}^pT_1 + d_{31}E_3, \tag{2} $$

$$ D_3 = {}^p\varepsilon_{33}E_3 + d_{31}{}^pT_1, \tag{3} $$

where ${}^ms_{11}$ and ${}^ps_{11}$ are the components of the compliance tensors of the magnetic and piezoelectric materials, respectively; ${}^p\varepsilon_{33}$ are the components of the permittivity tensor; and d_{31} and q_{11} are the piezoelectric and piezomagnetic coefficients, respectively.

Expressing the stress components via the strain components and substituting these expressions into the equation of motion of the medium, we obtain differential equations for the x projections of the displacement vectors of the magnetic (${}^mu_x$) and piezoelectric (${}^pu_x$) media. A solution to these equations can be found in the following form:

$$ \begin{aligned} {}^mu_x(x) &= A_1\cos({}^mkx) + B_1\sin({}^mkx), \\ {}^pu_x(x) &= A_2\cos({}^pkx) + B_2\sin({}^pkx), \end{aligned} \tag{4} $$

where ${}^mk = \omega({}^m\rho{}^ms_{11})^{1/2}$, ${}^pk = \omega({}^p\rho{}^ps_{11})^{1/2}$, and ${}^m\rho$ and ${}^p\rho$ are the densities of the magnetic and piezoelectric components, respectively. The constant coefficients A_1, A_2, B_1, and B_2 are determined from the boundary conditions. Assuming the contact between phases to be ideal and the left-hand end face of the magnetic plate and the right-hand end face of the piezoelectric phase to be free, the boundary conditions can be formulated as

$$ \begin{aligned} {}^mu_x(0) &= {}^pu_x(0), \quad {}^mT_1(0) = {}^pT_1(0), \\ {}^mT_1(-L_1) &= 0, \quad {}^pT_1(L_2) = 0. \end{aligned} \tag{5} $$

The electric field strength in the piezoelectric phase is determined from Eq. (3) using the open circuit condition,

$$ \int_0^W dy \int_0^{L_2} D_3(x)dx = 0, \tag{6} $$

where W is the sample width.

Expressing the stress tensor components in Eq. (2) via the strain tensor components, using a solution for ${}^pu_x$, and substituting these expressions into Eq. (3) and the resulting expression for D_3 into Eq. (6), we obtain an equation for E_z. Defining the magnetoelectric voltage coefficient $\alpha_{E,t}$ via the relation $E_3 = \alpha_{E,t}H_1$, we obtain the expression

$$ \alpha_E = \frac{d_{31}q_{11}}{{}^p\varepsilon_{33}{}^ms_{11}\Delta_a}\frac{\tan(\kappa_2/2)}{\kappa_2}\frac{1}{1-\cos(\kappa_1)}, \tag{7} $$

where

$$ \begin{aligned} \Delta_a = (1-K_{31}^2)\left(1+\frac{\tan(\kappa_2/2)}{\kappa_2}\right)\left(1+\gamma\frac{\tan(\kappa_1)}{\tan(\kappa_2)}\right) \\ +\left(1+\gamma\frac{\tan(\kappa_1)}{\sin(\kappa_2)}\right)\frac{\tan(\kappa_2/2)}{\kappa_2}. \end{aligned} \tag{8} $$

Here, $\kappa_1 = {}^mkL_1$, $\kappa_2 = {}^pkL_2$, $\gamma = ({}^m\rho{}^ps_{11}/{}^p\rho{}^ms_{11})^{1/2}$, and $K_{31}^2 = d_{31}^2/({}^p\varepsilon_{33}{}^ps_{11})$ is the square of the electromechanical coupling coefficient for the planar oscillations.

As can be seen from formula (7), the ME voltage coefficient exhibits a resonance growth for the frequencies corresponding to $\Delta_a = 0$. These frequencies are determined by the composite sample geometry and parameters and do not coincide with the resonance frequencies of separate magnetic and piezoelectric components. The ME voltage coefficient is proportional to the product of the piezoelectric (d_{31}) and piezomagnetic (q_{11}) moduli and inversely proportional to the permittivity ${}^p\varepsilon_{33}$ of the piezoelectric phase and the compliance modulus ${}^ms_{11}$ of the magnetic phase. Real structures always exhibit losses, which are related primarily with nonideal contacts. These losses determine the resonance line width and limit the peak value of the ME voltage coefficient. The losses can be taken into account in terms of the damping coefficient by representing k or ω as a complex quantity [7]. Let us use the second way and represent the circular frequency as $\omega = \omega' + i\chi$, where χ is the damping factor determined from the experimental resonance line width.

In order to obtain quantitative estimates, let us use the parameters of a composite studied in [4]. Expressing the compliance moduli via the elastic moduli, we obtain the following values: magnetic phase, ${}^ms_{11} = 0.454 \times 10^{-10}$ m^2/N, $q_{11} = 19.7 \times 10^{-10}$ m/A, ${}^m\rho = 9200$ kg/m^3, $L_1 = 7$ mm; piezoelectric phase, ${}^ps_{11} =$

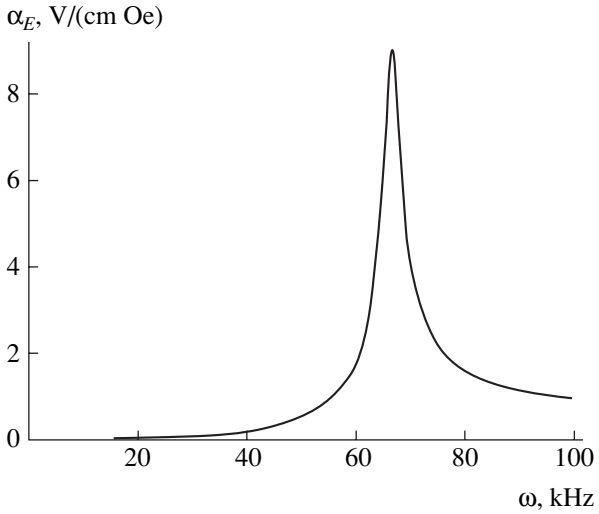

Fig. 2. Frequency dependence of the ME voltage coefficient calculated for a damping coefficient of $\chi = 10000\ s^{-1}$.

0.178×10^{-10} m^2/N, $d_{31} = -1.82 \times 10^{-10}$ m/V, ${}^p\rho = 7700$ kg/m^3, ${}^p\varepsilon_{33} = 1800$, $L_2 = 9.1$ mm. Figure 2 shows a theoretical dependence of the ME voltage coefficient calculated using formula (7). There is a very good agreement, both qualitative and quantitative, between theory and the experimental data reported in [4]. At a frequency of 65 kHz, the ME effect exhibits a resonance growth, whereby the ME voltage coefficient reaches almost 10 V/(cm Oe). This value is three orders of magnitude greater than that at 10 kHz. Harmonics of the second, third, and higher orders are observed at the multiple frequencies. If the effect were due only to a resonance in the piezoelectric phase, the growth would be observed at a frequency of 190 kHZ, whereas the resonance frequency of the magnetic phase is 130 kHz. Therefore, the resonance growth of the ME voltage coefficient predicted by the theory and observed in experiment is related to the electromechanical resonance in the whole sample.

Thus, a hybrid composite based on a magnetostrictive ferrite and a piezoelectric component exhibits a resonance increase in the ME effect. The resonance frequency is determined by the geometry and parameters of both ferrite and piezoelectric phases. The peak value of the ME voltage coefficient is several orders of magnitude greater than the low-frequency value.

Acknowledgments. The author is grateful to M.I. Bichurin and G. Srinivasan for fruitful discussions of results.

This study was supported in part by the Ministry of Education of the Russian Federation (project no. E02-3.4-278) and the Program “Universities of Russia” (project no. UR 01.01.007).

REFERENCES

1. M. I. Bichurin, V. M. Petrov, and G. Srinivasan, J. Appl. Phys. **92**, 7681 (2002).
2. M. I. Bichurin, D. A. Filippov, V. M. Petrov, and G. Srinivasan, in *Proceedings of the International Conference on Physics of Electron Materials, Kaluga, 2002*, p. 309.
3. D. A. Filippov, M. I. Bichurin, V. M. Petrov, and G. Srinivasan, Bull. Am. Phys. Soc. **48**, 214 (2003).
4. J. G. Wan, J.-M. Liu, H. L. W. Chand, *et al.*, J. Appl. Phys. **93**, 9916 (2003).
5. M. I. Bichurin, D. A. Filippov, V. M. Petrov, *et al.*, Phys. Rev. B **68**, 132408 (2003).
6. D. A. Filippov, M. I. Bichurin, V. M. Petrov, *et al.*, Pis’ma Zh. Tekh. Fiz. **30**, 15 (2004) [Tech. Phys. Lett. **30**, 6 (2004)].
7. R. Truell, C. Elbaum, and B. B. Chick, *Ultrasonic Methods in Solid State Physics* (Academic Press, New York, 1969; Mir, Moscow, 1972).

Translated by P. Pozdeev

Technical Physics Letters, Vol. 30, No. 5, 2004, pp. 354–357. Translated from Pis'ma v Zhurnal Tekhnicheskoĭ Fiziki, Vol. 30, No. 9, 2004, pp. 12–20.

The Velocity of Streamer Propagation toward Anode and Cathode in He, Xe, N_2, and SF_6

S. I. Yakovlenko

Institute of General Physics, Russian Academy of Sciences, Moscow, 117924 Russia

Received November 10, 2003

Abstract—A simple mechanism of ionization spreading in a dense gas, based on the background electron multiplication wave in an inhomogeneous electric field, is considered. This process is independent of the sign of the field projection onto the direction of propagation. An analytical expression for the velocity of the ionization front propagation is obtained, which agrees well with the results of numerical calculations performed using both the simple background electron multiplication model and a detailed diffusion-drift theory. The ionization wave front velocity as a function of the field strength at the streamer boundary has been tabulated for He, Xe, N_2, and SF_6. Some peculiarities observed in the motion of streamers, such as the velocity jerks, can be related to the recently discovered nonmonotonic dependence of the ionization rate on the field strength. © *2004 MAIK "Nauka/Interperiodica".*

Introduction

As is known, streamers are formed in a dense gas from an electron avalanche, whereby the electron density increases so that the external electric field begins to concentrate on the plasma [1–7]. Despite being investigated for a long time, the mechanism of streamer propagation is still incompletely clear and many recent works have been devoted to the numerical simulation of streamers (see, e.g., [8–13] and references therein).

The propagation of streamers toward the anode is usually related to the drift of electrons on the streamer front. However, the existence of streamers propagating toward the cathode is rather intriguing. At present, this phenomenon is conventionally treated within the framework of the Meek–Loeb–Raether photon hypothesis [1–7]. According to this, photons emitted from the streamer head produce ionization of the gas in front of this moving boundary. The photoionization events give rise to the avalanche process directed to the head. Overlapping avalanches provide for the streamer propagation toward the cathode. This theory was significantly refined by Lozansky and Firsov [6]. Attempts at constructing a nonphoton mechanism of streamer propagation based on the concept of Langmuir plasma oscillations were undertaken in [14, 15].

This Letter presents a quite simple nonphoton mechanism capable of ensuring the propagation of streamers in both directions.

Background Electron Multiplication Wave in an Inhomogeneous Electric Field

Simplest model. Let a small high-density plasma bunch appear between plane capacitor electrodes, such that the electric field inside this region is zero, and let the electron density around this plasma bunch be many orders of magnitude smaller than inside. Some background ionization always takes place, at least due to cosmic rays and the natural radioactivity. Simple estimates show that even a background radioactivity as small as about 10 μr/h provides for an electron density on the order of 10^3–10^4 cm^{-3}.

The proposed mechanism based on the background electron multiplication wave will be considered for the simplest model. Let us ignore the electron drift and determine the boundary between gas and streamer as the points where the plasma density reaches a certain critical value N_{cr} that provides for the complete screening of the external field. In this case, the electron density at a point with radius vector $\mathbf{r}$ at time t can be expressed as

$$N_e(\mathbf{r}, t) = \begin{cases} N_0 \exp[\nu_i(E(\mathbf{r}))t], & N_0 \exp[\nu_i(E(\mathbf{r}))t] < N_{cr}, \\ N_{cr}, & N_0 \exp[\nu_i(E(\mathbf{r}))t] \geq N_{cr}, \end{cases} \quad (1)$$

where N_0 is the background plasma density. Obviously, the propagation of the ionization front according to model (1) is independent of the sign of the field projection onto the propagation direction, since the ionization rate is determined by the modulus of the electric field strength.

Multiplication front velocity. The coordinates of the electron multiplication wave front are determined at the points where the critical electron density is reached. Consider a point with the coordinate $z(t)$ on the wave

front. Time variation of this coordinate in the normal direction is implicitly described by the expression

$$\nu_i(E_0(z(t)))t = Ln, \quad Ln \equiv \ln(N_{cr}/N_0), \tag{2}$$

where $E_0 = E(z(0))$ is the field strength on the front surface. Generally speaking, the value of Ln (together with N_{cr}) is a function of E_0. However, we will ignore this dependence possessing a logarithmic character. Taking a derivative of expression (2), we obtain for the front velocity

$$u_{fr} = \frac{dz}{dt} = \nu_i\left[\left(\frac{d\ln\nu}{d\ln E}\left|\frac{-\nabla E}{E}\right|\right)_{E=E_0} Ln\right]^{-1}. \tag{3}$$

Approximating the front surface at the streamer head by a sphere of radius r_0, we can write $|-\nabla E/E|_{E=E_0} = 2/r_0$. This yields

$$u_{fr} = \nu_i r_0\left[\left(\frac{d\ln\nu}{d\ln E}\right)_{E=E_0} 2Ln\right]^{-1}. \tag{4}$$

The ionization rate $\nu_i = \alpha_i u_{de}$ can be expressed as a product of the Townsend coefficient $\alpha_i(E, p) = p\xi(E/p)$ on the electron drift velocity $u_{de}(E/p)$, where $\xi(E/p)$ is the function characteristic of a given gas. It is important to note that the most significant characteristics of the ionization process are functions of the reduced electric field strength E/p. For this reason, the velocity of the streamer head propagation is also expressed through the universal functions of E_0/p:

$$\begin{gathered} u_{fr} = \nu_i r_0/\zeta(E_0/p), \\ \zeta(E_0/p) = 2Ln\left(\frac{d\ln(u_{de}(E/p)\xi(E/p))}{d\ln(E/p)}\right)_{E/p=E_0/p}. \end{gathered} \tag{5}$$

Note also that, as was established in [16, 17], the ionization rate $\nu_i(E/p)$ exhibits a maximum at a certain value of $E/p = (E/p)_{cr}$. This circumstance leads to some peculiarities in the ionization front propagation (see below).

Comparison to the diffusion-drift model. In order to confirm the existence of the background electron multiplication wave, various numerical calculations were performed within the framework of a one-dimensional diffusion-drift model described in detail elsewhere [19]. This model describes the ionization process developed in the region between two coaxial cylindrical electrodes, $r_0 < r < r_1$ (where r_0 and r_1 are the radii of the inner and outer cylinders, respectively), in terms of the equation of momentum transfer, equation of continuity for electrons and ions, and the Poisson equation for the electric field strength. Various quantities (ionization rates, drift velocities, diffusion coefficients) entering into the equations of the diffusion-drift model were set as functions of the field strength using approximate expressions obtained for xenon [18].

The existence of the background electron multiplication wave was demonstrated by the results of numerical calculations for an anode of small radius (i.e., for a positive potential applied to the inner electrode of radius r_0 at a zero potential on the outer electrode of radius r_1). The results of these calculations showed that a background electron multiplication wave moves in this system from anode to cathode. The values of the ionization front propagation velocity determined using the detailed diffusion-drift theory and the simple electron background multiplication model (1) differ by no more than 3%.

Background Electron Multiplication Wave Velocity in Various Gases

Helium and xenon. It is interesting to consider the ionization front propagation velocity in helium and xenon in more detail, since the ionization and drift characteristics for these gases have been thoroughly studied [16–18] and simple approximations are available. For helium [16],

$$\begin{gathered} \xi(x) = 5.4(\text{Torr})^{-1}\exp(-(14/x)^{1/2} - 1.5\times10^{-3}x), \\ u_{de} = 10^6\ (\text{cm/s})x, \end{gathered} \tag{6}$$

where $x = (E_0/p)$ (Torr cm/V). Substituting expression (6) into Eq. (5), we obtain

$$\begin{gathered} u_{fr} = \nu_i r_0/\zeta(x), \\ \zeta(x) = 2Ln(1 + 1.87x^{-1/2} - 1.5\times10^{-3}). \end{gathered} \tag{7}$$

For xenon [17, 18],

$$\xi(x) = 45(\text{Torr})^{-1}u_{de}\exp(-31.1(1/x)^{1/2} - 1.7\times10^{-4}x), \tag{8}$$

$$\begin{gathered} u_{de} = \frac{1.3x + 1.3x^6}{1 + 7.31\times10^{10}x^{5.8}} \\ + 1.3\times10^5 x\exp\left(-\frac{2.2}{x}\right)(\text{cm/s}). \end{gathered} \tag{9}$$

The validity of formula (7) was checked by direct numerical calculations for a spherically symmetric electron bunch (Fig. 1). The electron density distribution was calculated for various times using formula (1). Using these data, the corresponding values of the front radius r_{fr} at various moments were calculated and approximated by a linear dependence, the slope of which gave the front velocity. Several points determined in this way are depicted in Fig. 1.

Molecular nitrogen and SF_6. The background electron multiplication front velocity in N_2 and SF_6 was determined (Fig. 2) using the values of α_i and u_{de} tabulated in [20] and [21], respectively. The nonmonotonic

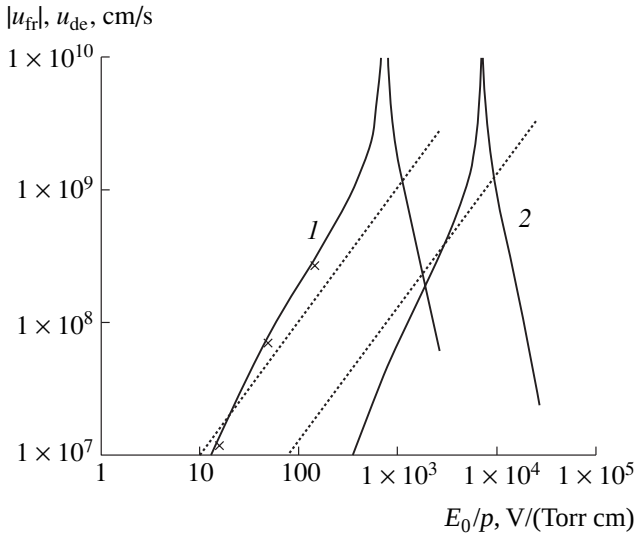

Fig. 1. Plots of the modulus of the ionization front velocity u_{fr} (solid curves) and the electron drift velocity u_{de} (dash curves) versus the reduced field strength E_0/p at the streamer surface calculated by formulas (6)–(9) using $N_{cr} = 10^{14}$ cm^{-3}, $N_0 = 10$ cm^{-3}, $r_0 = 0.5$ mm, $p = 1$ bar and data from [16–18] for (*1*) helium [$(E_0/p)_{cr} \approx 720$ V/(Torr cm)] and (*2*) xenon [$(E_0/p)_{cr} \approx 7$ kV/(Torr cm)]. Crosses show the results of numerical calculations using model (1) for helium (see the text for explanations).

dependence of the multiplication front velocity on the field strength is related to the nonmonotonic variation of the derivative of the ionization rate. This is explained by the existence of three ionization thresholds (20, 40, and 50 eV) in SF_6.

Discussion of Results

Streamer propagation velocity. The background electron multiplication wave velocities for $E_0/p < (E_0/p)_{cr}$ agree in the order of magnitude with the measured velocities of streamers (~10^7–10^9 cm/s). More detailed comparison to the experiment requires two-dimensional calculations. It should be noted that, for some values of r_0 and E_0/p, the multiplication wave velocity becomes comparable to the electron drift velocity; for the stronger fields and larger streamer head radii, the multiplication wave velocity exceeds the drift velocity (Fig. 1). Therefore, in weak fields and in the initial stage of motion of the anode streamer end, the usual ionization wave spreading by the electron drift mechanism can predominate. As the ionization process develops, the field strength at the streamer end grows because of an increase in the streamer length. For this reason, ionization due to the background electron multiplication must dominate in the late stages. As for the cathode streamer end propagation velocity, there is no ground for considering it to be equal to the electron drift velocity.

Elongation of the ionization region. The shape of the streamer head is determined by the interplay of two factors. The front velocity according to formula (7) increases with the field strength (for $E_0/p < (E_0/p)_{cr}$) and grows linearly with the curvature radius r_0. On the other hand, the field strength is greater at the points where the curvature radius is smaller. For not very strong fields such that $E_0/p < (E_0/p)_{cr}$, the velocity grows with the field strength more rapidly than by the linear law. For this reason, the streamer head top will move faster than the remote regions. Therefore, the ionization region for $E_0/p < (E_0/p)_{cr}$ will elongate. It should be noted, however, that the minimum radius of curvature r_0 is limited from below, because the above considerations are valid for $\alpha_i r_0 \gg 1$.

The field strength at the streamer head increases with its length. Accordingly, the streamer propagation velocity must also increase with the streamer length—in agreement with experiment [6].

Infinite and negative velocities. According to expressions (5), the background multiplication front velocity becomes infinite for $E_0/p = (E_0/p)_{cr}$. Since the multiplication wave does not carry information in the direction of wave propagation, this velocity can, formally speaking, be supraluminal. However, the delay in the external field screening (ignored above) will restrict this velocity in some cases to the light speed.

For $E_0/p > (E_0/p)_{cr}$, the background multiplication front should move in the direction opposite to that of the field gradient. Therefore, at a certain distance from the front (where the field strength decreases so that $E_0/p = (E_0/p)_{cr}$), an ionization region has to arise and move in both directions. As a result, the streamer velocity will exhibit jerks. Nonmonotonic features in the ionization rate as a function of the field strength (Fig. 2b) must also lead to instabilities in the streamer motion.

Conclusions

We have considered a simple mechanism of ionization spreading in a dense gas, which is independent of the sign of the field projection onto the direction of propagation. This mechanism is related to the difference in the rate of background electron multiplication at various points in an inhomogeneous electric field. The streamer motion, as is commonly accepted, is determined by the electric field concentration at its head. Proceeding from a simple equation taking into account the background electron multiplication, we obtained an analytical expression for the ionization front velocity. This expression agrees well with the results of numerical calculations performed using both the simple background electron multiplication model and a detailed diffusion-drift theory. The ionization wave front velocity as a function of the field strength at the streamer boundary has been tabulated for He, Xe, N_2, and SF_6.

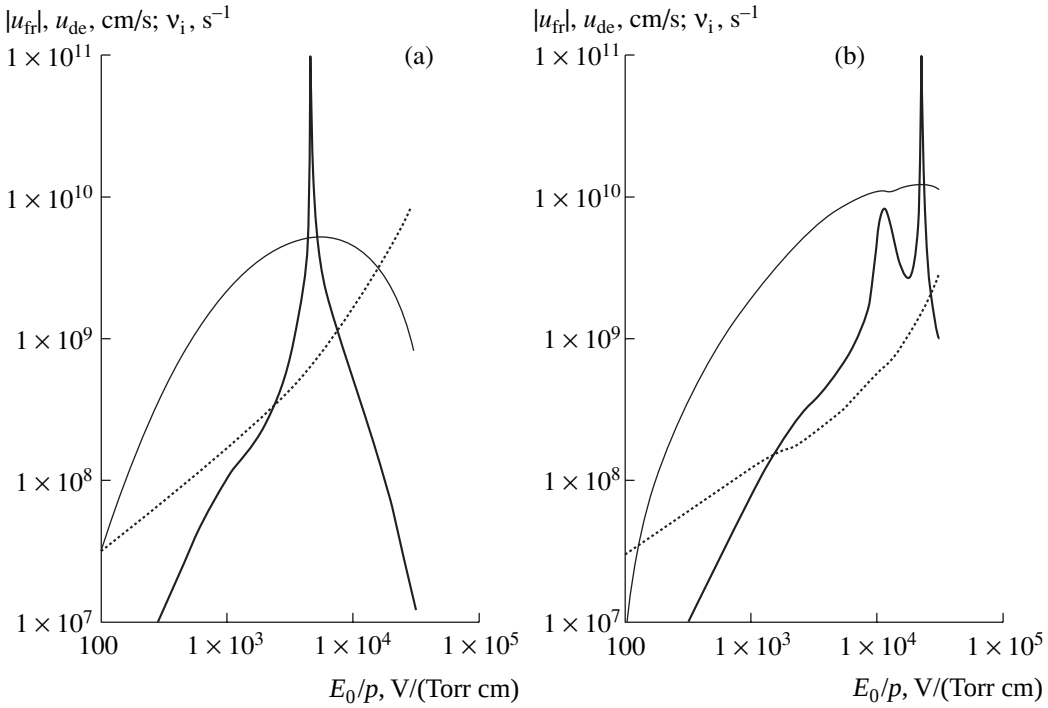

Fig. 2. Plots of the modulus of the ionization front velocity u_{fr} (thick solid curves), the electron drift velocity u_{de} (dash curves), and ionization rate (thin solid curves) versus the reduced field strength E_0/p at the streamer surface calculated by formulas (6)–(9) using $N_{cr} = 10^{14}$ cm^{-3}, $N_0 = 10$ cm^{-3}, $r_0 = 0.5$ mm, $p = 1$ bar and data from [20, 21] for (a) N_2 [$(E_0/p)_{cr} \approx 4.7$ kV/(Torr cm)] and (b) xenon [$(E_0/p)_{cr} \approx 23$ kV/(Torr cm)].

Of course, there is a large number of phenomena related to streamers that were not taken into account in the above considerations. In particular, the preionization of a gas with fast electrons emitted from the anode streamer end is possible. Nevertheless, the proposed model provides for a simple mechanism explaining the streamer propagation toward both anode and cathode.

REFERENCES

1. L. B. Loeb, *Fundamental Processes of Electrical Discharges in Gases* (Wiley, New York, 1939; Gostekhizdat, Moscow, 1950).
2. V. L. Granovskiĭ, *Electric Current in a Gas* (Gostekhizdat, Moscow, 1952), Vol. 1.
3. P. A. Kaptsov, *Electronics* (Gostekhizdat, Moscow, 1954).
4. J. M. Meek and J. D. Craggs, *Electrical Breakdown of Gases* (Clarendon Press, Oxford, 1953; Inostrannaya Literatura, Moscow, 1960).
5. H. Raether, *Electron Avalanches and Breakdown in Gases* (Butterworths, London, 1964; Mir, Moscow, 1968).
6. É. D. Lozanskiĭ and O. B. Firsov, *Theory of Spark* (Atomizdat, Moscow, 1975).
7. Yu. P. Raizer, *Physics of Gas Discharge* (Nauka, Moscow, 1992; Springer-Verlag, Berlin, 1991).
8. M. C. Wang and E. E. Kunhardt, Phys. Rev. A **42**, 2366 (1990).
9. P. A. Vitello, B. M. Penetrante, and J. N. Bardsley, Phys. Rev. E **49**, 5574 (1994).
10. A. A. Kulikovsky, Phys. Rev. E **57**, 7066 (1998).
11. A. Rocco, U. Ebert, and W. Hundsdorfer, Phys. Rev. E **66**, 035102(R) (2002).
12. M. Arrayás, U. Ebert, and W. Hundsdorfer, Phys. Rev. Lett. **88**, 174502-1 (2002).
13. A. A. Kulikovsky, Phys. Rev. Lett. **89**, 229401 (2002).
14. N. S. Rudenko and V. I. Smetanin, Izv. Vyssh. Uchebn. Zaved. Fiz., No. 7, 34 (1977).
15. L. P. Babich, Fiz. Plazmy **7**, 1419 (1981) [Sov. J. Plasma Phys. **7**, 783 (1981)].
16. A. N. Tkachev and S. I. Yakovlenko, Pis'ma Zh. Éksp. Teor. Fiz. **77**, 264 (2003) [JETP Lett. **77**, 221 (2003)].
17. A. N. Tkachev and S. I. Yakovlenko, Pis'ma Zh. Tekh. Fiz. **29** (16), 54 (2003) [Tech. Phys. Lett. **29**, 683 (2003)].
18. A. N. Tkachev and S. I. Yakovlenko, Laser Phys. **12**, 1022 (2002).
19. A. N. Tkachev and S. I. Yakovlenko, Laser Phys. **12**, 1221 (2002).
20. A. N. Tkachev and S. I. Yakovlenko, Pis'ma Zh. Tekh. Fiz. **29** (16), 45 (2003) [Tech. Phys. Lett. **29**, 679 (2003)].
21. A. N. Tkachev and S. I. Yakovlenko, Pis'ma Zh. Tekh. Fiz. **30** (7), 14 (2004) [Tech. Phys. Lett. **30**, 265 (2004)].

Translated by P. Pozdeev

Technical Physics Letters, Vol. 30, No. 5, 2004, pp. 358–360. Translated from Pis'ma v Zhurnal Tekhnicheskoĭ Fiziki, Vol. 30, No. 9, 2004, pp. 21–25.

The Formation of Pulsed Supersonic Underexpanded Jets Influenced by a Background Gas

N. G. Korobeĭshchikov*, A. E. Zarvin, and V. Zh. Madirbaev**

Novosibirsk State University, Novosibirsk, Russia

*e-mail: * korobei@ci.nsu.ru; ** zae@phys.nsu.ru*

Received September 22, 2003

Abstract—We have studied the gasdynamics of a pulsed jet expansion of He, Ar, and N_2 with moderate n ($\sim 10^3$–10^6) and Reynolds numbers in the interval $Re_L \sim 1$–10^2. The laws of motion of the leading front in pulsed jets of various gases are determined. It is found that the front velocities of such jets are significantly lower than the limiting values for a stationary expansion of the corresponding gases. The pulsed jet structure has been studied for various similarity parameters of the system. It is shown that the size of a quasi-stationary region in the gas moving away from the source decreases depending on n. © *2004 MAIK "Nauka/Interperiodica".*

The laws of gasdynamics of free nonstationary jets have been studied in sufficient detail either for large ($n \sim 10^8$), whereby the gas outflows into a space with very low background pressure ($P_b \sim 10^{-3}$ Pa) [1, 2], or for small ($n \sim 10^2$) corresponding to the expansion into a flooded space with high background pressure ($P_b \sim$ 10 Pa) [3, 4]. In the former case, the flow structure is adequately described by the model of free expansion into vacuum, whereby the leading front of the jet moves with the limiting velocity of a nonstationary flow and the boundary of the region of quasi-stationary flow moves with the limiting velocity of a nonstationary flow [5]. In the latter case, the leading front features the formation of a characteristic shock-wave structure comprising compressed layers of the outflowing gas and the background gas displaced from the flow region. The interval of intermediate n values, which is most interesting from the standpoint of the pulsed gas jet and molecular beam applications, remains almost uninvestigated.

We have studied the gasdynamics of a pulsed jet expansion of various gases (helium, nitrogen, argon) into a space with reduced background pressure. The expansion was in the form of long pulses with a duration of ~1 ms at the supersonic nozzle output and an off-duty ratio of no less than 100. The investigation was performed on the LEMPUS complex gasdynamic setup created at Novosibirsk State University. The pulsed gas jets were studied by methods of molecular beam mass spectrometry [6] and electron beam spectroscopy [7]. We have studied strongly underexpanded ($n \sim 10^3$–10^6) pulsed jets under the conditions of significant influence of the background gas ($P_b \sim 10^{-2}$–10^0 Pa; $Re_L \sim 1$–10^2). The jets were characterized by the leading front velocity of the outflowing gas and the duration of the region of quasi-stationary flow for various values of the control gasdynamic parameters, including the stagnation pressure P_0 (10^0–10^3 kPa), the nozzle diameter (0.5 and 1 mm), and the distance from the source x/d (10–225).

Under the given experimental conditions (in contrast to the case of expansion into vacuum), no primary rarefaction wave is formed, at least in the studied range of distances from the source. Therefore, the leading front position in the outflowing jet determines the front boundary of a quasi-stationary flow region. At the same time (in contrast to the continuous medium) the retarding action (drag) of the background gas on the outflowing gas does not lead to the formation of strong hydrodynamic pressure jumps (shock waves) on the leading front. The leading front velocities V_{imp} are significantly lower than the limiting velocities of a stationary (and the more so, nonstationary) flow of the corresponding gas: V_{imp} = 1230, 370, and 400 m/s for helium, argon, and nitrogen, respectively, at a background gas pressure of $P_b \sim 0.1$ Pa in the expansion chamber. For the convenient comparison of experimental data corresponding to various times of motion of the leading front under various expansion conditions, we used (as suggested in [5]) the dimensionless similarity parameters of time, $\tau = (\rho_b/\rho_a)^{1/2} t v_a/r_a$, and distance, $\xi = (\rho_b/\rho_a)^{1/2} r/r_a$, where a is the index characterizing the gas parameters at the source output.

Figure 1 presents the experimental results for the pulsed jets of He, Ar, and N_2 constructed in the above dimensionless variables. As can be seen, there is a generalized dependence for each gas describing the data obtained for various retarding and background gas pressures and even nozzle diameters. Solid curves drawn in Fig. 1 show the results of model calculations [5]. A comparison with the experimental data shows that the

1063-7850/04/3005-0358$26.00

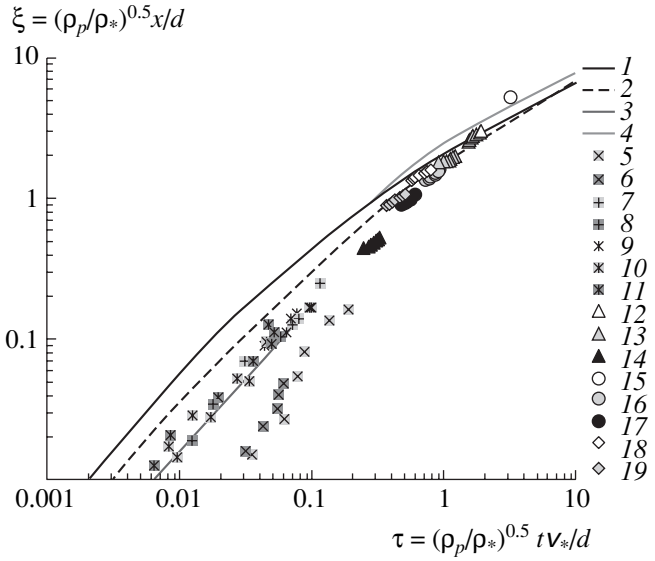

Fig. 1. The motion of the leading front of a pulsed gas jet described in terms of dimensionless similarity parameters: (*1*) N_2, theory [5]; (*2*) Ar, theory [5]; (*3*) experiment [1]; (*4*) experiment [3]; (*5*) He, free jet, P_0d = 100 kPa mm; (*6*) He, free jet, P_0d = 800 kPa mm; (*7*) Ar, free jet, P_0d = 11 kPa mm; (*8*) Ar, free jet, P_0d = 220 kPa mm; (*9*) N_2, free jet, P_0d = 100 kPa mm; (*10*) N_2, free jet, P_0d = 220 kPa mm; (*11*) N_2, free jet, P_0d = 440 kPa mm; (*12*) He, molecular beam, P_0d = 10 kPa mm; (*13*) He, molecular beam, P_0d = 55 kPa mm; (*14*) He, molecular beam, P_0d = 800 kPa mm; (*15*) Ar, molecular beam, P_0d = 6 kPa mm; (*16*) Ar, molecular beam, P_0d = 40 kPa mm; (*17*) Ar, molecular beam, P_0d = 55 kPa mm; (*18*) N_2, molecular beam, P_0d = 40 kPa mm; (*19*) N_2, molecular beam, P_0d = 100 kPa mm.

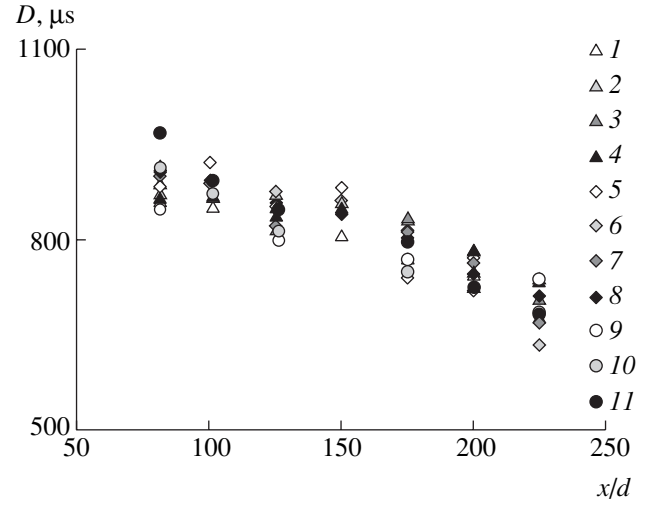

Fig. 2. The pulse halfwidth characterizing the length of the stationary flow region at various distances from the source: (*1*) He, P_0d = 28 kPa mm; (*2*) He, P_0d = 100 kPa mm; (*3*) He, P_0d = 225 kPa mm; (*4*) He, P_0d = 460 kPa mm; (*5*) N_2, P_0d = 5 kPa mm; (*6*) N_2, P_0d = 50 kPa mm; (*7*) N_2, P_0d = 70 kPa mm; (*8*) N_2, P_0d = 100 kPa mm; (*9*) Ar, P_0d = 5 kPa mm; (*10*) Ar, P_0d = 17 kPa mm; (*11*) Ar, P_0d = 28 kPa mm.

model gives overstated estimates of the leading front velocity, especially for small τ and ξ values. According to [5], this is explained by the assumption of a nonviscous gas used in the model. The dash–dot lines in Fig. 1 present the experimental data obtained under different nonstationary expansion conditions for argon outflowing into vacuum [1] and for a shock-wave-heated jet of nitrogen [3]. These data are in good agreement with our results.

According to the model [5] for the pulsed jet expansion into vacuum, the time of existence of a stationary flow in the gas moving downjet from the source decreases because some of the gas particles go to the leading and trailing rarefaction waves. For the same initial pulse duration, the time of existence of a stationary flow at a fixed distance from the source depends on the adiabatic exponent γ of the gas: the smaller the γ value, the greater the length of the stationary flow region. In our experiments with the expansion into a space with low background pressure P_b under otherwise equal conditions (a fixed distance from the nozzle, initial pulse duration, and the P_0 and P_b values), the length of the stationary flow region was the same for all gases (i.e., independent of the adiabatic exponent).

Figure 2 shows data on the halfwidths of gas pulses in helium, nitrogen, and argon measured at various distances from the source for the same initial pulse duration and different stagnation pressures. As can be seen, the pulse halfwidths (and, hence, the length of the stationary flow region) in the gas moving downjet from the source decreases: the higher the background pressure, the greater the rate of decrease. At a fixed distance from the source, the length of the stationary flow region increases with the pressure P_0.

Under the experimental conditions studied, the mass of a gas outflowing from the source is comparable with that of the background gas displaced from the flow region. The drag related to the background gas results in that the jet is retarded at the leading front and passes to the trailing rarefaction wave. Accordingly, the length of the stationary flow region decreases downjet the flow. An increase in the stagnation pressure or the nozzle diameter leads to a growth in the specific (per unit time) rate of the gas outflow from the nozzle. As a result, the outflowing gas more intensively displaces the background gas from the flow region. Thus, in contrast to the case of expansion into vacuum, the length of the stationary flow region depends not only on the initial pulse duration but also on the ration of retarding and background pressures P_0/P_b in the flow region.

Acknowledgments. This study was supported by the Federal Targeted Program "Integration of Science and High School in Russia: 2002–2006" (State Contract no. LO 126/805) and the Ministry of Industry, Sci-

ence, and Technology of the Russian Federation within the framework of the Program of Support for Unique Research and Experimental Setups (project no. 06-05).

REFERENCES

1. A. V. Eremin, V. A. Kochnev, A. A. Kulikovskiĭ, *et al.*, Zh. Prikl. Mekh. Tekh. Fiz., No. 1, 34 (1978).
2. V. A. Kochnev and I. M. Naboko, Zh. Prikl. Mekh. Tekh. Fiz., No. 1, 107 (1980).
3. I. M. Naboko, V. V. Golub, A. V. Eremin, *et al.*, Arch. Mech. **29**, 69 (1977).
4. B. M. Dobrynin, V. G. Maslennikov, and V. A. Sakharov, Zh. Tekh. Fiz. **57**, 118 (1987) [Sov. Phys. Tech. Phys. **32**, 69 (1987)].
5. S. F. Chekmarev, *Pulsed Gas Flows in Supersonic Nozzles and Jets* (Inst. Teplofiz. Sib. Otd. Akad. Nauk, Novosibirsk, 1990).
6. A. E. Zarvin, N. G. Korobeĭshchikov, V. Zh. Madirbaev, *et al.*, Prib. Tekh. Éksp., No. 5, 64 (2000).
7. G. G. Gartvich, A. E. Zarvin, V. V. Kalyada, *et al.*, Zh. Prikl. Mekh. Tekh. Fiz. **34** (5), 150 (1993).

Translated by P. Pozdeev

Technical Physics Letters, Vol. 30, No. 5, 2004, pp. 361–363. Translated from Pis'ma v Zhurnal Tekhnicheskoĭ Fiziki, Vol. 30, No. 9, 2004, pp. 26–32.

Interfacial Capacitance in Epitaxial Heterostructures $La_{0.67}Ca_{0.33}MnO_3/SrTiO_3/La_{0.67}Ca_{0.33}MnO$

Yu. A. Boikov* and V. A. Danilov

Ioffe Physicotechnical Institute, Russian Academy of Sciences, St. Petersburg, 194021 Russia

** e-mail: yu.boikov@mail.ioffe.ru*

Received October 13, 2003

Abstract—Epitaxial trilayer heterostructures of the type $La_{0.67}Ca_{0.33}MnO_3/SrTiO_3/La_{0.67}Ca_{0.33}MnO_3$ were grown by laser ablation on $(001)[(LaAlO_3)_{0.3} + (Sr_2AlTaO_6)_{0.7}]$ substrates. The real part of the dielectric permittivity ε and the loss factor $\tan\delta$ of a 1100-nm-thick $SrTiO_3$ interlayer were studied in the temperature interval T = 4.2–300 K in a nonbiased state and at a bias voltage of ±2.5 V applied to the manganite electrodes. Using the temperature dependence $\varepsilon(T)$ measured for the $SrTiO_3$ layer grown between the manganite electrodes, we have estimated the capacitance of $La_{0.67}Ca_{0.33}MnO_3/SrTiO_3$ interfaces ($C_1 \approx 2$ μF/cm^2) related to the electric field penetrating from the interlayer into $La_{0.67}Ca_{0.33}MnO_3$. *© 2004 MAIK "Nauka/Interperiodica".*

Perovskite-like ferroelectrics of the $(Ba,Sr)TiO_3$ system are promising materials for tunable devices in microwave electronics [1]. In real devices, a ferroelectric layer possessing a nonlinear dependence of the polarization on the applied electric field strength must be a component of a thin-film heterostructure including conducting (metal or superconductor) electrodes. The dielectric response of the ferroelectric film to variations in the ambient temperature and the applied electric field strongly depends on the structure and properties of ferroelectric–electrode interfaces. The response of the real part of the dielectric permittivity ε of a $(Ba,Sr)TiO_3$ film to the electric field is usually much lower compared to the response of analogous bulk crystals.

Using thin epitaxial films of conducting oxides such as $SrRuO_3$ (SRO) and $YBa_2Cu_3O_{7-\delta}$ (YBCO) [2] as electrodes, it is possible to obtain multilayer heterostructures with ferroelectric layers possessing clear preferential orientation (azimuthal and relative to the normal to the substrate plane) and the real part of dielectric permittivity ε obeying the Curie–Weiss law.

This Letter presents the results of experimental investigation of the temperature and field dependence of ε for an $SrTiO_3$ (STO) layer grown between two $La_{0.67}Ca_{0.33}MnO_3$ manganite (LCMO) film electrodes.

Epitaxial trilayer (120 nm)LCMO/(1100 nm)STO/(120 nm)LCMO heterostructures were grown by laser ablation (KrF, λ = 248 nm, τ = 30 ns) on polished $(001)[(LaAlO_3)_{0.3} + (Sr_2AlTaO_6)_{0.7}]$ (LSATO) substrates. Technological parameters of the deposition of manganite and ferroelectric films are given elsewhere [2, 3]. Square contact pads ($S = 200 \times 200$ μm) in the upper manganite layer of the LCMO/STO/LCMO heterostructure were formed using photolithography and ion beam etching (Ar, 500 V, 0.2 mA).

The capacitance C of the plane-parallel film capacitor structures was measured using an HP Model 4263A LCR meter (f = 100 kHz) with and without a bias voltage ($V_b = \pm 2.5$ V) applied to the electrodes. The permittivity ε of the STO layer was calculated as $C = \varepsilon S/d$. The resistance R of the manganite electrodes was measured by the same LCR meter in the Van der Pauw geometry and then the resistivity ρ was calculated as $\rho = R\pi d_1/\ln 2$ [4], where d_1 is the electrode thickness.

The results of the X-ray diffraction investigation indicated that the STO interlayer (as well as the manganite electrodes) in the plane-parallel trilayer LCMO/STO/LCMO heterostructure possesses clearly defined orientation both in the substrate plane and in the azimuthal direction. The $\omega/2\theta$ and ϕ scans showed that the (001) plane and the [010] direction in the LCMO and STO layers are parallel to the analogous plane and direction in the substrate. Figure 1 shows the X-ray diffractogram obtained with both incident and reflected beams lying in the plane normal to the substrate. The crystal lattice parameter in the STO layer of the LCMO/STO/LCMO heterostructure measured along the normal to the substrate plane was $a_\perp = 3.908 \pm 0.003$ Å, almost coinciding with the value measured in the plane, $a_\parallel = 3.906 \pm 0.003$ Å. The effective unit cell volume, $V_{\text{eff}} = a_\perp x a_\parallel^2 = 59.62$ Å^3, in the STO layer was approximately equal to that in stoichiometric single crystals of strontium titanate (≈59.55 Å^3 [5]). The half-width (full width at half maximum) of the X-ray rocking curve for the (002)STO reflection in the LCMO/STO/LCMO heterostructure was 0.17°. This value is in good agreement with the analogous data for the epitaxial layers of strontium titanate grown on the surface of YBCO electrodes, while being about three

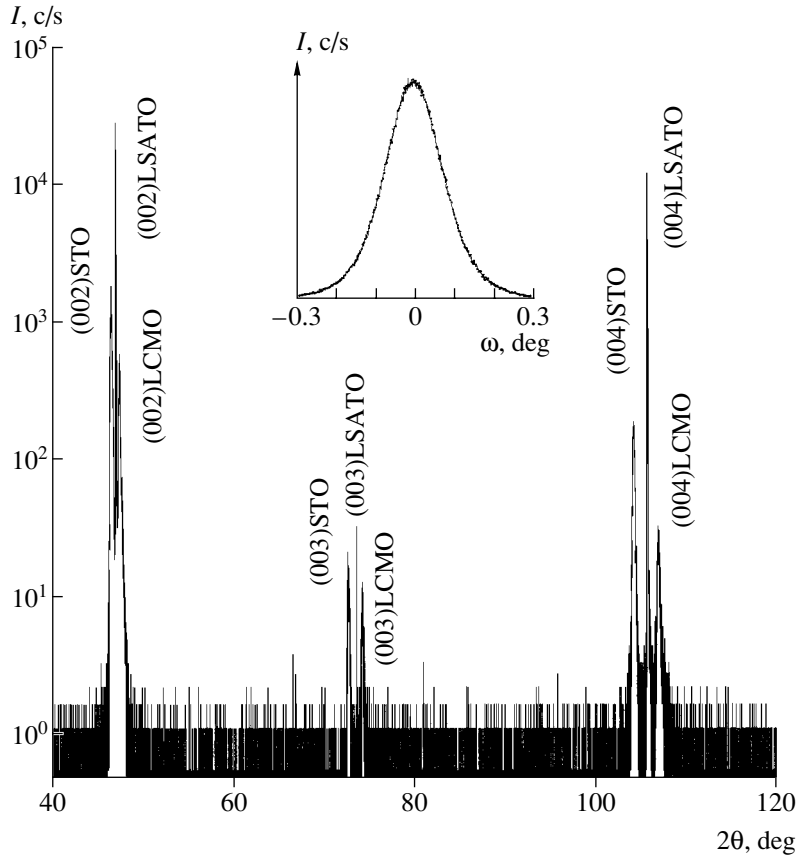

Fig. 1. The X-ray diffractogram (Cu$K_{\alpha 1}$, ω/2θ scan) of an (001)LCMO/(001)STO/(001)LCMO heterostructure on an (001)LSATO substrate, measured with both incident and reflected beams lying in the plane normal to the substrate. The inset shows the X-ray rocking curve for the (002)STO reflection of the same heterostructure.

times the halfwidth of the X-ray rocking curve for the (002)STO reflection from an epitaxial structure of the SRO/STO/SRO type [2].

Because of the differences in the crystal lattice parameters of LCMO, STO, and LSATO, both the lower and upper LCMO electrodes in the LCMO/STO/LCMO/(001)LSATO heterostructure were subjected to tensile stresses in the substrate plane. The crystal lattice parameter (~0.3868 nm) measured in the substrate plane in the lower electrode was greater than the corresponding parameter(~0.3837 nm) measured along the normal to the substrate surface.

Figure 2b shows the temperature dependence of the resistivity determined for an LCMO layer grown on (001)LSATO. Similar to the case of bulk stoichiometric samples, a sharp buildup in ρ(T) of the LCMO/(001)LSATO system is observed at 255–260 K. The resistivity of an LCMO film remains unchanged after the formation of a (1100 nm)STO layer.

Figure 2a shows the temperature dependence of ε measured at V_b = 0 for the STO layer in the LCMO/STO/LCMO heterostructure. In the temperature interval T = 80–200 K, the permittivity of the STO layer obeyed the relation

$$\varepsilon^{-1} = \varepsilon_0^{-1} C_0^{-1} (T - T_{\text{Weiss}}) + \varepsilon_1^{-1}, \quad (1)$$

where T_{Weiss} = 30 K is the Curie–Weiss temperature for single-domain strontium titanate single crystals [6], the quantity $C_0 \approx 0.77 \times 10^5$ K approximately coincides with the Curie constant for bulk STO samples [7], $\varepsilon_1 = 1530\varepsilon_0$ is a constant, and ε_0 is the permittivity of vacuum.

The first term on the right-hand side of relation (1) reflects the contribution to the measured permittivity from the volume of the ferroelectric layer, while the second term reflects the contribution from the LCMO/STO interfaces. The appearance of the latter term is related to the capacitance $C_1/2$ of interfaces [8] in the LCMO/STO/LCMO heterostructure. This capacitance is due to the electric field penetrating from the interlayer into the manganite electrodes. The capacitance per unit area of the LCMO/STO interface is $C_1 = 2\varepsilon_1/d \approx 2 \times 10^{-6}$ F/cm^2. This value is only slightly different from the capacitance of an interface between the dielectric and a noble metal [8]. The capacitance C_1 of the ferroelectric–electrode interface depends on the

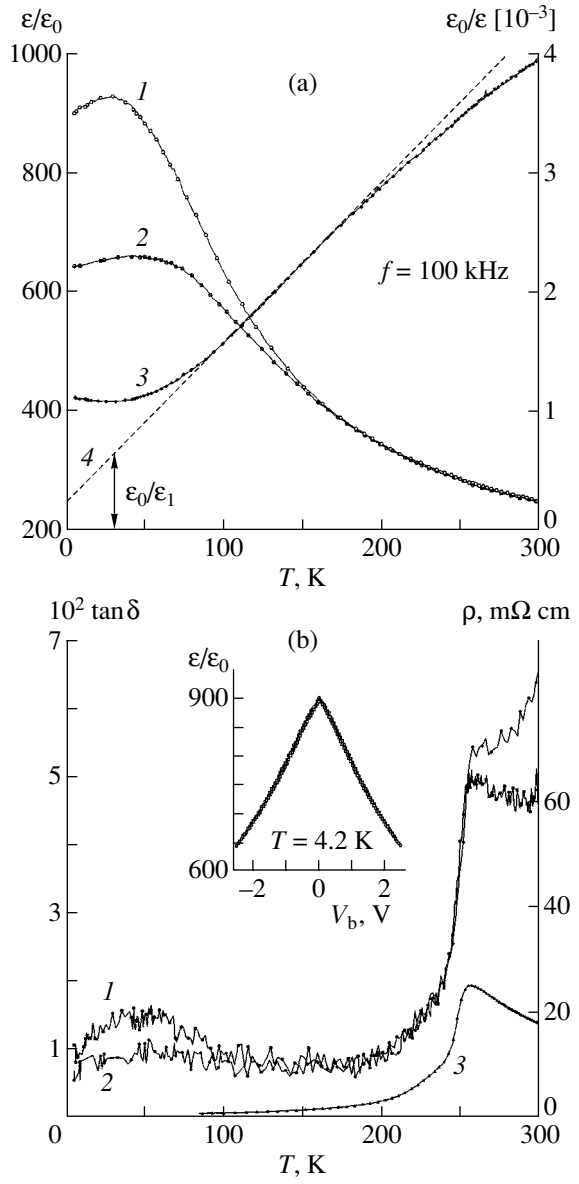

Fig. 2. (a) The temperature dependences of the permittivity ratios (*1*, *2*) $\varepsilon/\varepsilon_0$ and (*3*) $\varepsilon_0/\varepsilon$ for the STO layer in the LCMO/STO/LCMO heterostructure measured for $V_b = 0$ (*1*) and 2.5 V (*2*); line *4* is the tangent to the $\varepsilon/\varepsilon_0(T)$ curve in the interval $T = 80$–200 K (arrow indicates the $\varepsilon_0/\varepsilon_1$ value); (b) the temperature dependences of (*1*, *2*) the loss factor $\tan\delta$ of the STO interlayer and (*3*) the resistivity ρ of the lower LCMO layer in the LCMO/STO/LCMO heterostructure measured for $V_b = 0$ (*1*) and 2.5 V (*2*); the inset shows the $\varepsilon/\varepsilon_0(V_b)$ curve for the STO layer at $T = 4.2$ K.

depth L_e of the electric field penetration into the electrode and on the effective permittivity ε_e of the latter: $C_1 = \varepsilon_e/2.31L_e$ [8]. The field penetration depth L_e depends on the charge carrier density in the electrode and on the permittivity ε_e. For $T < 200$ K, the charge carrier density (holes, $p \approx 6 \times 10^{21}$ cm^{-3}) in LCMO is about ten times smaller than the analogous values for noble metals (Au, Pt). This circumstance favors an increase in L_e of manganite electrodes as compared to the analogous values for the noble metal electrodes. However, the permittivity of LCMO [9] is significantly higher than that of noble metals.

The effect of an applied electric field ($E = 25$ kV/cm) on the permittivity of the STO interlayer was clearly manifested at temperatures below 150 K. The most pronounced suppression of ε by the field was observed at temperatures (~25–30 K) in the vicinity of the maximum of $\varepsilon(T)$ (Fig. 2a). The curve of $\varepsilon(V_b)$ measured for the STO layer is virtually symmetric relative to $V_b = 0$ (see the inset on Fig. 2b), which is indicative of insignificant differences between the microstructure and electron parameters of the lower and upper ferroelectric–electrode interfaces in the LCMO/STO/LCMO heterostructure studied. The behavior of $\varepsilon(V_b)$ exhibits no any evidence of hysteresis.

Figure 2b also shows the temperature dependence of the loss factor $\tan\delta$ for the plane-parallel trilayer LCMO/STO/LCMO capacitor structure for $V_b = 0$ and 2.5 V ($f = 100$ kHz). At $T < 100$ K, the application of a bias voltage to the manganite electrodes led to a decrease (by ~50% at $T \sim 50$ K) in $\tan\delta$ for the LCMO/STO/LCMO heterostructure. The field-induced decrease in $\tan\delta$ can be at least partly related to a change in the domain structure of the STO layer. In the temperature interval $T = 100$–250, the electric field virtually did not affect the dielectric losses in the STO interlayer. Above 250 K, application of the electric field led to a growth in $\tan\delta$, probably because of an increase in the effective conductivity of the ferroelectric layer (the Poole–Frenkel effect [10]).

Acknowledgments. This study was supported by the Presidium of the Russian Academy of Sciences (project no. 9B19).

REFERENCES

1. J. P. Hong and J. S. Lee, Appl. Phys. Lett. **68**, 3034 (1996).
2. Yu. A. Boikov and T. Claeson, Physica C **336**, 300 (2000).
3. Yu. A. Boikov and T. Claeson, Physica B **311**, 250 (2002).
4. T. I. Kamins, J. Appl. Phys. **42**, 4357 (1971).
5. R. W. G. Wyckoff, *Crystal Structure*, 2nd ed. (Interscience, New York, 1964), Vol. 2, p. 394.
6. R. C. Neville, B. Hoeneisen, and C. A. Mead, J. Appl. Phys. **43**, 2124 (1972).
7. A. D. Hilton and B. W. Ricketts, J. Phys. D: Appl. Phys. **29**, 1321 (1996).
8. H. Y. Ku and F. G. Ullman, J. Appl. Phys. **35**, 265 (1964).
9. A. V. Boris, N. N. Kovaleva, A. V. Bazhenov, *et al.*, J. Appl. Phys. **81**, 5756 (1997).
10. J. R. Yeargan and H. L. Taylor, J. Appl. Phys. **39**, 5600 (1968).

Translated by P. Pozdeev

Technical Physics Letters, Vol. 30, No. 5, 2004, pp. 364–366. Translated from Pis'ma v Zhurnal Tekhnicheskoĭ Fiziki, Vol. 30, No. 9, 2004, pp. 33–37.

Study of the Reflectance of an Aluminum Film under Simultaneous Action of Current Pulses and Laser Radiation

V. V. Osipov*, A. N. Orlov, and V. V. Lisenkov**

Institute of Electrophysics, Ural Division, Russian Academy of Sciences, Yekaterinburg, Russia

*e-mail: * osipov@iep.uran.ru; ** lisenkov@iep.uran.ru*

Received July 29, 2003

Abstract—We have experimentally observed a reversible increase in the reflectance of aluminum at a wavelength of 308 nm during the passage of an electric current pulse with a density of up to 100 MA/cm^2. It is suggested that the effect is explained by partial reflection of the incident radiation by free electrons injected into the conduction band of an oxide film on the metal surface during the passage of a current pulse. *© 2004 MAIK "Nauka/Interperiodica".*

Wide use of lasers in basic research, medicine, and various commercial fields is related to a considerable extent with the possibility of controlling the laser pulse duration. This is achieved in most cases by modulating the *Q* value of the laser cavity with the aid of various converters, such as the Kerr cell, Pockels cell, etc. However, since optical materials used in such converters are transparent only within a certain wavelength interval, each modulator is applicable only in a rather narrow region of the spectrum of electromagnetic waves. While the number of materials for converters operating in the middle IR, far IR, and visible spectral range is sufficiently large, the class of materials for the UV range is rather restricted. In the vacuum UV range, it is difficult to find transparent materials with the properties required for their use in *Q*-switches.

We believe that a good alternative is offered by *Q*-switching through controlled variation of the reflectance of one of the cavity mirrors. The results of our previous experiments [1] showed that nanosecond current pulses can produce irreversible changes in the optical properties of aluminum films. In one experiment, the reflectance of an aluminum film exhibited a 13% increase after the first nine to ten current pulses, while subsequent pulses did not bring about additional changes.

In order to create a *Q*-switched laser cavity using this effect, it was necessary to study variations in the reflectance of an aluminum film during the passage of a current pulse.

The experiments were performed using a setup schematically depicted in Fig. 1. Pulsed radiation (λ = 308 nm) of a XeCl laser *1* was passed through beam-splitting plates *2* and *3*, reflected from a 200- to 1000-Å-thick metal film *4*, and measured by power meter *5* of the IMO-2N type. The measurements were performed during the passage of high current pulses through the metal film and in the absence of such pulses. The average laser pulse duration (full width at half maximum) was 30 ns, and the laser pulse energy was 20–40 mJ. Since the laser pulse energy could vary within 10–15%, a reference signal was formed by measuring the energy reflected from plate *3* with a 30% reflectance and measured by another IMO-2N power meter *5*.

The pulses of current with an amplitude of up to 1000 A and a width of 30–120 ns were passed through thin aluminum film by discharge of a capacitor bank *C* via a limiting resistor *R*. A two-beam oscillograph *8* (S8-14) measured the shape of current pulses (in shunt *6*) and the shape of laser pulses (via beam-splitting plate *2* and photodetector *7* of the FEK-22 SPU-M type).

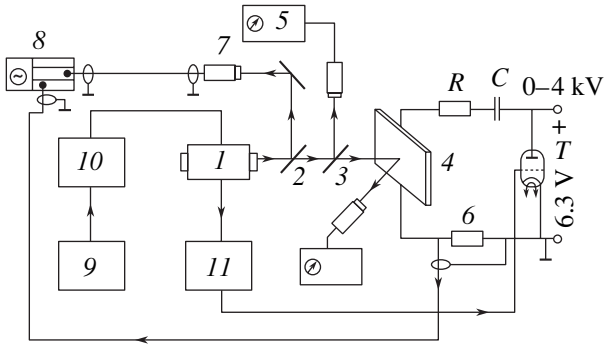

Fig. 1. Schematic diagram of the experimental setup (see the text for explanations).

1063-7850/04/3005-0364$26.00 © 2004 MAIK "Nauka/Interperiodica"

Thyratron *T* of the TGI1-500/16 type switched the charge accumulated by the capacitor bank *C* to the sample film on receiving a positive pulse from the XeCl laser power supply unit *10* driven by a high-voltage pulse generator *9*. Using delay line *11*, it was possible to control the thyratron switch time with a 10-ns step.

Changes in the sample reflectance were determined by simultaneously monitoring the two beams of laser radiation (reference and reflected) with the aid of two power meters IMO-2N. It was found that the pulses of current with a density below 100 MA/cm^2 lead to a reversible increase in the reflectance of the metal film. The results of measurements are presented in the table.

We believe that the observed effect is related to the reflection of laser radiation from an oxide film always formed on the surface of aluminum in atmosphere. The mechanism of light reflection from such an oxide film was described in [2] for V_2O_5. According to this, the laser radiation can be partly reflected by free electrons injected by various means into the conduction band of the oxide film. The reflection from the film will predominate under the condition that the laser radiation frequency ω_{las} is close to the frequency of plasma oscillations ω_p of free electrons ($\omega_{las} \sim \omega_p$).

We have calculated the total reflectance of the metal–oxide film system assuming that the reflectance R_m of the metal surface remains constant. The reflectance of the oxide film was calculated as

$$R_f = \frac{(n-1)^2 + k^2}{(n+1)^2 + k^2}, \quad (1)$$

where n and k are the indices of refraction and absorption of the metal oxide. These parameters are determined by solving the standard system of equations.

$$n^2 - k^2 = n_0 - \frac{\omega_p^2 \tau^2}{1 + \omega_{las}^2 \tau^2}, \quad (2)$$

$$nk = \frac{\omega_p^2 \tau}{2\omega_{las}(1 + \omega_p^2 \tau^2)}, \quad (3)$$

where $n_0 = 1.57$ is the refractive index of Al_2O_3 under normal conditions (i.e., for almost complete absence of free electrons in the conduction band) and τ is the average time of electron relaxation. The latter parameter was assumed to be equal to that in pure aluminum and calculated using the data from [2].

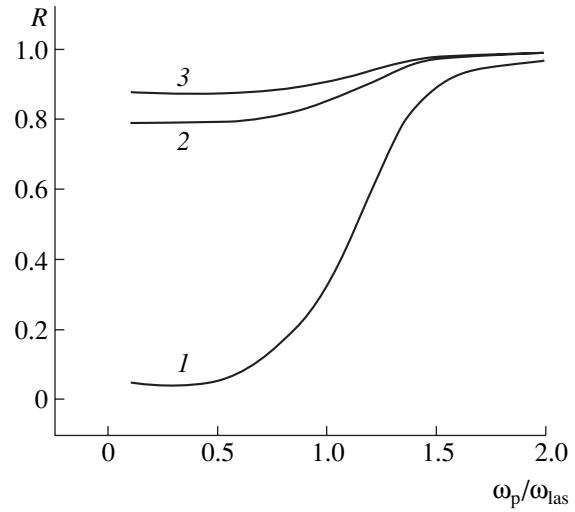

Fig. 2. Plots of the reflectance of (*1*) an oxide film and (*2*, *3*) a metal-oxide film system versus the ω_p/ω_{las} ratio calculated for different reflectances of the metal, R_m = 79 (*2*) and 88% (*3*).

The results of calculations presented in Fig. 2 show that the reflectance R of the metal–oxide film system increases with the density of free electrons (proportional to the ω_p/ω_{las} ratio). The growth in R becomes more pronounced (curves *2* and *3*) with a decrease in the reflectance of the metal, which can be induced by laser radiation heating of the metal. Therefore, the effect should be more clearly manifested with increasing laser pulse energy, in agreement with what was observed in experiment.

We cannot unambiguously indicate the factor responsible for the appearance of free electrons in the conduction band of the oxide film. One possible scenario is as follows. The heating of aluminum by a current pulse can change the stoichiometry and phase composition of the oxide film, leading to the formation of phases with small bandgap widths. A decrease in this value favors the injection of electrons immediately from the metal into the conduction band of oxide: as is known, the Fermi level of the metal occurs in the middle of the bandgap of a dielectric film covering its surface. In addition, rapid expansion of the metal heated by sharp current pulses may lead to deformation of the

Variation of the reflectance of aluminum under the action of current pulses

Laser pulse energy, mJ	28	29	31.4	33.8
Reflectance (%) during the passage of electric current pulses	89	87.6	85	83
Reflectance (%) in the absence of electric current	88	86	82	79

oxide film at a rate comparable with that induced by a shock wave. The latter is known (see [3] and references cited therein) to produce a shift of the energy bands in dielectrics. A decrease in the bandgap width increases the probability of a short-time overlap of the valence and conduction bands, resulting in the electron injection.

Thus, our experiments revealed the effect of reversible increase in the reflectance of aluminum caused by the passage of high-density current pulses. A qualitative explanation of this phenomenon has been proposed. This effect can be used in *Q*-switched laser cavities and other optical systems related to the modulation of laser radiation.

REFERENCES

1. A. N. Orlov, V. V. Tsarapkin, and A. N. Gvozdikov, Fiz. Khim. Obrab. Mater., No. 3, 26 (1998).
2. A. M. Prokhorov, V. I. Konov, I. Ursu, and I. N. Mikheilesku, *Interaction of Laser Emission with Metals* (Nauka, Moscow, 1988).
3. Yu. N. Vershinin, *Electrothermal and Detonation Processes under the Electric Breakdown of Solid Insulators* (Ural. Otd. Ross. Akad. Nauk, Yekaterinburg, 2000).

Translated by P. Pozdeev

Technical Physics Letters, Vol. 30, No. 5, 2004, pp. 367–369. Translated from Pis'ma v Zhurnal Tekhnicheskoĭ Fiziki, Vol. 30, No. 9, 2004, pp. 38–43.

Doping Nanoparticles

V. M. Koshkin[a,*] and V. V. Slezov[b]

[a] *Kharkov Polytechnical Institute (National Technical University), Kharkov, Ukraine*
[b] *Kharkov Institute of Physics and Technology, National Scientific Center, Kharkov, Ukraine*
** e-mail: koshkin@kpi.kharkov.ua; vkosh@online.kharkov.ua*

Received November 20, 2003

Abstract—It is shown that the equilibrium solubility of impurities in disperse particles with dimensions on the order of several dozen ångströms can exceed the equilibrium solubility in the same massive material by up to two orders of magnitude. Simultaneous allowance of the variation of both surface and volume energy upon the dissolution of impurities leads to stabilization of the disperse system. Experiments confirming this effect are discussed and the possible practical inferences are considered. © *2004 MAIK "Nauka/Interperiodica".*

There is experimental evidence that the mutual solubility of components of two-phase metal alloys with a grain size on the order of a few dozen ångströms in the solid state is several orders of magnitude greater than in analogous massive alloys. This phenomenon has been observed in systems where the equilibrium solubility in massive samples is extremely small [1, 2]. We believe that elucidation of the nature of this effect will open new possibilities in the physics and technology of nanoparticles.

Consider a system comprising melt A of a very large volume containing a single solid particle B with the volume V and the surface area S. Peculiarities of the dissolution of small particles were studied more than a century ago by Ostwald, who showed that the solute concentration C over the lone particle B occurring in a finite volume of medium A exponentially increases with the ratio S/V, that is, with a decrease in the particle size. The effect becomes significant for the particles with a characteristic size L on the order of a few dozen ångströms. This behavior is similar to the analogous Laplace–Thomson effect, whereby the vapor pressure over drops increases when the drop size decreases. Such effects are sometimes considered as being due to an increase in surface curvature, although the curvature is nothing but a convenient macroscopic parameter reflecting the S/V ratio and not related to the physics of phenomena. The phenomenon under consideration is determined only by the tendency of the system to minimize the free energy—in particular, to reduce the area of contact between phases—and takes place for small cubes and thin films as well as for small balls (see [3]).

A system of such particles in a bounded volume is substantially unstable with respect to the particle size distribution and evolves toward their coarsening. The limit corresponds to the equilibrium, whereby a massive single crystal occurs in a saturated solution or melt. If the solvent volume is very large, the equilibrium is achieved upon complete dissolution of small particles. The general theory of evolution for disperse systems has been constructed in [4]. This theory is universal for particles of any nature, provided that the surface tension at the boundaries of disperse particles remains unchanged in the course of evolution.

However, thermodynamics also "offers" another means of minimizing the free energy of a two-phase system. According to this, a decrease in the free energy can be achieved through a decrease in the area of the interphase boundary and via the formation of a solid solution of substance A in substance B, provided that this would reduce the specific surface energy σ. The same is valid for a system of two fluids (two liquids or a liquid and a gas). Of course, thermodynamics makes use of both ways to provide for a decrease in the total free energy. Kukushkin and Osipov [5, 6] studied the variation of solubility in solid particles depending on their dimensions. Below, we propose a somewhat more general approach and the results will be compared to the conclusions obtained in [5, 6]. Anyhow, the second thermodynamic scenario of the transition of disperse systems to equilibrium is still incompletely studied. In systems with small particles, this aspect of evolution to the equilibrium opens new possibilities for creating materials which cannot be obtained by other means. Let us study this thermodynamic possibility.

The Helmholtz free energy F of the aforementioned system is determined, provided that the volume of medium A is sufficiently large, by the free energy F_B of the solid particle and its surface energy $\sigma(C)$. The formation of a solid solution with a small concentration C of substance A in substance B is characterized by the additional internal energy U accompanying the localization of a single atom of A in the crystal B. The change in F with allowance of both components can be expressed as

$$\Delta F = (UCN + NkTC\ln C)V + \sigma(C)S, \qquad (1)$$

where N is the number of atoms per unit volume of B, k is the Boltzmann constant, and T is the absolute temperature. Since the surface entropy weakly depends on the concentration [3], the corresponding term in (1) is omitted.

To the first approximation, it is expedient to assume that σ is a linear function of the concentration of A in B:

$$\sigma(C) = \sigma_{AB} + \beta C, \quad (2)$$

where β is a numerical coefficient determined below.

Minimization of the F value yields the following equilibrium concentration C_d of A in particle B:

$$C_d = C_0 \exp\left(-\frac{\beta}{NkT}\frac{S}{V}\right) = C_0 \exp\left(-\frac{\beta V_m}{RT}\frac{S}{V}\right), \quad (3)$$

where C_0 is the equilibrium concentration of A in a massive crystal B, V_m is the molar volume of B, and R is the universal gas constant. For a large particle, $S/V \ll 1$ and, hence, $C_d = C_0$. Here, it should be noted that expansion of expression (3) into series for small values of the coefficient determining the dependence of surface energy (2) on the concentration of impurity A in B leads to a relation coinciding with the formulas obtained in [5].

The observed effect is determined by the ratio S/V, which increases as $1/L$ when the particle size L decreases, and by the coefficient β. It is the latter quantity that determines the real physical meaning of the phenomena under consideration; this value can be readily evaluated. Indeed, for $C = 1$, σ is the specific energy of the boundary between pure crystal A and its melt, so that $\beta = \sigma_{0B} - \sigma_{AB}$, where σ_{AB} is the surface energy of the boundary between pure crystal B and pure melt A.

As can be seen from relation (3), for $\beta < 0$, the equilibrium content of A in crystalline particle B increases with decreasing particle size; for $\beta > 0$, the equilibrium concentration of A in B decreases. Thus, the sign of β determines the sign of the observed effect. Let us study this circumstance in more detail and consider the consequences of importance for applications.

If the energy of B–B bonds is greater than that of A–A bonds, a minimum surface energy is inherent in the boundary of a crystal with its own melt. In this case, $\beta < 0$ and, according to relation (3), the solubility of A in the solid particle B will increase with decreasing particle size. Note that this ratio of the binding energies corresponds to a small solubility of A in massive B, that is, to large U values. Thus, the result is at first glance paradoxical: the lower the solubility in a massive solid phase, the higher the solubility in small solid particles—this is exactly what was observed in [1, 2]. According to relation (3), the ratio of equilibrium solubilities of A in disperse and massive B is independent of U. The latter value depends, generally speaking, not only on the difference of binding energies but also on the crystal lattice distortions near an impurity atom; however, if the difference between the energies of chemical bonds is more or less pronounced, it is this factor that contributes most significantly to the U value and the above conclusion concerning the opposite correlation between solubilities in the massive and disperse phases is quite general.

And there is no place for paradoxes: thermodynamics selects a microscopic mechanism that provides for the minimum total free energy. If it is energetically more favorable to form a solid solution with decreased surface energy at the expense of an apparently "unfavorable" (for the massive) dissolution in the solid phase, this scenario will be realized. A decrease in the surface energy competes with an increase in the internal energy of the solid particle. Judging by the form of the expression for C_d obtained from relation (3),

$$C_d = \exp\left[-\frac{U}{kT} - \frac{\beta}{NkT}\frac{S}{V} - 1\right], \quad (4)$$

this process appears as an effective decrease in U in the small particle for $\beta < 0$. This effect allows disperse particles to be doped when introduction of the same impurities into massive sample is practically impossible. The same effect accounts for the higher content of equilibrium vacancies in highly disperse solids in comparison to massive samples, which is pointed out by many researchers.

In the case of $\beta > 0$ (e.g., when the energy of A–B bonds is greater than that of B–B bonds), the formation of an interface is energetically more favorable than the dissolution of A in solid B. Indeed, the surface provides for a net gain due to the A–B bonds, while in the bulk this gain is reduced by unavoidable lattice distortions. This case corresponds to systems of ordered phases (solid state compounds), for which the solubility in disperse particles is lower than in massive samples. This circumstance can also be used in practice, for example, for eliminating the deviations from stoichiometry in semiconductor compounds.

There are numerous technical applications in which dispersion does not pose limitations. Intriguing hypothetical systems are colloidal lasers or scintillators comprising small particles distributed in an "appropriate" matrix. In particular, one possibility is offered by intercalated layered semiconductors [7]. In the course of intercalation, these systems exhibit dispersion into particles with dimensions on the order of a few dozen ångströms [8]. The above phenomena must also be significant in nanoelectronics, where heterophase regions in the working elements have dimensions on the same order of magnitude.

It is important to note that, in contrast to the Ostwald–Thomson equilibrium corresponding (as was demonstrated above) to complete dissolution, provided that the solvent volume is sufficiently large, the proposed mechanism retains the system of disperse particles in equilibrium with the pure solvent. This creates

new possibilities for the stabilization (or breakage) of disperse systems, which can also be of interest from a technological standpoint.

The aim of this Letter was only to outline the phenomenon. Of course, equilibria will be studied taking into account both mechanisms operating simultaneously, the kinetics of equilibrium setting, the evolution of the particle size distribution (generalizing the previous results [4]), and other aspects. It is likely that the radiation stability of particles with dimensions comparable with the zones of instability of the point defects can be significantly higher than that of massive crystals (see [9]).

Let us estimate the scale of the phenomena considered above. For $T = 1000$ K, the value $\sigma = 1$ J/m^2, typical of metals (see [3]), and a particle size of 2×10^{-9} m, the ratio of solubilities is estimated as $C_d/C_0 = 200$. Thus, the effect is worthy of attention.

Acknowledgments. This study was supported in part by the Ukrainian Scientific-Technological Center (grant no. 36) and the Basic Research Foundation of Ukraine.

REFERENCES

1. A. I. Zubkov, A. I. Il'inskiĭ, O. A. Podgornaya, *et al.*, Fiz. Met. Metalloved., No. 10, 197 (1990).
2. H. Gleiter, J. Weissmuller, O. Wollersheim, *et al.*, Acta Mater. **49**, 737 (2001).
3. Yu. G. Frolov, *Course of Colloid Chemistry: Surface Phenomena and Disperse Systems* (Khimiya, Moscow, 1982).
4. I. M. Lifshits and V. V. Slezov, Zh. Éksp. Teor. Fiz. **35**, 479 (1958) [Sov. Phys. JETP **8**, 331 (1959)].
5. S. A. Kukushkin and A. V. Osipov, Zh. Tekh. Fiz. **67** (10), 112 (1997) [Tech. Phys. **42**, 1212 (1997)].
6. S. A. Kukushkin and A. V. Osipov, Usp. Fiz. Nauk **168**, 1083 (1998) [Phys. Usp. **41**, 983 (1998)].
7. V. M. Koshkin and Yu. N. Dmitriev, *Chemistry and Physics of Compounds with Loose Crystal Structure* (Academic, Dordrecht, 1994).
8. V. M. Koshkin and A. P. Mil'ner, Pis'ma Zh. Tekh. Fiz. **9**, 1431 (1983) [Sov. Tech. Phys. Lett. **9**, 615 (1983)].
9. V. M. Koshkin, Fiz. Nizk. Temp. **28**, 963 (2002) [Low Temp. Phys. **28**, 695 (2002)].

Translated by P. Pozdeev

Technical Physics Letters, Vol. 30, No. 5, 2004, pp. 370–373. From Pis'ma v Zhurnal Tekhnicheskoĭ Fiziki, Vol. 30, No. 9, 2004, pp. 44–51.

SH-Wave Intromission Concept¶

E. D. Guy[a,*] and S. J. Radzevicius[b,]**

[a] *US Army Corps of Engineers, Environmental & Remediation Section, Huntington, West Virginia 25701, USA*
[b] *ENSCO Inc., APA Division, Springfield, Virginia 22151, USA*
*e-mail: * Erich.D.Guy@usace.army.mil; ** radzevicius.stan@ensco.com*
Received June 9, 2003; in final form, October 21, 2003

Abstract—The existence of an *SH*-wave incidence angle for which the reflected amplitude is zero (*SH*-wave intromission angle) is established for the case of plane-wave scattering by a planar interface joining two homogeneous, isotropic, and linearly elastic half-spaces. Such an incidence angle is numerically shown to exist for two combinations of bimaterial interface properties. The *SH*-wave intromission angle is roughly parallel to the electromagnetic Brewster angle and the acoustic *P*-wave intromission angle, and the concept should find new applications for non-intrusive characterization of interfaces. *© 2004 MAIK "Nauka/Interperiodica".*

Introduction. Three types of elastic body waves composed of longitudinal primary (*P*) and transverse secondary (*SV* and *SH*) waves can exist in homogeneous, isotropic, and linearly elastic media. *P*-waves are polarized in the propagation direction and within the incidence plane, *SV*-waves are polarized orthogonal to the propagation direction and within the incidence plane, and *SH*-waves are polarized orthogonal to the propagation direction and within a plane that is orthogonal to the incidence plane. When elastic waves are incident on an interface joining media with different impedances, scattering (reflection and refraction/transmission) occurs. Amplitude and energy partitioning between scattered components is dependent on the incident wave type, the incidence angle, and the media impedances.

Amplitudes and energies of planar interface-scattered components from incident *P*- and *SV*-waves depend on media compressional velocities, shear velocities, and densities, whereas partitioning from incident *SH*-waves depends only on media shear velocities and densities [1]. For incident *P*- or *SV*-waves, mode-conversion can occur at the point of oblique incidence on a welded planar interface, with four possible wave types (reflected *P*, reflected *SV*, refracted *P*, and refracted *SV*) being generated. From an interface parallel to incident *SH*-wave polarization however, only scattered *SH*-waves are generated, regardless of the incidence angle. We have derived equations from the plane *SH*-wave reflection coefficient, which predict an angle of *SH*-wave incidence at which the reflected amplitude is zero (*SH*-wave intromission angle).

Theory. For plane *SH*-waves in homogenous, isotropic, and linearly elastic media, the reflection coefficient [1] for any angle of incidence can be written as

$$SH_1SH_1 = (Zs_1\cos\theta_{SH_1SH_1} - Zs_2\cos\theta_{SH_1SH_2})/(Zs_1\cos\theta_{SH_1SH_1} + Zs_2\cos\theta_{SH_1SH_2}), \quad (1)$$

where SH_1SH_1 is the reflection displacement amplitude coefficient, $\theta_{SH_1SH_1}$ is the incidence and reflection angle, $\theta_{SH_1SH_2}$ is the refraction angle, and Zs_1 and Zs_2 are the incident (medium 1) and refracted (medium 2) media shear impedances. Shear impedance is the product of medium shear velocity (Vs_1 or Vs_2) and density (ρ_1 or ρ_2).

The reflection coefficient is zero (only the refracted wave will remain) when the incidence angle is equal to the *SH*-wave intromission angle (θ_I), and this occurs when

$$Zs_1\cos\theta_I = Zs_2\cos\theta_{SH_1SH_2}. \quad (2)$$

To solve for θ_I,

$$Zs_1/Zs_2 = \cos\theta_{SH_1SH_2}/\cos\theta_I. \quad (3)$$

Using the relation $\sin^2 x + \cos^2 x = 1$ and Snell's law [1] to eliminate $\theta_{SH_1SH_2}$,

$$Zs_1/Zs_2 = (1-(Vs_2/Vs_1)^2\sin^2\theta_I)^{1/2}/(1-\sin^2\theta_I)^{1/2} \quad (4)$$

yields a solution for θ_I in terms of media shear velocities and shear impedances,

$$\theta_I = \sin^{-1}(1-(Zs_1/Zs_2)^2/(Vs_2/Vs_1)^2-(Zs_1/Zs_2)^2)^{1/2} \quad (5)$$

or a solution for θ_I in terms of media shear velocities

¶This article was submitted by the authors in English.

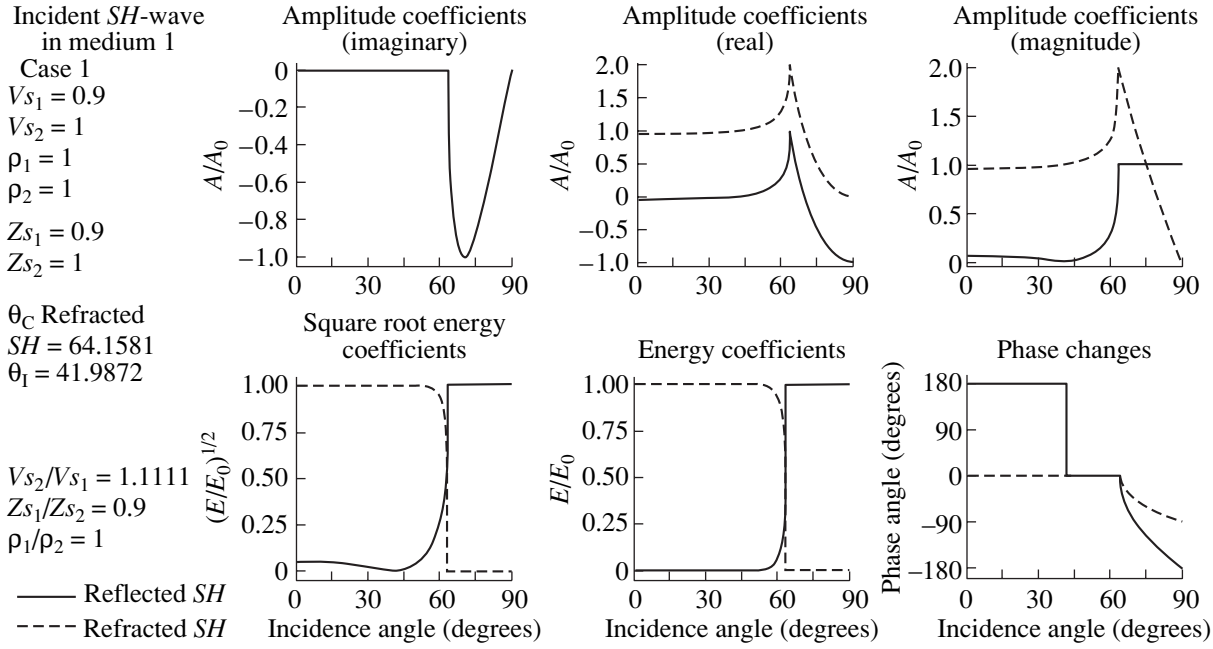

Fig. 1. *SH*-wave intromission angle (θ_I) occurrence for the case of an *SH*-wave incident on an interface with increasing shear velocity and shear impedance: $(Vs_2/Vs_1) > 1 > (Zs_1/Zs_2)$. Plots of amplitude coefficients, square root energy coefficients, energy coefficients, and phase changes as a function of incident angle for a plane *SH*-wave incident on a planar interface joining homogeneous, isotropic, and linearly elastic media were obtained using the PSHSV computer program [2]. A/A_0 is the ratio of a given scattered wave maximum amplitude particle displacement to that of the incident wave; E/E_0 is the ratio of a given scattered wave energy to that of the incident wave. Vs_1 and Vs_2 are the incident (medium 1) and refracted (medium 2) media shear velocities; ρ_1 and ρ_2 are the incident and refracted media densities; and Zs_1 and Zs_2 are the incident and refracted media shear impedances. A critical angle (θ_C) occurs for these media conditions. See text for discussion of this figure.

and densities,

$$\theta_I = \sin^{-1}((Vs_2/Vs_1)^2 - (\rho_1/\rho_2)^2/(Vs_2/Vs_1)^4 - (\rho_1/\rho_2)^2)^{1/2}, \quad (6)$$

where θ_I is a particular real angle of incidence between zero and 90°. To obtain a real solution to Eq. (5) or (6), the numerator and denominator in the respective equation must have the same sign, and the absolute value of the numerator must be equivalent to or less than the absolute value of the denominator in the respective equation. In terms of media shear velocities and shear impedances, Eq. (5) shows that these conditions will be met if $(Vs_2/Vs_1) \geq 1 \geq (Zs_1/Zs_2)$, or if $(Zs_1/Zs_2) \geq 1 \geq (Vs_2/Vs_1)$. When both $Vs_1 = Vs_2$ and $\rho_1 = \rho_2$, the *SH*-wave reflection coefficient is zero for all incidence angles.

Numerical examples. To illustrate *SH*-wave intromission angle existence, solutions to equations (obtained using the *PSHSV* computer program [2]) describing plane *SH*-wave scattering from a planar interface joining two homogeneous, isotropic, and linearly elastic half-spaces are presented. Shown in Figs. 1 and 2 are solutions for two example bimaterial interface physical properties cases. In Fig. 1 are solutions for the case of an incident *SH*-wave going from a medium with relatively low shear velocity to a medium with relatively high shear velocity. In Fig. 2 are solutions for the case of an incident *SH*-wave going from relatively high to relatively low shear velocity. Shear velocity (m/s) and density (g/cm^3) values used to obtain solutions are listed on the plots in Figs. 1 and 2.

Both Fig. 1 and Fig. 2 each contain six subplots showing how amplitude coefficients, square root energy coefficients, energy coefficients, and phase angles change as a function of incidence angle for each wave type generated at the interface for the respective case. The amplitude coefficients plotted in Figs. 1 and 2 were calculated using Eq. (1), and the following equation,

$$SH_1SH_2 = (2Zs_1\cos\theta_{SH_1SH_1})/(Zs_1\cos\theta_{SH_1SH_1} + Zs_2\cos\theta_{SH_1SH_2}), \quad (7)$$

where SH_1SH_2 is the refraction displacement amplitude coefficient. The reflection and refraction angle cosines in Eqs. (1) and (7) depend on the horizontal and vertical components of the slowness vector,

$$pp = (u^2 - \eta^2)^{1/2} = u\sin\theta, \quad (8)$$

$$\eta = (u^2 - pp^2)^{1/2} = u\cos\theta, \quad (9)$$

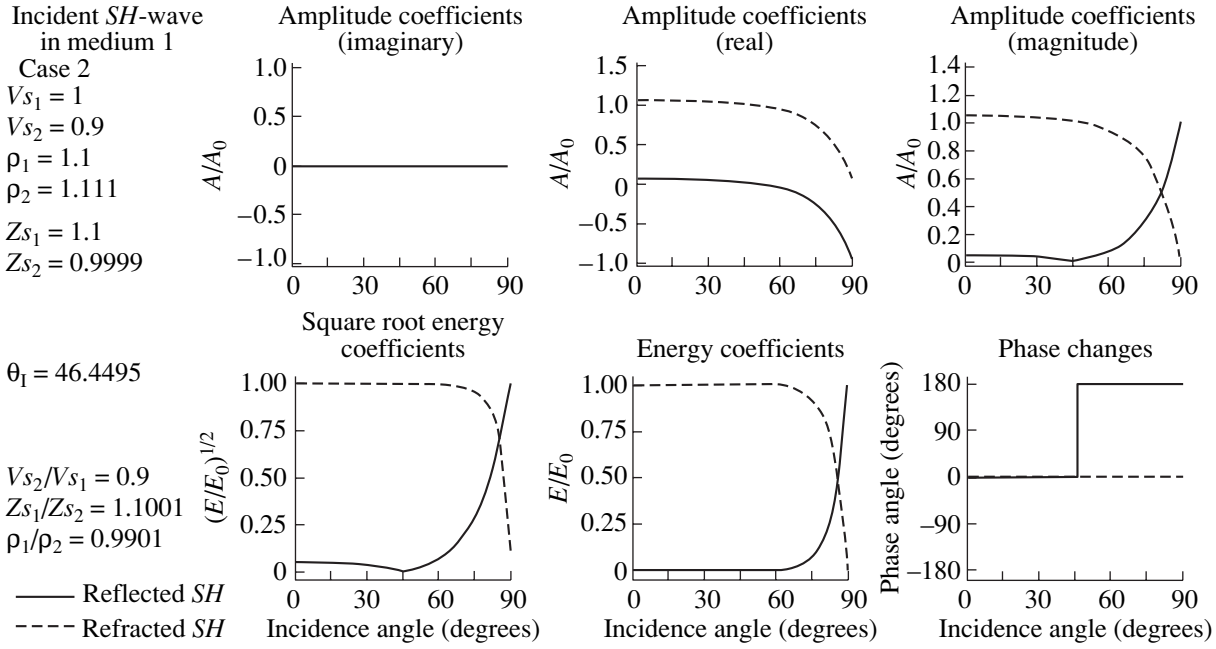

Fig. 2. *SH*-wave intromission angle (θ_I) occurrence for the case of an *SH*-wave incident on an interface with decreasing shear velocity and shear impedance: $(Zs_1/Zs_2) > 1 > (Vs_2/Vs_1)$. Notations are the same as in Fig. 1. See text for discussion of this figure.

where u is the slowness, pp is the horizontal slowness, η is the vertical slowness, and θ is the reflected or refracted ray angle measured from the normal. In terms of Vs_1 and Vs_2, the reflection and refraction angle cosines are

$$\cos\theta_{SH_1SH_1} = Vs_1((1/Vs_1^2) - pp^2)^{1/2}, \quad (10)$$

$$\cos\theta_{SH_1SH_2} = Vs_2((1/Vs_2^2) - pp^2)^{1/2}. \quad (11)$$

The square root energy and energy coefficients plotted in Figs. 1 and 2 were calculated as

$$ENSH_1SH_1 = SH_1SH_1, \quad (12)$$

$$ENSH_1SH_2 = (SH_1SH_2)((Zs_2\cos\theta_{SH_1SH_2})/(Zs_1\cos\theta_{SH_1SH_1}))^{1/2}, \quad (13)$$

$$ESH_1SH_1 = (ENSH_1SH_1)^2, \quad (14)$$

$$ESH_1SH_2 = (ENSH_1SH_2)^2, \quad (15)$$

where $ENSH_1SH_1$ and $ENSH_1SH_2$ are the normalized reflected and refracted square root energy coefficients and ESH_1SH_1 and ESH_1SH_2 are the reflected and refracted energy coefficients. Whereas reflected and refracted amplitudes do not necessarily sum to unity for a given angle of incidence, the energy coefficients (representing what fraction of an incident wave energy flux is reflected or refracted normal to the interface) must sum to unity for all angles of incidence.

The phase angles plotted in Figs. 1 and 2 were calculated using the following equation,

$$\varphi = \tan^{-1}(b/a), \quad (16)$$

where φ is the phase angle (between +180° and –180°, with 0° specified between quadrants 1 and 4) and a and b are the real and imaginary parts of a given displacement amplitude coefficient.

The Fig. 1 solutions were obtained for a case where bimaterial interface physical properties were such that $(Vs_2/Vs_1) > 1 > (Zs_1/Zs_2)$. Both an intromission angle (θ_I) and a critical angle (θ_C) are observed in the Fig. 1 subplots, and these results are consistent with Eq. (5) predictions. The critical angle occurs, as the incident medium velocity is less than that of the refracted medium; it is defined as

$$\theta_C = \sin^{-1}(Vs_1/Vs_2). \quad (17)$$

A 180° phase shift for the reflected *SH*-pulse occurs at θ_I (approximately 42°), and the phase is then constant until θ_C (approximately 64°) is reached, beyond which the reflected pulse phase is variable. From the real and imaginary parts of the reflection amplitude coefficient in Fig. 1, it is seen that θ_I occurs when the real portion of the reflected signal goes from negative to positive prior to θ_C. As the real portion of the reflected signal changes sign prior to all of the energy being reflected from the interface at θ_C, the reflected energy goes to zero at θ_I. Not all cases involving an incident *SH*-wave going from relatively low to relatively high shear velocity would result in θ_I occurrence. For instance, for a

case where the physical properties were such that $(Vs_2/Vs_1) = (Zs_1/Zs_2) > 1$, a θ_C would occur, but Eq. (5) predicts that θ_I would not occur.

The Fig. 2 solutions were obtained for a case where bimaterial interface physical properties were such that $(Zs_1/Zs_2) > 1 > (Vs_2/Vs_1)$. A θ_I is observed, but no θ_C is observed, in the subplots of Fig. 2, and these results are consistent with Eq. (5) predictions. The reflected *SH*-pulse phase is constant until the θ_I (approximately 46°), at which the reflection amplitude goes to zero and beyond which a 180° phase shift of the reflected pulse occurs. From the real and imaginary parts of the reflection amplitude coefficient in Fig. 2, it is seen that θ_I occurs when the real portion of the reflected signal goes from positive to negative. Not all cases involving an incident *SH*-wave going from relatively high to relatively low shear velocity would result in θ_I occurrence. For instance, for a case where the physical properties were such that $1 > (Vs_2/Vs_1) = (Zs_1/Zs_2)$, Eq. (5) predicts that a θ_I would not occur.

Conclusions. An *SH*-wave intromission angle occurs for a given incidence angle when the interface is characterized by increasing velocity and impedance and $(Vs_2/Vs_1) \geq 1 \geq (Zs_1/Zs_2)$ or decreasing velocity and impedance and $(Zs_1/Zs_2) \geq 1 \geq (Vs_2/Vs_1)$. Recognition and utilization of the *SH*-wave intromission concept should lead to new non-intrusive interface characterization applications (as in the widely utilized electromagnetic Brewster angle in optics [3–5] and the *P*-wave intromission angle in acoustics [6, 7]) and should stimulate further investigations of this effect.

REFERENCES

1. P. M. Shearer, *Introduction to Seismology* (Cambridge University Press, New York, 1999).
2. E. D. Guy, S. J. Radzevicius, and J. P. Conroy, Comput. Geosci. **25**, 569 (2003).
3. C. A. Balanis, *Advanced Engineering Electromagnetics* (Wiley, New York, 1989).
4. L. M. Brekhovskikh, *Waves in Layered Media* (Academic, New York, 1980).
5. M. Born and E. Wolf, *Principles of Optics* (Cambridge University Press, New York, 1999).
6. L. J. Ziomek, *Fundamentals of Acoustic Field Theory and Space Time Signal Processing* (CRC Press, Ann Arbor, 1995).
7. R. S. Winokur and J. C. Bohn, J. Acoust. Soc. Am. **44**, 1130 (1968).

Technical Physics Letters, Vol. 30, No. 5, 2004, pp. 374–376. Translated from Pis'ma v Zhurnal Tekhnicheskoĭ Fiziki, Vol. 30, No. 9, 2004, pp. 52–56.

Edge-Type Josephson Junctions with Silicon Nitride Spacer

S. N. Vdovichev*, A. Yu. Klimov, Yu. N. Nozdrin, and V. V. Rogov

Institute for Physics of Microstructures, Russian Academy of Sciences, Nizhni Novgorod, Russia

** e-mail: vdovichev@ipm.sci-nnov.ru*

Received November 4, 2003

Abstract—Edge-type Josephson junctions with a silicon nitride spacer possessing small capacitance have been fabricated at the butt-joint of two superconducting niobium films. The main results of experimental investigation of the electrical properties of these structures are presented. © *2004 MAIK "Nauka/Interperiodica".*

Niobium based Josephson junctions are among the main elements of modern cryoelectronics. This Letter reports on the results of investigation of edge-type Nb–SiN_x–Nb Josephson junctions characterized by a small stray capacitance, a critical current within 10–1000 μA, and a normal resistances of 1–10 Ω. Such junctions can be used in microwave devices (adders, multipliers, etc.) [1], programmable voltage standards [2], and elements of quantum logics (with a stray capacitance on the order of 10^{-15} to 10^{-16} F and the critical current not exceeding 10 μA) [3].

Figure 1 shows a schematic diagram of the cross section of the proposed edge-type Nb–SiN_x–Nb Josephson junction. A distinctive feature of this junction is that the second superconducting electrode forms a butt-joint with the first electrode, rather than covering it over a dielectric interlayer as in conventional structures [4, 5]. The edge-type design allows the stray capacitance of the junction to be significantly reduced. Josephson junctions of this geometry can be used for the investigation of submicron magnetic structures [6, 7]. To the best of our knowledge, such edge-type Josephson junctions are reported for the first time. Below, we present the main results of experimental investigation of the electrical properties of new junctions.

The Josephson junctions were obtained on standard silicon wafers. By means of magnetron sputtering, the substrate was sequentially covered with the first Nb (Nb^I) layer (~100 nm), the amorphous dielectric layer of SiN_x (~50 nm), and the metallic film of NiCr (~200 nm), after which the latter film was patterned as required using standard photolithographic techniques. The open regions of Nb^I/SiN_x were subjected to reactive ion-plasma etching to open the edge of the Nb^I layer. Then, the SiN_x spacer and the second Nb (Nb^{II}) film were deposited by magnetron sputtering after preliminary cleaning of the Nb^I film edge by ion etching in Ar atmosphere. Note also that the SiN_x spacer separating the two Nb electrodes was oxidized after deposition so as to provide for "healing" of the possible microscopic through holes in the insulator. The junction structure formation was completed by anodic etching of the NiCr film and photolithographic patterning of the second electrode. The junction area was equal a fraction of a square micron. The above method of obtaining edge-type Josephson junctions showed good reproducibility, and the properties of junctions were stable in time, which is very important for practical applications.

The electrical properties of the edge-type Josephson junctions with spacer thicknesses within 1–5 nm were studied by conventional four-terminal techniques in a helium cryostat. Figure 2 presents the typical current–voltage (*I–U*) characteristics observed for several junctions with various spacer thicknesses and shows the effects of applied magnetic field and microwave irradiation on these curves. The main features of the observed current–voltage characteristics are as follows:

(i) the absence of hysteresis in the *I–U* curves, which was indicative of a small (below unity) values of the dimensionless MacCumber–Stewart capacitance parameter $\beta_c = (2e/\hbar)I_c R_N^2 C$ and allowed the junction capacitance C to be estimated below 10^{-11} to 10^{-12} F (estimates of the C value based on the junction geometry and the typical parameters of amorphous Si_3N_4 give values on the order of 10^{-15} to 10^{-16} F);

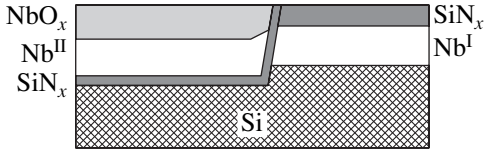

Fig. 1. Schematic diagram of the cross section of the edge-type Nb–SiN_x–Nb Josephson junction.

(ii) the presence of a kink at $V_g \sim 1.8$ mV corresponding to the bandgap of niobium;

(iii) considerable excess current;

(iv) manifestations of both dc and ac Josephson effects.

Under the action of an intense microwave radiation ($f = 80$ GHz), the *I–U* curves of the junctions exhibited pronounced Josephson current steps at a voltage of $U_n = (h/2e)fn \approx 180n$ μV ($n = 1, 2, \ldots$). This voltage and the critical current exhibit oscillations with increasing microwave power.

The dependence of the critical current of the Josephson junctions on the applied magnetic field, $I_c(H)$, is close to the usual Fraunhofer diffraction pattern with a period inversely proportional to junction width. The typical diffraction patterns observed for two junctions of different width fabricated in the same technological cycle are presented in Fig. 3a. The oscillation period was about five times as small as that predicted by a simple calculation using the "effective" Josephson contact area [8]. The discrepancy can be related to the demagnetizing effect of superconducting banks of the junction, leading to the effective field buildup in the junction region [9]. It should be noted that the theory of such junctions is not completely developed [10]. The large number of oscillations in the diffraction pattern is evidence of the homogeneity of the junction and the absence of shorts in the spacer. Numerical estimates show that the Josephson penetration length even at the maximum current density (~10^5 A/cm^2) does not exceed the junction width, which implies that the contacts are small.

Figure 3b shows the temperature dependence of the critical current, $I_c(T)$, measured for a junction with relatively large critical current. The dependence is close to linear in the entire temperature range studied. As is known, this behavior is characteristic of superconductor–insulator–metal–superconductor (SINS) [8] or superconductor–semiconductor–superconductor (S–Sm–S) [11] junctions.

In this stage of investigation, the structure of the spacer was not studied directly and can only be judged by some indirect data. We have measured the characteristics of junctions with different spacer thicknesses and established the main trends in the dependence of these parameters on the SiN_x layer thickness. For this purpose, a series of edge-type junctions with various spacer thicknesses were fabricated in the same technological cycle. As the spacer thickness monotonically decreased from 5 to 1 nm along the substrate length, the critical current of the junction varied within 10–1000 μA (10^2–10^5 A/cm^2), while the junction resistance changed from 5 to 1 Ω.

From our estimates of the average deposition rate of SiN_x, a critical current of 500 μA for a junction area of 0.8 μm^2 corresponds to a spacer thickness of 2 nm. The dependence of the critical current on the spacer thickness has an exponential character. The junction resistance monotonically increases with the spacer thickness by approximately a linear law. Such dependences of the critical current and resistance of the junction are frequently observed for semiconductor interlayers [8] and are determined by features of the junction technology.

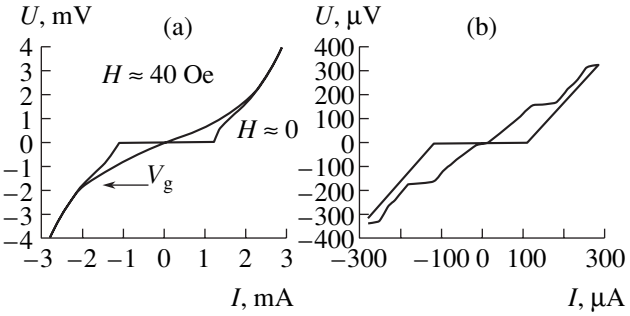

Fig. 2. The effect of (a) magnetic field and (b) microwave radiation ($f = 80$ GHz) on the typical current–voltage characteristics of the edge-type Josephson junctions.

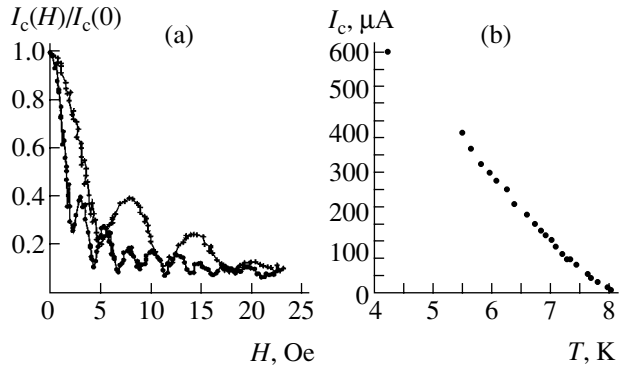

Fig. 3. The typical curves of (a) $I_c(H)/I_c(0)$ for the junctions with spacer thicknesses 5 and 8 μm and (b) $I_c(T)$ for the 5-μm-wide junction.

In the following experiments, we plan to study the electrical properties of the edge-type Josephson junctions at temperatures below 4.2 K, to elucidate the structure of the SiN_x spacer and its influence on the junction properties, and to obtain and study Josephson junctions with critical currents below 10 μA.

Acknowledgments. The authors are grateful to A.A. Fraerman and A.V. Samokhvalov for fruitful discussions of the obtained results.

This study was supported by the Russian Foundation for Basic Research (project no. 03-02-16774) and the Quantum Macrophysics Program of the Russian Academy of Sciences.

REFERENCES

1. K. K. Likharev, *Introduction to the Dynamics of Josephson Junctions* (Nauka, Moscow, 1985).

2. C. A. Hamilton, Rev. Sci. Instrum. **71**, 3611 (2000).
3. L. B. Ioffe, V. B. Geshkenbein, M. V. Feigelman, *et al.*, cond-mat/9809116 (1998).
4. R. F. Broom, A. Ooesenbrug, and W. Walter, Appl. Phys. Lett. **37**, 237 (1980).
5. A. L. Gudkov, M. Yu. Kupriyanov, and K. K. Likharev, Pis'ma Zh. Tekh. Fiz. **11**, 1423 (1985) [Sov. Tech. Phys. Lett. **11**, 587 (1985)].
6. A. Y. Aladyshkin, A. A. Fraerman, S. A. Gusev, *et al.*, J. Magn. Magn. Mater. **258**–**259**, 406 (2003).
7. A. V. Samokhvalov, Pis'ma Zh. Éksp. Teor. Fiz. **78**, 822 (2003) [JETP Lett. **78**, 369 (2003)].
8. A. Barone and G. Paterno, *Physics and Applications of the Josephson Effect* (Wiley, New York, 1982; Mir, Moscow, 1984).
9. J. Gu, W. Cha, and S. Namba, J. Appl. Phys. **50**, 6437 (1979).
10. V. G. Kagan, V. V. Dobrovitski, J. R. Clem, *et al.*, Phys. Rev. B **63**, 144501 (2001).
11. V. N. Gubankov, S. A. Kovtonyuk, and V. P. Koshelets, Zh. Éksp. Teor. Fiz. **89**, 1335 (1985) [Sov. Phys. JETP **62**, 773 (1985)].

Translated by P. Pozdeev

Technical Physics Letters, Vol. 30, No. 5, 2004, pp. 377–379. Translated from Pis'ma v Zhurnal Tekhnicheskoĭ Fiziki, Vol. 30, No. 9, 2004, pp. 57–62.

Numerical Calculation and Experimental Study of Operation of a High-T_c Superconductor Bolometer with Active Electrothermal Feedback

K. V. Ivanov, I. A. Khrebtov*, and A. D. Tkachenko

Vavilov Optical Institute, State Scientific Center of the Russian Federation, St. Petersburg, 190164 Russia

** e-mail: iakhrebtov@yahoo.com*

Received November 18, 2003

Abstract—Based on the proposed model, we have numerically calculated and experimentally studied operation of a high-T_c superconductor bolometer in the regime with active negative electrothermal feedback (NEF). The NEF regime allows the bolometer operation speed to be controlled, which expands the possible application field. The influence of the NEF on the sensitivity, response time, and detectivity of the bolometer was studied.

The use of high-T_c superconductor bolometers is sometimes limited because of the impossibility of simultaneously providing both a high sensitivity and a fast operation speed. This problem can be partly solved by means of the negative electrothermal feedback (NEF) in either passive or active regime [1–5]. In the active regime, the system involves an external negative feedback loop with an electronic amplifier [5].

The mechanism of NEF action is illustrated in Fig. 1. At the system input, the optical power P_{opt} absorbed by the bolometer is converted with the responsivity S_V^* into an electric signal transmitted with the bridge coefficient M_1 to the preamplifier K. Here, S_V^* is the responsivity of a bolometer without feedback for an absorption coefficient of $\varepsilon = 1$,

$$S_V^* = \frac{U_b\beta}{G}\frac{1}{1 + i\omega\tau_0}, \quad (1)$$

where $\omega = 2\pi f$, f is the frequency, β is the temperature coefficient of resistance of the high-T_c superconductor film, G is the thermal loss coefficient, and τ_0 is the thermal time constant.

For an equal-arm Winston bridge, the transmission coefficient is $M_1 = 0.5$. The amplified signal is transmitted via a divider with the coefficient $F = R_I/(R_I + R_f)$, where $R_f = 100$ kΩ is the feedback loop resistance, to the bridge supply branch and, divided by the bridge coefficient M_2, back to the bolometer in the form of the Joule power correction ΔP. This change in the Joule power under the action of the active NEF tends to compensate the action of P_{opt} so that $R_b \longrightarrow R_I$.

An analysis of the scheme in Fig. 1 leads to the following expression for the bolometer responsivity in the NEF regime for $\varepsilon = 1$:

$$S_V = \frac{1}{I_b}\frac{0.5L_0}{1 + 0.5L_0FK}\frac{1}{1 + i\omega\tau_{eff}}. \quad (2)$$

Here, $L_0 = P\beta/G$ is the feedback coefficient, $P = I_b^2 \times R_b$ is the Joule power dissipated in the bolometer, I_b is the bias current, K is the amplifier gain, and τ_{eff} is the effective time constant given by the formula

$$\tau_{eff} = \frac{\tau_0}{1 + 0.5L_0FK}. \quad (3)$$

Substituting noise power for the optical radiation power in the scheme of Fig. 1 and performing transformations, we obtain a frequency dependence of the noise voltage reduced to the bridge output:

$$U_n = U_n^*\frac{(1 + \omega^2\tau_0^2)^{1/2}}{((1 + 0.5L_0FK)^2 + \omega^2\tau_0^2)^{1/2}}, \quad (4)$$

where

$$U_n^* = \sqrt{U_J^2 + (0.5U_{1/f})^2 + (0.5U_{ph})^2}, \quad (5)$$

U_J is the Johnson noise voltage; $0.5U_{1/f}$ and $0.5U_{ph}$ are the voltages due to the $1/f$ noise and the phonon noise, respectively, reduced to the bridge output without NEF.

The experiments were performed with a GdBaCuO bolometer fabricated on a 2 × 2-mm Si/Si_3N_4 membrane using a method described by Nivelle *et al.* [2].

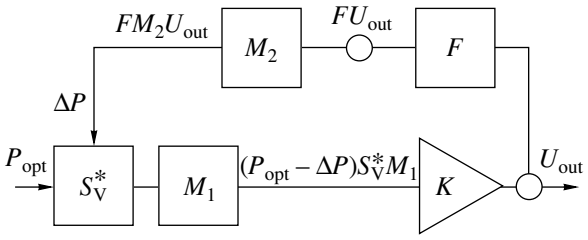

Fig. 1. Schematic diagram of the negative electrothermal feedback (see the text for explanations).

The bolometer had a sensitive area of 0.85×0.85 mm and an absorption coefficient of $\varepsilon = 0.7$ for a radiation wavelength of $\lambda = 3$ μm. The other characteristics are presented in the table. The bolometer was operated in a constant bias current mode (CCM) and in an active NEF regime, being connected via an equal-arm Winston bridge cooled to a temperature of ≈80 K. The bolometer resistance at the working point was $R_b = 4.7$ kΩ.

Operation in the NEF regime, in comparison to the CCM, was characterized by increased response speed and decreased responsivity S_V (Fig. 2). The frequency dependence of the responsivity in the active NEF regime was calculated using formula (2), while the CCM with a positive electrothermal feedback was described using the expression for S_V obtained in [2]. As can be seen from Fig. 2, the results of calculations are in good agreement with the experimental data.

Operating in the active NEF regime, the bolometer exhibited noise suppression at low frequencies (Fig. 3). The discrepancy between calculated and experimentally measured dependences can be explained by a stronger dependence of the $1/f$ noise voltage of the frequency and current for the bias currents above the thermal instability threshold. At high frequencies, where the active NEF action is not as pronounced, the measured noise is close to the Johnson noise in cooled resistors of the bridge.

Despite the noise suppression observed in the active NEF regime, the detectivity defined as $D^* = A^{1/2}/NEP$ (where A is the receiving area and $NEP = U_n/S_V^*$ is the noise equivalent power) exhibited no increase in the frequency interval from 1 to 10 Hz. The lower detectivity of the bolometer operating in the NEF regime in this frequency interval can be explained by excessive $1/f$ noise and a lower responsivity in this regime. In the range of frequencies $f > 10$ Hz, the responsivity in the constant bias current mode begins to decrease, while that in the NEF regime is retained at a constant level (Fig. 2). As a result, the detectivity in the active NEF regime is greater than that in the CCM. This is favored, among other factors, by a low level of the Johnson noise in cooled resistors of the bridge and by the use of a low-noise preamplifier.

It should be noted that bolometers are frequently characterized by the ratio $D^*/\tau_{eff}^{1/2}$ at $f = f_{cutoff}$; in the active NEF regime, this parameter amounts to 8.3×10^{10} (cm Hz)/W, which is better as compared to 6.1×10^{10} (cm Hz)/W for the CCM operation. The experimental values of D^*, NEP, S_V, and U_n at the cutoff frequency f_{cutoff} are presented in the table. In addition, it was experimentally established that a bolometer oper-

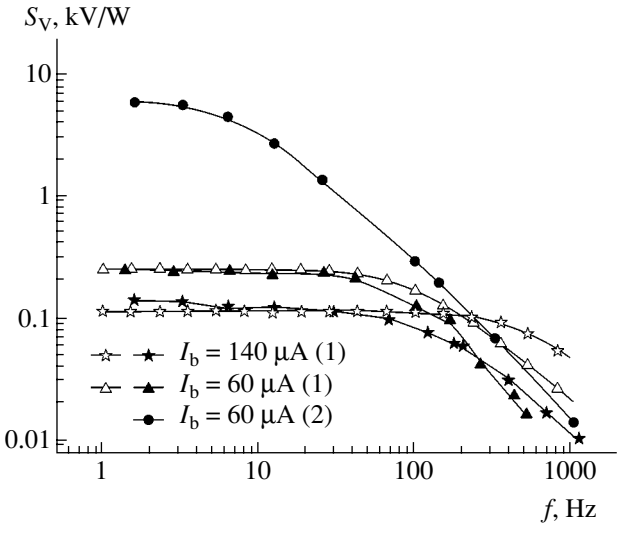

Fig. 2. Experimental (black symbols) and calculated (open symbols) frequency dependences of the responsivity of high-T_c superconductor bolometers operating in the (1) NEF and (2) constant bias current modes.

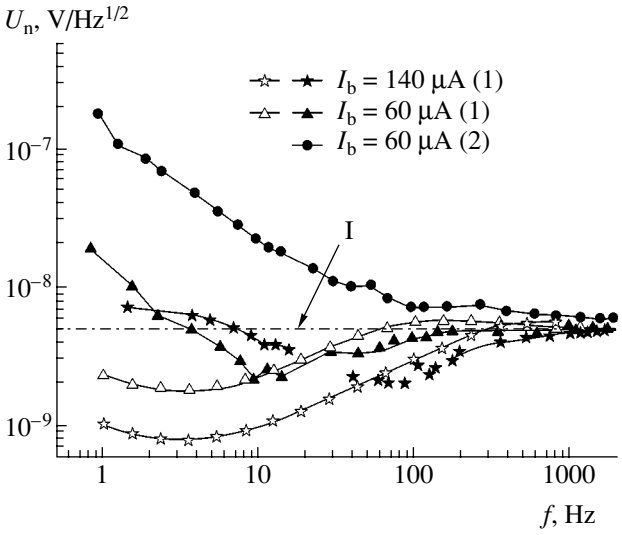

Fig. 3. Experimental (black symbols) and calculated (open symbols) frequency dependences of the noise voltage in high-T_c superconductor bolometers operating in the (1) NEF and (2) constant bias current modes (line I shows the Johnson noise of the bridge resistance).

The parameters of high-T_c superconductor bolometers operating in different regimes

Parameter	Operation regime		
	constant current mode	negative electrothermal feedback	
T_s, K	84.3	83.6	79.2
β, K^{-1}	0.9	–	–
G, W/K		1.3×10^{-5}	
I_b, μA	60	60	140
τ_{eff}, ms	23	2.8	1.6
f_{cutoff}, Hz	7	56	100
S_V, V/W	3500	179	86
U_n, nV/Hz$^{1/2}$	32	3.6	2.2
NEP, W/Hz$^{1/2}$	0.9×10^{-11}	2.0×10^{-11}	2.6×10^{-11}
D^*, (cm Hz$^{1/2}$)/W	9.2×10^9	4.3×10^9	3.3×10^9
$D^*/\tau_{eff}^{1/2}$, (cm Hz)/W	6.1×10^{10}	8.0×10^{10}	8.3×10^{10}

Note: T_s is the substrate temperature; the absolute values of responsivity were measured using a blackbody radiator with a cavity temperature of $T = 373$ K ($\lambda_{max} \approx 7$ μm).

ating in the NEF regime retains the linearity of conversion to at least tenfold greater maximum values of the input optical power as compared to that for the CCM.

Conclusions. A bolometer operating in the NEF regime with an equal-arm Winston bridge cooled to a working temperature of ≈80 K showed a detectivity of 3.3×10^9 (cm Hz$^{1/2}$/W) at an effective time constant of 1.6 ms. Although the detectivity is about 2.8 times smaller than that in the constant bias current mode, the operation speed in the NEF regime increases by a factor of 14. The experimental results are quite well described by the proposed calculation model.

Acknowledgments. The authors are grateful to W. Michalke for his help in preparing bolometers to experiments.

This study was supported by the Ministry of Industry, Science, and Technology of the Russian Federation.

REFERENCES

1. H. Neff, J. Laukemper, I. A. Khrebtov, *et al.*, Appl. Phys. Lett. **66**, 2421 (1995).
2. M. J. M. E. de Nivelle, M. P. Bruijn, R. de Vries, *et al.*, J. Appl. Phys. **82**, 4719 (1997).
3. A. T. Lee, J. M. Gildemeister, S.-F. Lee, and P. L. Richards, IEEE Trans. Appl. Supercond. **7**, 2378 (1997).
4. H. Neff, A. M. N. Lima, G. S. Deep, *et al.*, Appl. Phys. Lett. **76**, 640 (2000).
5. E. Steinbeis, J. Opt. Technol. **68**, 290 (2001).

Translated by P. Pozdeev

Technical Physics Letters, Vol. 30, No. 5, 2004, pp. 380–382. Translated from Pis'ma v Zhurnal Tekhnicheskoĭ Fiziki, Vol. 30, No. 9, 2004, pp. 63–67.

AlGaN/GaN HEMTs Grown by Ammonia MBE

V. V. Volkov*, V. P. Ivanova, Yu. S. Kuz'michev, S. A. Lermontov, Yu. V. Solov'ev, D. A. Baranov, A. P. Kaĭdash, D. M. Krasovitskiĭ, M. V. Pavlenko, S. I. Petrov, Yu. V. Pogorel'skiĭ, I. A. Sokolov, M. A. Sokolov, M. V. Stepanov, and V. P. Chalyĭ

"Svetlana–Elektronpribor" Corporation, St. Petersburg, Russia

"Scientific and Technological Equipment" Corporation, St. Petersburg, Russia

** e-mail: support@semiteq.ru*

Received November 18, 2003

Abstract—The experimental technology and characteristics of domestic AlGaN/GaN high electron mobility transistors are described. The results show good prospects for further development. © *2004 MAIK "Nauka/Interperiodica".*

Introduction. In recent decades, gallium nitride and related ternary compounds possessing a unique combination of physical properties have become one of the most promising systems of semiconductor compounds. A high potential of group III nitrides in the field of optoelectronic devices for the UV and visible spectral range has been realized to a considerable extent. These compounds are also characterized by significant band breaks at heteroboundaries, pronounced polarization effects, high values of the electron drift velocity (within $(1.5–3) \times 10^7$ cm/s in an electric field on the order of 100 kV/cm), large values of breakdown fields, relatively high thermal conductivity, etc.

Owing to these properties of the base materials, the power characteristics of group III nitride based devices are significantly (sometimes tenfold) higher than the analogous parameters of GaAs and SiC based devices. Advantages of the nitride based devices are especially pronounced at elevated working temperatures (up to 400°C). This opens wide possibilities in solving difficult problems related, in particular, to the development of military equipment (placing special demands upon the characteristics of devices and components) and the systems of aircraft traffic control, satellite tele- and radiocommunications, environmental monitoring, and many others.

Various types of nitride based microwave transistors (HEMT, MESFET, etc.) have been developed, which generally confirm the above statement concerning good prospects of such devices [1–3]. The most widely used methods of fabrication of the nitride device heterostructures are metalorganic vapor phase epitaxy (MOVPE) and molecular beam epitaxy (MBE). The main requirements for transistor heterostructures are a high structural perfection of AlGaN and GaN layers and their interfaces, as well as a high resistance of the buffer layer. Meeting these requirements provides for the formation of a conducting channel (in particular, two-dimensional), with a sheet electron density on the order of 10^{13} cm^{-2} and an electron mobility above $\mu = 1000$ cm^2/(V s). The main stages in nitride device technology are the formation of mesa structures, low-ohmic contacts to the source and drain electrodes, and a stable Schottky barrier at the gate electrode.

This Letter describes the experimental technology and static output characteristics of high electron mobility transistors (HEMTs) based on AlGaN/GaN heterostructures grown by MBE on sapphire substrates. Being among the best devices of this type obtained in Russia,

$Al_{0.3}Ga_{0.7}N$ (80 Å)
$Al_{0.3}Ga_{0.7}N$:Si (80 Å)
$Al_{0.3}Ga_{0.7}N$ (40 Å)
GaN (500 Å)
$Al_xGa_{1-x}N$ (600 nm) $0.3 < x < 0.8$
AlN (200 Å)
Al_2O_3

Fig. 1. Schematic diagram of the AlGaN/GaN HEMT heterostructure.

these HEMTs show a high potential for further development.

Experimental. AlGaN/GaN heterostructures for HEMTs (Fig. 1) on (0001)-oriented sapphire substrates were grown in an EPN-2 setup specially designed for the MBE of group III nitrides, using ammonia as the source of active nitrogen [4]. The main difference of our heterostructures [5] from the most widely used HEMT configuration is the presence of a relatively thick (0.6 μm) AlGaN buffer layer ensuring high (above 150 V) breakdown voltages for the bottom part of the HEMT structure. This layer is followed by a 500-Å-thick semi-insulating GaN layer covered by a modulation-doped $Al_{0.3}Ga_{0.7}N$ layer with a total thickness of 200 Å. The subsequent spacer, donor, and barrier sublayers are 40, 80, and 80 Å thick.

Prior to depositing ohmic contacts, the structure was etched in a hydrochloric acid solution and in hydrogen peroxide–ammonia solutions, followed by rinsing and drying in acetone vapor. The ohmic contacts were formed by means of explosive photolithography using 0.2-μm-thick Ti/Al composite metallization. After deposition of the ohmic contacts, the device structures were annealed in N_2 at 830°C for 50 s and the electrical parameters of the contacts were determined by the long line technique. The electric isolation between elements (mesa structure) on the wafer was obtained by reactive ion etching in $SiCl_4$ plasma to a depth of 0.3 μm. A 1-μm long gate electrode was formed by means of explosive photolithography using 0.15-μm-thick Ni/Au composite metallization.

Results and discussion. According to the results of the Hall effect measurements, the HEMT heterostructures have a sheet electron density in the channel on the order of 1×10^{13} cm^{-2} and a room-temperature electron mobility of 400–600 cm^2/(V s). In nitrogen, the mobility increased up to 1000–2000 cm^2/(V s) and the room-temperature electron density remained unchanged, which was evidence of the two-dimensional electron gas formation at the AlGaN/GaN interface.

According to the data of atomic force microscopy measurements, the roughness of transistor heterostructures ranges within 0.9–3.3 nm. The crystal structure perfection was checked by X-ray diffraction. For a 1-μm-thick test sample of gallium nitride grown under the same conditions as those used in the device technology, the halfwidths of the X-ray rocking curves obtained in the Θ and Θ–2Θ scans for a symmetric Bragg reflection were 276″ and 55″, respectively. The total number of defects in the grown structures was not specially evaluated, but we believe that it amounts to no less than 5×10^9 cm^{-2}.

After the device topology formation, the resistances of source and drain ohmic contacts were 2.5–3 Ω mm and the contact resistivity was $\rho_c = (6–8) \times 10^{-6}$ Ω mm.

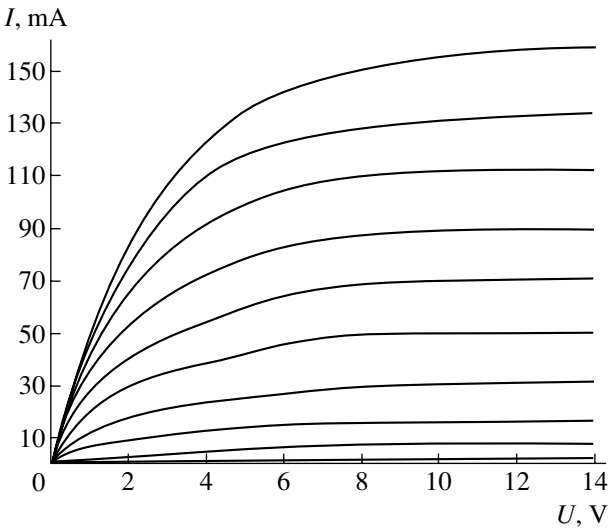

Fig. 2. Static current–voltage characteristics of Schottky-gate field-effect transistors based on epitaxial AlGaN/GaN heterostructures (the gate voltage was varied by $\Delta U = 0.5$ V steps).

The buffer stray currents after mesa structure etching were negligibly small: $I = 2–3$ nA per 50 V (both in the dark and on illumination). The gate–source nonideality coefficient was 1.18 V, the source–gate breakdown voltage was above 25 V, and the Schottky barrier height (determined from the *C–V* measurements) amounted to 0.93–1.02 eV.

Figure 2 shows the static current–voltage (*I–U*) characteristics of AlGaN/GaN HEMT heterostructures schematically depicted in Fig. 1. As can be seen, the devices exhibit stable saturation and controllability, a cutoff voltage of 4 V, a transconductance of 65–80 mS/mm, a saturation current of 165–180 mA/mm, and a source–drain breakdown voltage of 50 V.

The main disadvantages of obtained HEMTs are comparatively low values of the working current and transconductance, which are probably explained by relatively high values of the device resistance and the electron mobility in the channel, respectively. The device characteristics can be increased by further developing the heterostructure growth technology, primarily through improvement of the structural perfection of both the whole device material and the channel material. Additional gain in the device performance can be achieved through a decrease in the interfacial roughness, optimum doping of the upper AlGaN layer, and further development of the device technology (in particular, the regime of ohmic contact fusion) and design (smaller gate length).

Thus, we have experimentally verified the technology of Schottky-gate field-effect transistors based on epitaxial AlGaN/GaN heterostructures. The obtained static performance characteristics of these Schottky-

barrier transistor structures indicate that the proposed technology of AlGaN/GaN heterostructures grown by ammonia MBE on sapphire substrates can be used for the fabrication of HEMTs of various types.

REFERENCES

1. R. Behtash, H. Tobler, M. Neuburger, *et al.*, Electron. Lett. **39**, 626 (2003).
2. L. Shen, S. Heikman, B. Moran, *et al.*, IEEE Trans. Electron Devices **48**, 586 (2001).
3. Y.-F. Wu, D. Kapolnek, J. P. Ibbetson, *et al.*, IEEE Electron Device Lett. **22**, 457 (2001).
4. A. V. Alekseev, A. N. Volkov, D. M. Krasovitskiĭ, *et al.*, Izv. Vyssh. Uchebn. Zaved. Mater. Élektron. Tekh., No. 1, 32 (2001).
5. RF Pat. Appl. No. 2003109501/28(010201) (Accepted 2003).

Translated by P. Pozdeev

Technical Physics Letters, Vol. 30, No. 5, 2004, pp. 383–384. Translated from Pis'ma v Zhurnal Tekhnicheskoĭ Fiziki, Vol. 30, No. 9, 2004, pp. 68–72.

The Domain Structure and Barkhausen Effect in $Fe_{78}B_{12}Si_9Ni_1$ Amorphous Alloy

T. M. Breczko[a], N. Ye. Skryabina[b], L. V. Spivak[b,*], and M. J. Bramowicz[a]

[a] *University of Varmia and Mazury, Olsztyn, Poland*

[b] *Perm State University, Perm, Russia*

* *e-mail: levspivak@permonline.ru*

Received October 28, 2003

Abstract—There is no correlation between dimensions of the domain structure elements in an $Fe_{78}B_{12}Si_9Ni_1$ amorphous alloy ribbon and the Barkhausen effect characteristics in this alloy in various states: initial, hydrogenated, and annealed. Traditional notions of the Barkhausen effect, the nature of which is related to the domain size and the domain wall mobility, are inapplicable to disordered systems such as magnetically soft amorphous metal alloys. © *2004 MAIK "Nauka/Interperiodica".*

Introduction. The introduction of hydrogen (deuterium) into iron based amorphous metal alloys leads to a severalfold increase in the integral emf characterizing the Barkhausen effect, expansion of the range of magnetic fields in which the Barkhausen noise oscillations (jumps) are observed, and increase in the number of the Barkhausen jumps of large amplitude [1–3]. Annealing at temperatures above 300°C produces a qualitatively similar influence on the Barkhausen effect in such alloys. In the course of storage of a hydrogen-saturated amorphous alloy sample, the Barkhausen emf and other parameters of the Barkhausen noise spectrum return to the values characteristic of the initial (nonhydrogenated) state. The time of relaxation to this state amounts to several days. In annealed samples, changes in the Barkhausen emf are retained for arbitrarily long periods of time. Therefore, samples used in investigations of the domain structure after storage contain virtually no hydrogen. Such samples show only the aftereffect of hydrogenation on the domain structure of the material.

We have studied the domain structure of amorphous metal alloys using a new approach based on the measurement of magnetization in microscopic volumes of the sample.

Method of investigation. The experimental procedure involved the two-side hydrogen saturation of a 30-μm-thick amorphous metal alloy ribbon in an acid electrolyte at a cathode current density of 50 A/m^2. The Barkhausen emf (ε_B) and its frequency spectrum were measured using a specially designed setup. The Barkhausen transducer comprised an inductor coil, generating a magnetic field in the sample volume, and a measuring coil, detecting the magnetic flux variations related to the Barkhausen jumps. The frequency of magnetic field switching was 50 Hz. The samples exhibited homogeneous magnetization reversal in the volume. The thermal treatment (annealing) was performed by keeping a sample in a vacuum furnace at a preset temperature for 30 min.

The room-temperature domain structure of a sample was studied by double scans in a magnetic force microscope (MFM). In the first scan, the MFM measured the sample surface topography, and in the second scan, the phase shift $\Delta\Phi$ of the cantilever oscillations induced by a magnetic field of the domain. This phase shift can be expressed as [4]

$$\Delta\Phi = \frac{Q}{k}\left(q\frac{\partial H_z}{\partial z} + m_x\frac{\partial^2 H_x}{\partial z^2} + m_y\frac{\partial^2 H_y}{\partial z^2} + m_z\frac{\partial^2 H_z}{\partial z^2}\right),$$

where Q is the quality factor of the MFM cantilever resonance, q is the effective magnetic charge of the MFM tip, k is the elastic constant of the cantilever, (m_x, m_y, m_z) is the magnetic moment of the tip, and (H_x, H_y, H_z) is the magnetic moment of the domain.

The MFM probe was a tip coated with a 30- to 40-nm-thick layer of cobalt, mounted on a cantilever. The probe was magnetized in the axial direction in a homogeneous magnetic field. In the MFM images presented in Fig. 1, bright fields showing the measured phase shifts $\Delta\Phi$ correspond to the regions where the magnetization vectors of the sample and cantilever are oriented in the opposite directions, while dark fields correspond to these vectors oriented in the same direction.

Results and discussion. Figure 1a shows the MFM image of the domain structure of an $Fe_{78}B_{12}Si_9Ni_1$ amorphous alloy ribbon in the initial state. This structure is characterized by domain chaos with a tendency to the formation of a domain structure with a labyrinth morphology in the ribbon plane. It is clearly seen (especially in the three-dimensional diagram) that the magnetization of separate domains is inhomogeneous and decreases toward the boundaries.

1063-7850/04/3005-0383$26.00 © 2004 MAIK "Nauka/Interperiodica"

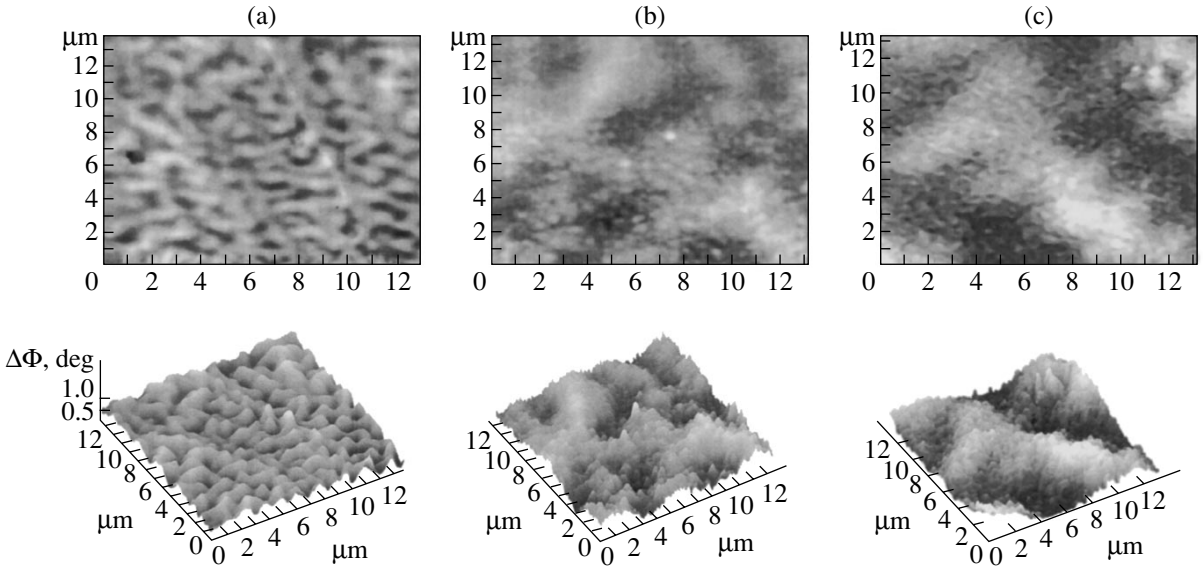

Fig. 1. MFM images of the domain structure of an $Fe_{78}B_{12}Si_9Ni_1$ amorphous alloy ribbon in various states: (a) initial; (b) saturated with hydrogen; (c) annealed.

The introduction of hydrogen changes the domain structure (Fig. 1b) and modifies the Barkhausen effect characteristics: the integral Barkhausen emf over the magnetization reversal cycle increases more than threefold (see [1]); the number of Barkhausen jumps per unit volume increases from 25 to 95; and the range of magnetic fields in which the Barkhausen jumps are observed expands from 60 to 100 A/m. However, it is important to note that the domain structure is studied a rather long period of time after hydrogenation. During this time, hydrogen was completely eliminated from the sample and the Barkhausen effect parameters returned to the initial values characteristic of the nonhydrogenated material (the relaxation time usually does not exceed 20–30 h).

Thus, both the initial state with relatively small dimensions of the domain structure elements and the state upon hydrogenation and subsequent hydrogen elimination from the sample have close integral and spectral characteristics of the Barkhausen noise.

The domain structure of the same alloy ribbon annealed at 360°C (Fig. 1c) differs from the initial structure by much greater domain size and is close in this respect to the structure observed in the sample upon hydrogenation and relaxation. However, the annealed material is characterized by high values of the Barkhausen emf, which are several times greater than those observed in the initial state and in the state upon the introduction and elimination of hydrogen.

The above data indicate that the domain structure of amorphous metal alloys in all cases represents domain chaos with an inhomogeneous distribution of magnetization over each domain volume. The domain boundaries are smeared and oriented chaotically relative to the magnetic field vector (lying in the ribbon plane). The labyrinth structure does not allow some domain walls to move at the expense of other. This domain structure can be considered as static with respect to external magnetic fields within 100–1000 A/m.

It was found that the fractal dimension of the domain structure in the samples studied was influenced neither by the thermal treatment nor by hydrogenation and was always equal to 1.75 ± 0.05. This result indicates that the regions of spontaneous magnetization in the samples occurring in all three states (initial, hydrogenated, and annealed) belong to close morphology types.

The results presented above show that the domain size in disordered structures such as amorphous metal alloys occurring in the state of domain chaos is not correlated with characteristics of the Barkhausen effect. The behavior of Barkhausen noises in such alloys is more likely determined by reorientation of the spontaneous magnetization vectors of separate domains or, as we are prone to believe, of a subdomain magnetic structure of the material. The latter is evidenced by the inhomogeneous character of distribution of the spontaneous magnetization vectors within separate domains.

REFERENCES

1. N. E. Skryabina, L. V. Spivak, A. S. Kinev, *et al.*, Pis'ma Zh. Tekh. Fiz. **26** (21), 26 (2000) [Tech. Phys. Lett. **26**, 947 (2000)].
2. L. V. Spivak and A. S. Kinev, Vestn. Permsk. Univ., Ser. Fiz., No. 6, 9 (2000).
3. N. E. Skryabina, L. V. Spivak, A. S. Kinev, and N. V. Pimenova, Materialovedenie, No. 6, 29 (2001).
4. L. Kong and S. Y. Chou, Appl. Phys. Lett. **70**, 2043 (1997).

Translated by P. Pozdeev

Technical Physics Letters, Vol. 30, No. 5, 2004, pp. 385–388. Translated from Pis'ma v Zhurnal Tekhnicheskoĭ Fiziki, Vol. 30, No. 9, 2004, pp. 73–81.

The Effect of Irradiation on the Characteristics of MOS Transistors

E. N. Bormontov, M. N. Levin, V. R. Gitlin, T. G. Men'shikova, and A. A. Tatarintsev

Voronezh State University, Voronezh, Russia

Received August 12, 2003; in final form, December 22, 2003

Abstract—We have experimentally studied the effect of X-ray radiation on the parameters of MOS transistors. An analysis showed that correct evaluation of the density of surface states and the gate insulator charging by method of subthreshold current-voltage characteristics requires taking into account the planar inhomogeneity of a transistor. Some complication of the method is compensated by the increasing accuracy of determination of the surface parameters and the additional possibility of determining fluctuations of the surface potential. © *2004 MAIK "Nauka/Interperiodica".*

Exposure to ionizing radiation can result in the formation of surface states at the semiconductor–insulator interface and a space charge in the gate insulator (oxide) of a metal–oxide–semiconductor (MOS) transistor [1, 2]. The irradiation can also give rise to significant fluctuations of the surface potential over the semiconductor–insulator interface, which reflects a random distribution of the radiation defects over the insulator surface [2]. The radiation-induced charging leads to a change in the threshold voltage. In addition, the surface states and charge fluctuations lead to a decrease in the slope of the transfer (drain–gate) current–voltage characteristics of MOS transistors in the region of subthreshold currents.

In order to elucidate the mechanisms of radiation-induced instability and solve the problem of predicting the stability of irradiated large-scale MOS integrations, it is necessary to determine the radiation-induced charge, the density of surface states, and the degree of inhomogeneity of the surface potential by independent methods. The theory of MOS transistors with planar inhomogeneity and the methods of determination of the surface characteristics of such transistors were considered in [3].

This Letter presents the results of experimental investigation of the effect of radiation on the surface and fluctuation characteristics of MOS transistors and demonstrates the possibility of independent determination of these parameters.

Experimental and calculation procedures. The samples were *p*-channel transistor structures with a channel length of 5 μm, a gate insulator (SiO_2) thickness of $d = 120$ nm, and a dopant concentration in the substrate of $N_{sub} = 10^{17}$ cm^{-3}. The samples were irradiated with X-ray quanta at $E \approx 25$ keV to a dose of $D \leq 10^6$ rad (Si) in an IRIS-M3 setup. The effect of irradiation on the properties of MOS transistors was studied by measuring subthreshold current–voltage (*I–V*) characteristics on an automated setup.

The effect of the radiation dose on the fluctuation and surface parameters of samples is evaluated within the framework of the model of an inhomogeneous planar MOS transistor. The subthreshold current–voltage characteristics of such transistors with the *p* channel are described by the relation [3]

$$I_D = \frac{Z}{L}\mu_p \frac{n}{m}\left(\frac{kT}{q}\right)^2 \sqrt{\frac{n_i}{N_D}} C_D(\bar{Y}_S) \times \exp\left[-\frac{q}{kT}\frac{V_g - V_g^*}{n}\right]\left[1 - \exp\left(\frac{qV_D}{kT}\frac{m}{n}\right)\right], \quad (1)$$

where Z and L are the channel width and length, respectively; μ_p is the hole mobility in the channel; n_i is the intrinsic carrier density; N_D is the dopant concentration in the substrate; V_g and V_D are the gate and drain voltages, respectively; V_g^* is the gate voltage corresponding to the middle of the region of weak inversion; $\bar{Y}_S = 1.5\ln\lambda$; $\lambda = n_i/N_D$; q is the electron charge; k is the Boltzmann constant; T is the absolute temperature;

$$C_D(\bar{Y}_S) = \frac{1}{\sqrt{2\pi}\sigma}\int_{\bar{Y}_S - 3\sigma}^{\bar{Y}_S + 3\sigma}\left(\frac{q^2\varepsilon_S N_D}{2kT(-Y_S - 1)}\right)^{1/2} \times \exp\left[-\frac{(Y_S - \bar{Y}_S)^2}{2\sigma^2}\right]dY_S \quad (2)$$

is the capacitance of the depleted layer for the average surface potential $\bar{Y}_S$;

$$n = \frac{C_{OX} + C_{SC}^* + qD_{SS}}{C_{OX}}, \quad m = \frac{C_{OX} + C_{SC}^*}{C_{OX}},$$

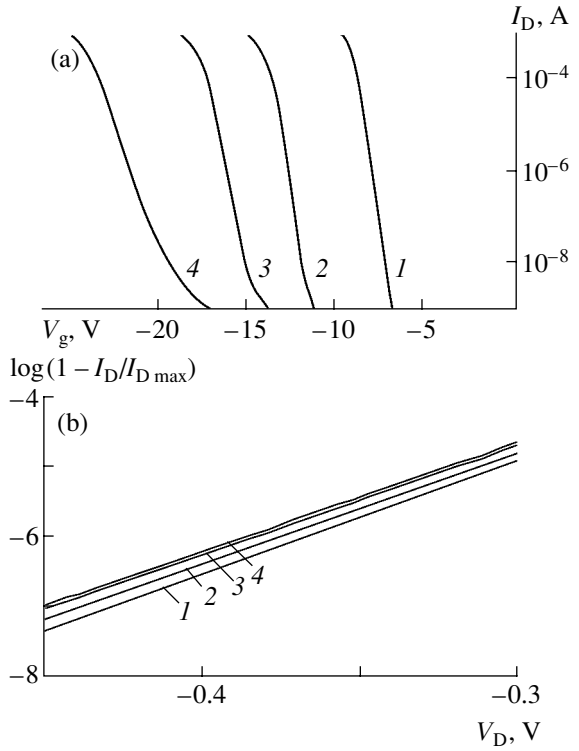

Fig. 1. The transfer (a) and output (b) current–voltage characteristics of a *p*-channel MOS transistor (*1*) before irradiation and (*2–4*) after X-ray irradiation to a dose of $D = 10^4$, 10^5, and 10^6 rad, respectively.

C_{OX} is the capacitance of the gate insulator; D_{SS} is the spectral density of the surface states;

$$C^*_{SC} = \frac{\varepsilon_S}{\sqrt{2}L_D}\frac{1}{\sqrt{2\pi}\sigma}\int_{1.5\ln\lambda-3\sigma}^{1.5\ln\lambda+3\sigma} \times\left|\frac{\exp(Y_S)-1-\lambda^2(\exp(-Y_S)-1)}{\sqrt{\exp(Y_S)-Y_S-1+\lambda^2(\exp(-Y_S)+Y_S-1)}}\right| \times\exp\left[-\frac{(Y_S-1.5\ln\lambda)^2}{2\sigma^2}\right]dY_S \quad (3)$$

is the total capacitance of the space charge region in the semiconductor for $Y_S = 1.5\ln\lambda$; and σ is the fluctuation parameter.

The form of relation (1) is similar to that of an analogous expression for a homogeneous planar transistor [4], but the parameters entering into these formulas are substantially different. In particular, the parameters *m* and *n* in (1) depend on the total capacitance C_{SC} of the space charge region (including the contribution from an inversion layer) rather than on the capacitance C_D of the depleted layer. In addition, the adopted model [3] takes into account the planar inhomogeneity of an MOS transistor, whereby all capacitances in (1) are averaged with respect to the surface potential.

The method of determination of the surface parameters of MOS transistors is essentially as follows. By measuring the slope of the rectified input characteristic (equal to m/n in the $\ln(1 - I_D/I_{D\,max})$ versus qV_D/kT coordinates) and the transfer characteristic ($1/n$ in the $\ln I_D$ versus qV_g/kT coordinates), we determine the *m* value. Then, using the definition of *m*, we determine the experimental capacitance of a space charge region in the semiconductor corresponding to the middle of the region of weak inversion, $C^*_{SC} = (m - 1)C_{OX}$. For a given dopant concentration in the substrate N_D, C^*_{SC} depends only on the fluctuation parameter σ. Using the theoretical dependence of C^*_{SC} on σ described by relation (3) and the experimental C^*_{SC} value, we can determine the fluctuation parameter. Using the *m* and *n* values, we can also calculate the spectral density of states by the formula

$$D_{SS} = \frac{C_{OX}+C^*_{SC}}{q}\left(\frac{n}{m}-1\right) = \frac{C_{OX}+(m-1)C_{OX}}{q} \times\left(\frac{1}{\tan\alpha_D}-1\right) = \frac{\tan\alpha_D}{|\tan\alpha_g|}\frac{C_{OX}}{q}\left(\frac{1}{\tan\alpha_D}-1\right). \quad (4)$$

Finally, upon additionally determining the threshold voltage V_T of the MOS transistor (e.g., by extrapolating the $I_D^{1/2}(V_g)$ curve to the region of strong inversion until intersection with the V_g axis) and using the known D_{SS} and σ values, we can calculate the charge Q_{0t} in the oxide as

$$Q_{0t} = -Q^*_{SC} - C_{OX}\left(V_T - \phi_{ms} - 2\frac{kT}{q}\ln\lambda\right) + 2qD_{SS}\frac{kT}{q}\ln\lambda, \quad (5)$$

where

$$Q^*_{SC} = \frac{\sqrt{2}qN_DL_D}{\sqrt{2\pi}\sigma}\int_{1.5\ln\lambda-3\sigma}^{1.5\ln\lambda+3\sigma}[(\exp Y - Y - 1) + \lambda^2(\exp(-Y)+Y-1)]^{1/2}\exp\left[-\frac{(Y-1.5\ln\lambda)^2}{2\sigma^2}\right]dY$$

is the total space charge of the semiconductor in the middle of the region of weak inversion.

Results and discussion. Figure 1 presents the typical experimental current–voltage characteristics measured in the region of subthreshold currents. Figure 2a shows an experimental plot of the threshold voltage

versus radiation dose. As can be seen from these data, the exposure modifies both the transfer (I_D versus V_g) and the output (I_D versus V_D) characteristics, as well as the threshold voltage of the transistor. It should be emphasized that the characteristics of both types should be considered simultaneously. Separate analysis of each family may lead to ambiguous interpretation of the results of investigation of the effect of irradiation on the surface properties of the base transistor structure.

Figure 2 also shows the dose dependences of the radiation-induced charge Q_{0t} accumulated in the oxide (Fig. 2a, curve *2*), the density of surface states D_{SS} (Fig. 2b, curve *1*), and the fluctuation parameter σ (Fig. 2b, curve *2*) of the Si–SiO_2 structure calculated using relations (3)–(5) and the experimental data. For comparison, Fig. 2b also presents the dose dependence of the density of surface states calculated with neglect of the surface potential fluctuations in silicon (Fig. 2b, curve *1*'). The main result illustrated by these data is that exposure to X-rays leads to the accumulation of radiation-induced charge in the oxide, which is accompanied by a significant growth of fluctuations of the semiconductor surface potential without the generation of additional surface states. It should also be noted that inhomogeneities in the semiconductor surface potential (reflected by the parameter σ) are correlated with the radiation-induced charge Q_{0t} in the oxide.

A decrease in the slope of the drain–gate current–voltage characteristics upon irradiation is conventionally related to an increase in the density of surface states [5, 6]. However, both the growth of the density of surface states with the radiation dose (Fig. 2b, curve *1*) and the typical U-shaped energy distribution for a low density of surface states can represent computational artifacts related to charge fluctuations in the oxide layer. In other words, neglect of the fluctuations may lead to the incorrect conclusion that the density of surface states increases irrespective of the type of radiation. On the other hand, the manifestation of radiation effects substantially depends on the character of the radiation action [1, 7]. Thus, radiation of some other type or a combination of X-ray radiation with other factors (annealing, UV radiation, etc.) may lead, for example, to a growth in the density of surface states or to the simultaneous increase in the density of surface states and the degree of inhomogeneity of the surface potential (surface charge fluctuations).

It was of interest to estimate the probability of the appearance of the observable values of the fluctuation parameter σ according to the existing models [8, 9]. For this purpose, we used the simplest Goetzberger capacitor model [8]. This model underlies the theory of inhomogeneous planar MOS transistors and is widely used for the interpretation of dispersion of the time of recharge of the surface states in MOS structures featuring large-scale technological fluctuations. Such fluctuations have been observed in the experiments with a scanning mercury probe [10].

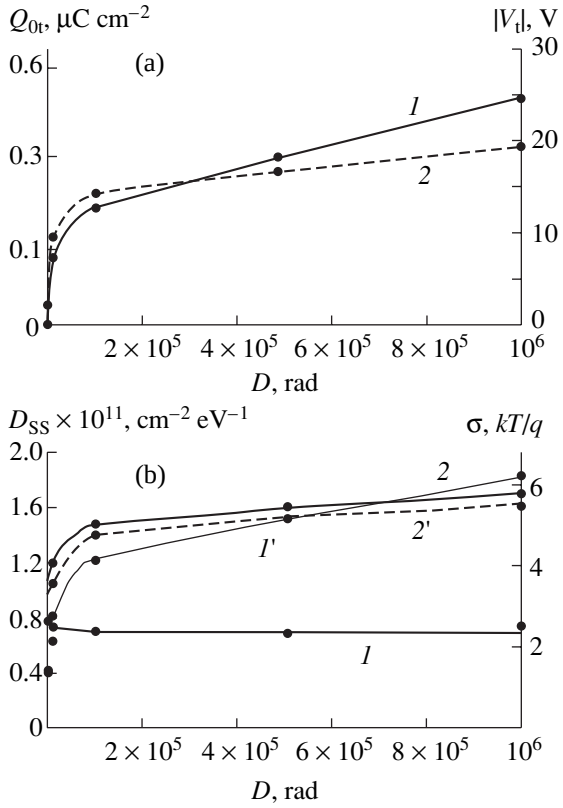

Fig. 2. Dose dependences of the surface parameters of X-ray irradiated MOS transistors: (a) the threshold voltage V_T (*1*) and the built-in charge Q_{0t} (*2*); (b) the density of surface states D_{SS} calculated using the models [3] (*1*) and [4] (*1*') and the fluctuation parameter σ calculated using the model [3] (*2*) and the Goetzberger capacitor model [8] (*2*').

According to the Goetzberger capacitor model, an MOS structure is conditionally subdivided into a large number of microscopic elements (parallel connected microcapacitors) randomly distributed over the entire area of the structure studied. Inside each element, the characteristics (capacitance, charge, potential) are considered homogeneous. The linear size of the element should be greater than the depth of the space charge region. In the regime of depletion of the MOS structure, the area of the element is equal to the squared depth of the depleted layer.

It was demonstrated [10] that a dominating role in fluctuations of the total surface charge in silicon based MOS structures belongs to the fluctuations of the charge Q_{0t} built in the oxide. It is commonly accepted that Q_{0t} and its fluctuations are the main factors responsible for the surface potential fluctuations in such structures. Therefore, the fluctuations in the semiconductor surface potential can be estimated by the value of accumulated built-in charge, that is, by the number of radiation defects in the oxide layer of an MOS structure.

Let $\bar{N}$ be the average number of defects per element area A (i.e., the area of a microcapacitor) in the gate insulator. If $\bar{N}$ is large, the distribution function $P(N)$ will represent the Gauss approximation of the Poisson distribution

$$P(N) = \frac{1}{\sqrt{2\pi\bar{N}}}\exp\left(-\frac{(N-\bar{N})^2}{2\bar{N}}\right). \quad (6)$$

The number of defects per element area and the density of a built-in charge Q_{0t} are obviously related as $N = AQ_{0t}/q$. Using the relation between probabilities, $P(N)dN = P(Q_{0t})/dQ_{0t}$, we obtain the following expression for the distribution of the built-in charge:

$$P(N) = \left(\frac{A}{2\pi q\bar{Q}_{0t}}\right)^{1/2}\exp\left(-\frac{A(Q_{0t}-\bar{Q}_{0t})^2}{2q\bar{Q}_{0t}}\right). \quad (7)$$

By the same token, using the dependence of the rms charge fluctuation on the MOS structure parameters, the distribution of the dimensionless surface potential can be expressed as

$$P(Y_S) = \frac{1}{\sigma\sqrt{2\pi}}\exp\left(-\frac{(Y_S-\bar{Y}_S)^2}{2\sigma^2}\right), \quad (8)$$

where σ is the standard deviation of the dimensionless surface potential given by the formula

$$\sigma = \frac{\beta}{C_{0X}+C_{SC}^*+C_{SS}}\left(\frac{q\bar{Q}_{0t}}{A}\right)^{1/2} \quad (\beta = q/kT). \quad (9)$$

The results of calculation of the dose dependence of the fluctuation parameter σ calculated within the framework of the Goetzberger model (Fig. 2b, curve *2*') show a good agreement with the experimental data (Fig. 2b, curve *2*). This coincidence confirms the model [8] and, on the other hand, justifies the use of the theory of inhomogeneous planar MOS transistors [3] and the method for of calculation of the MOS structure parameters based on this theory.

Thus, for large-scale fluctuations of the surface potential in an MOS structure with the characteristic size of the element exceeding the width of the space charge region in the semiconductor, the surface potential Y_S is distributed according to Gauss law (8) with standard deviation (9). In this case, correct evaluation of the density of surface states and the dielectric charging by method of subthreshold current-voltage characteristics requires taking into account the planar inhomogeneity of the MOS transistor. Some complication of the method is compensated by a significant increase in the accuracy of determination of the surface parameters and the additional possibility of determining fluctuations of the surface potential.

REFERENCES

1. V. S. Pershenkov, V. D. Popov, and A. V. Shal'nov, *Surface Radiation Effects in Integral Circuits* (Énergoatomizdat, Moscow, 1988).
2. *Ionizing Radiation Effects in MOS Devices and Circuits*, Ed. by T. P. Ma and P. V. Dressendorfer (Wiley, New York, 1989).
3. E. N. Bormontov, M. N. Levin, S. N. Borisov, and S. A. Vyalykh, Zh. Tekh. Fiz. **71** (2), 61 (2001) [Tech. Phys. **46**, 192 (2001)].
4. R. J. van Overstraten, G. J. Declerck, and P. A. Muls, IEEE Trans. Electron Devices **22**, 282 (1975).
5. P. J. McWhorter and P. S. Winokur, Appl. Phys. Lett. **48**, 133 (1986).
6. D. M. Fleedwood, M. R. Shaheyfelt, J. R. Schwank, *et al.*, IEEE Trans. Nucl. Sci. **36**, 1816 (1989).
7. M. N. Levin, E. N. Bormontov, O. V. Volkov, *et al.*, Mikroélektronika **30**, 16 (2001).
8. E. N. Nicollian and A. Goetzberger, Bell Syst. Tech. J. **46**, 1055 (1967).
9. J. R. Brews, J. Appl. Phys. **43**, 3451 (1974).
10. R. S. Nakhmanson and S. B. Sevastianov, Solid State Electron. **27**, 881 (1984).

Translated by P. Pozdeev

Technical Physics Letters, Vol. 30, No. 5, 2004, pp. 389–391. Translated from Pis'ma v Zhurnal Tekhnicheskoĭ Fiziki, Vol. 30, No. 9, 2004, pp. 82–87.

Differential Low-Coherence Interferometry for *In Situ* Diagnostics of Transparent Structures

V. V. Ivanov*, V. A. Markelov, M. A. Novikov, and S. S. Ustavshchikov

Institute for Physics of Microstructures, Russian Academy of Sciences, Nizhni Novgorod, Russia

** e-mail: ivanov@ipm.sci-nnov.ru*

Received October 15, 2003

Abstract—We describe and demonstrate a new differential method capable of measuring the profiles of transparent structures. Based on fiber-optic low-coherence interferometry and possessing a high noise immunity, the proposed technique can be used for the noncontact *in situ* diagnostics of microstructures under extremal conditions. © *2004 MAIK "Nauka/Interperiodica".*

Optical interference methods are widely used for the diagnostics of both microscopic and macroscopic structures. This is related to the noncontact and nondestructive character of the interference measurements in combination with their high accuracy. In some cases, such as control of the surface deviations from a preset shape, measurement of the step height in stepped structures, monitoring of etching and microprocessing of optical materials, and diagnostics of inhomogeneities in the refractive index, temperature gradient, etc., the object can be probed in the differential mode, whereby the difference of heights or thicknesses in two regions is measured [1–3]. For the diagnostics of stepped structures and in some other applications, of special interest is the differential optical low-coherence reflectometry (OLCR) capable of correctly measuring height (thickness) differences greater than $\lambda/2$ [1, 2].

This Letter describes a new OLCR technique optimized for *in situ* diagnostics of transparent structures.

The proposed method is essentially a modification of optical low-coherence common-path interferometry. One possible variant of the implementation of OLCR is illustrated in Fig. 1. According to this, the linearly polarized light from a low-coherence source *LCS* passes through a tunable interferometer *I* and is transmitted via an optical fiber *F* to polarization beam splitter PBS_1, where the incident light is separated into two parallel probing beams with mutually orthogonal linear polarizations. Being reflected from the front and rear surfaces of a sample *S*, these beams are recombined in splitter PBS_1 and transmitted via fiber *F* to a semitransparent mirror *BS* and the second polarization beam splitter PBS_2 (Wollaston prism), after which the separated beams reach photodetectors PD_1 and PD_2. The polarization effects in fiber *F* can be compensated by using a polarization controller or a 45° Faraday phase rotator placed in front of the first polarization beam splitter PBS_1.

When the interferometer *I* is scanned, the photocurrents $J_{1,2}$ measured at the outputs of photodetectors PD_1 and PD_2 vary as described by the following relations (Fig. 2) [4]:

$$J_{1,2}(x) = \bar{J}_{1,2} + j^{(0)}_{1,2}(x) + j_{1,2}(x) + j_{1,2}(-x),$$

$$j^{(0)}_{1,2}(x) = A^{(0)}_{1,2}\Gamma(x)\cos[4\pi x/\lambda_S], \qquad (1)$$

$$j_{1,2}(x) = a_{1,2}\Gamma(n^{\mathrm{gr}}_{1,2}d_{1,2} - x)\cos[4\pi(n_{1,2}d_{1,2} - x)/\lambda_S].$$

Here, x is the difference of the optical path lengths of the tunable interferometer, $\bar{J}_{1,2}$ is the x-independent part of the photocurrent, $A^{(0)}_{1,2}$ and $a_{1,2}$ are the interference signal amplitudes, $\Gamma(x)$ is the envelope of the coherence function of light at the photodetectors, λ_S is the central wavelength of the *LCS* radiation, $n_{1,2}$ and $d_{1,2}$ are the refractive indices and geometric thicknesses of the sample at the two points of measurement, and

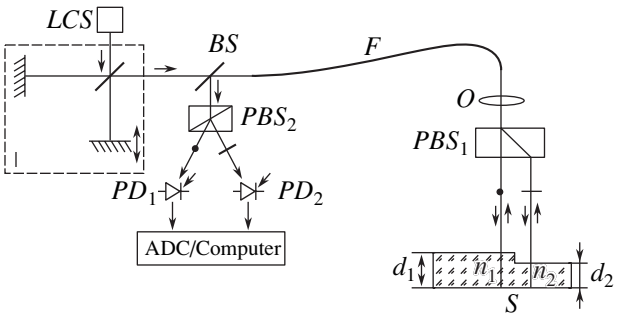

Fig. 1. Schematic diagram of the differential optical low-coherence reflectometer: (*LCS*) low-coherence light source; (*I*) tunable interferometer; (*BS*) semitransparent beam splitter; (PBS_1, PBS_2) polarization beam splitters; (*O*) objective lens; (*S*) sample; (PD_1, PD_2) photodetectors; (ADC) analog-to-digital converter.

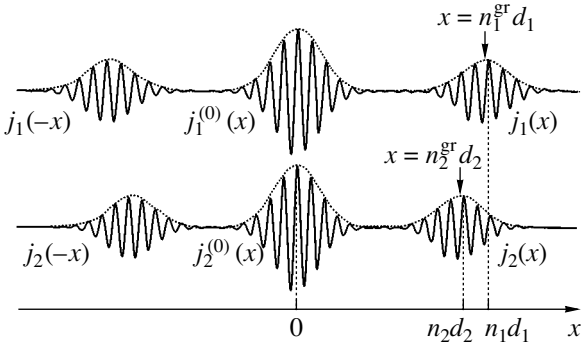

Fig. 2. Interference signals in the differential optical low-coherence reflectometer (dotted curves show the signal envelopes).

$n_{1,2}^{gr} = n_{1,2} - \lambda_S (dn_{1,2}/d\lambda)_{\lambda_S}$ are the group refractive indices of the sample.

If the measured differential optical thickness $n_1^{gr} d_1 - n_2^{gr} d_2$ is smaller than or comparable to the light coherence length (10–20 μm), that is, if the interference signals $j_1(x)$ and $j_2(x)$ overlap, the measurement of the optical thickness difference is reduced to determining the position of the central interference maximum of the $j_1(x)$ signal in the "coordinate system" set by the interference maxima of the $j_2(x)$ signal (Fig. 2). This circumstance makes it unnecessary to measure the arm length difference x in the tunable interferometer and provides for a weak dependence of the results on the character of modulation $x(t)$, which simplifies the procedure and reduces the cost of the system, especially in the case of high-precision measurements. For determining the difference of the optical thicknesses, it is sufficient to modulate the differential interferometer arm length within several coherence lengths of the radiation employed.

The interference signals $J_1(x)$ and $J_2(x)$ are independent of the optical path length between the tunable interferometer and the sample [5]. For this reason, the proposed method is insensitive to changes in the optical length of fiber F, uncorrelated fluctuations of the optical path lengths of the probing beams between the sample and polarization beam splitter PBS_1, and the sample translations along the probing beams.

The error of measurements of the differential optical thickness can be expressed as

$$\delta h = \delta z + M(\lambda_S/2), \tag{2}$$

where $\delta z < \lambda_S/2$ is the error of determining the position of the central interference maximum of the $j_1(x)$ signal in the coordinate system set by the interference maxima of the $j_2(x)$ signal; $M(\lambda_S/2)$ is the error related to incorrect recognition of the central maximum of the interference signals $j_1(x)$ and $j_2(x)$ (M is an integer). If error (2) is related only to the additive radiation noise, it can be shown that

$$\delta z = C_\varphi (\lambda_S/4\pi)\sqrt{(\sigma_1/a_1)^2 + (\sigma_2/a_2)^2}, \quad \sigma_1/a_1, \sigma_2/a_2 \ll 1, \tag{3}$$

where $\sigma_{1,2}$ is the standard noise in the corresponding channel and $C_\varphi \approx 1$ is the coefficient determined by a particular algorithm used for the treatment of interference signals (1). The probability of making an error amounting to several (integer) half-waves can be estimated as the rms error of measuring the shift of maxima in the envelope of the interference pattern (1):

$$\delta D_{env} \approx C_D l_{coh}\sqrt{(\sigma_1/a_1)^2 + (\sigma_2/a_2)^2}, \quad \sigma_1/a_1, \sigma_2/a_2 \ll 1. \tag{4}$$

Here, $C_D \approx 1$ is the coefficient depending on the method used for determining a maximum of the signal envelope and l_{coh} is the coherence length of the light source.

We may expect that the probability of making a $\lambda_S/2$ error in determining the differential optical thickness is small when $\delta D_{env} \ll \lambda_S/2$. Let $\sigma_{1,2}$ be determined by the shot and excess noise of the light source and the system involve a matched filter (i.e., a filter with the transmission function identical to the spectrum of signal (1)). Then, for an average power of $\bar{P}_{1,2} = 30$ μW incident onto the photodetectors, a visibility of the interference signals equal to $a_{1,2}/\bar{J}_{1,2} = 1/2$ (theoretical maximum for a common-path interferometer), a photodetector responsivity of 0.35 A/W, a modulation rate of the interferometer arm length equal to 50 mm/s (the maximum possible value), and a source with $\lambda_S = 800$ nm and $l_{coh} = 8$ μm, we obtain $\delta z \approx 3 \times 10^{-3}$ nm and $\delta D_{env} \approx 4 \times 10^{-4}$ μm, which corresponds to 1/1000 of the interference band width. Thus, the probability of a $\pm\lambda/2$ error in this situation is very small.

We have experimentally verified the proposed method by measuring the profile of a glass substrate of a spherical mirror with a curvature radius of 5 m. The experimental setup corresponded to the scheme of Fig. 1. The light source was a superluminescent diode with $\lambda_S = 820$ nm, $l_{coh} = 8$ μm, and an output power of 100 μW. The interferometer arm difference was modulated by reciprocating motions of a mirror glued to a loudspeaker membrane. No special measures were taken for vibration isolation of the interferometer, the measuring head, and the sample. The interferometer was connected to the measuring head via a 5-m-long single-mode optical fiber. The polarization state of light at the input of the polarization beam splitter PBS_1 was controlled by a polarization manager. The Wollaston prism PBS_1 was a single crystal calcite plate cut at 45° relative to the optical axis. The distance between separated beams was 570 μm; the beam diameter on the sample surface did not exceed 50 μm. The interference

signals from photodetectors were amplified, digitized, and processed on a personal computer.

The rms error upon averaging over 10 measurements was about 2 nm. This error was determined by artifacts of the algorithm used for the interference signal processing. The proposed method has proved to be insensitive (to within the measurement error) with respect to sample translations (within 100 μm) along the optical axis of the system. It was also low-sensitive with respect to the character of modulation of the optical path length in the tunable interferometer, as well as to the acoustic noise and vibrations acting on the interferometer: the phase noise in the interferometer was three orders of magnitude greater than the measurement accuracy. Thus, even the simplest demonstration experiment allowed a nanometer-scale longitudinal resolution to be reached in the measurement of a test object profile and showed the high noise immunity of the proposed method.

REFERENCES

1. D. P. Dave and Th. E. Milner, Opt. Lett. **25**, 227 (2000).
2. D. P. Dave and Th. E. Milner, Appl. Opt. **41**, 2038 (2002).
3. Zh.-F. Zhou, T. Zhang, and W.-D. Zhou, Appl. Opt. **41**, 125 (2002).
4. Y. J. Rao and D. Jackson, Meas. Sci. Technol. **7**, 981 (1996).
5. V. V. Ivanov, M. A. Novikov, *et al.*, Proc. SPIE **4900**, 548 (2002).

Translated by P. Pozdeev

Technical Physics Letters, Vol. 30, No. 5, 2004, pp. 392–395. Translated from Pis'ma v Zhurnal Tekhnicheskoĭ Fiziki, Vol. 30, No. 9, 2004, pp. 88–95.

Infrared Quenching of Electroluminescence in ZnS:Mn Thin-Film Emitters

N. T. Gurin and D. V. Ryabov

Ul'yanovsk State University, Ul'yanovsk, Russia

e-mail: Nsg@sv.uven.ru

Received October 29, 2003

Abstract—IR irradiation of electroluminescent emitters based on thin ZnS:Mn films in the pause between excitation voltage pulses produces quenching of the luminescence and leads to a decrease in the emission intensity within the wavelength interval 530–540 nm and an increase within 640–680 nm. These phenomena are explained by the IR-radiation-induced recharge of the deep centers related to the sulfur vacancies V_S^{2+} and V_S^+, whereby the concentration of the latter centers increases, and redistribution of the channels of impact excitation of Mn^{2+} and V_S^+ centers in favor of the latter type. © *2004 MAIK "Nauka/Interperiodica".*

Introduction. Well-known data [1] on the influence of IR radiation on the electroluminescence (EL) of powdered zinc sulfide phosphors with recombination luminescence showed evidence of the presence of an absorption band in the IR spectral range. Pulsed irradiation of the samples in this spectral interval led to a decrease in the luminance wave amplitude, that is, produced quenching of the luminescence.

In electroluminescent thin-film (ELTF) emitters exhibiting intracenter luminescence, pulsed IR irradiation in the pause between excitation voltage pulses leads to an increase in the amplitude of a current passing through the phosphor layer during these pulses [2, 3]. The influence of such IR irradiation on the EL spectra was not studied. The EL spectra of alternating-current ELTF emitters based on ZnS:Mn were measured in the continuous excitation mode. Using such spectra, typically showing only the average ELTF emitter brightness [4], it is not possible to reveal the influence of the current kinetics in the phosphor layer and of the instantaneous brightness variations.

In this context, we have studied variations of the EL spectra of ELTF emitters subject to pulsed IR irradiation in the pause between excitation voltage pulses. The spectra were measured in various regions of the luminance wave corresponding to different excitation levels. The measurements were performed under the conditions when adjacent brightness waves did not overlap and the pause between excitation voltage pulses was sufficiently long for the neutralization of space charges formed in the phosphor layer.

Experimental. The experiments were performed on ELTF emitters with an MISIM-type layer structure, where M denotes the lower transparent 0.2-μm-thick SnO_2 based electrode deposited onto a glass substrate and the upper nontransparent thin-film Al electrode with a thickness of 0.15 μm and a diameter of 1.5 mm; S is the 0.48-μm-thick electroluminescent ZnS:Mn (0.5 wt %) layer; and I are the insulating ZrO_2–Y_2O_3 (13 wt %) layers. The ZnS:Mn phosphor layer was obtained by thermal evaporation in a quasi-closed volume in vacuum and deposition onto a substrate heated to 250°C, followed by annealing for 1 h at 250°C. The upper nontransparent metal electrode was also obtained by thermal deposition in vacuum, while thin insulating layers were prepared using the electron-beam deposition technique.

We have experimentally studied the luminance wave, representing the time variation of the instantaneous luminance L_λ at a given wavelength, using ELTF emitters excited with alternating-sign voltage pulses of a triangular shape. The measurements were performed either with continuous excitation or in a pulse train mode, whereby the excitation signal $V(t)$ represented pairs of triangular pulses with a frequency of 20 Hz. In the first half-period, either positive or negative excitation half-waves can be applied to the upper electrode, which will be referred to as the +Al and –Al regime, respectively. The time interval T_s between excitation pulse trains was T_s = 1, 50, or 100 s. The output radiation corresponding to the first luminance wave was transmitted through an MUM-2 monochromator (wavelength uncertainty, 0.5 nm; linear dispersion, 4.8 nm/mm; slit width, 3 mm) in order to increase the sensitivity of detection and measured with an FEU-79 photoelectron multiplier. The measurements were performed in a wavelength range from 400 to 750 nm at a 5-nm step.

The patterns of excitation voltage $V(t)$ and luminance waves $L_\lambda(t)$ were recorded with the aid of a two-

1063-7850/04/3005-0392$26.00 © 2004 MAIK "Nauka/Interperiodica"

channel storage oscillograph of the S9-16 type linked via an interface to a personal computer. The system ensured the measurement and storage of 2048 experimental points at a preset discretization period in each channel and 256 levels of the amplitude quantization. The data were mathematically processed and graphically displayed using the application program packages MAPLE V (Release 4, Version 4.00b) and GRAPHER (Version 1.06, 2-D Graphing System).

The total EL spectrum $L(\lambda)$ was obtained by summing the partial spectra $L_n(\lambda)$ measured in separate regions (n = I–IV) of the luminance wave as described elsewhere [4]. Here, region I of the luminance wave corresponds to the "fast" initial buildup of the current $I_p(t)$ through the phosphor layer, regions II and III correspond to the "slow" portion of the $I_p(t)$ growth, and region IV corresponds to the decay portions of both $I_p(t)$ and $L(\lambda)$.

The ELTF emitter structures were photoexcited from the substrate side using either continuous or pulsed IR radiation of a pair of LEDs of the AL107B type with an emission band maximum at $\lambda = 950$ nm, a full width at half-maximum of $\Delta\lambda_{0.5} = 25$ nm, a total power of $P \sim 12$ mW, and a total photon flux density of $\Phi \sim 3 \times 10^{15}$ mm^{-2} s^{-1}. The emission spectra presented below were obtained by statistical processing of the results of five measurements.

Results. The main experimental results can be summarized as follows. In the continuous excitation mode, no influence of the IR irradiation on the EL spectrum was observed to within the experimental error. Nor was any change in the EL spectra observed in the pulse train excitation mode, when the IR irradiation was produced during the action of excitation voltage pulses.

When the samples were subjected to IR irradiation during a pause between excitation voltage pulses in the pulse train mode, various changes were observed in the EL spectra measured for regions I–IV of the luminance wave and in the total EL spectra of ELTF emitters during the first half-period of the excitation voltage pulse applied in different regimes (±Al) after the pause. These changes are as follows:

(i) The intensity of the main peak (~585 nm) decreases by a factor of 1.1–2.55 in the EL spectra measured for regions I–III and in the total spectrum in the –Al regime (see Figs. 1a and 1e), as well as in the spectra for all regions I–IV and in the total spectrum in the +Al regime (Figs. 1c, 1d, and 1f).

(ii) The main peak increases by a factor of ~1.7 in the EL spectrum measured for region IV in the –Al regime (Fig. 1b).

(iii) The relative intensity of emission in the wavelength interval ~(530–540) nm decreases, and that in the interval ~(640–690) nm increases, in the EL spectra measured for regions I and IV in the –Al regime (Figs. 1a and 1b).

(iv) The relative intensity of emission in the interval ~(530–540) nm decreases in the EL spectrum measured for region I in the +Al regime (Fig. 1c).

(v) The relative intensity of the band peaked at ~495 nm decreases in the EL spectra measured for region I–IV and in the total spectrum in the –Al regime (Figs 1a, 1b, and 1e).

All these changes become more pronounced on increasing the pause (during which IR irradiation is performed) between excitation voltage pulses.

Discussion of results. The above results can be given the following interpretation. When the applied voltage exceeds the threshold of the ELTF emitter operation, electrons are injected by means of the tunneling emission from the surface states in a near-cathode region of the insulator–phosphor interface. Ballistically accelerated in the interelectrode region, electrons produce impact ionization of Mn^{2+} centers and the deep centers related to zinc vacancies (V_{Zn}) and sulfur vacancies (V_S) in the near-anode region of the phosphor with the formation of a positive space charge. In the near-cathode region, free electrons trapped on the deep centers related to V_S^{2+} and V_S^+ (with the energies ≈1.3 and ≤1.9 eV above the valence band top, respectively) neutralize the positive space charge formed in the preceding ELTF emitter operation cycle and give rise to a negative space charge. In the pause between two sequential operation cycles, both space charges are neutralized to a degree increasing with the pause duration [2, 3].

Irradiation of the ELTF emitter with photons of certain energy in the IR spectral range during a pause between two voltage pulses results in the production of additional V_S^+ centers as a result of the trapping of electrons (injected from the valence band) on the V_S^{2+} centers. This leads to a decrease in the positive space charge, the field strength in the near-cathode region, and the tunneling emission current during the next operation cycle in the –Al regime, in which case the concentration of sulfur vacancies at the upper phosphor–insulator interface exceeds that of the zinc vacancies and determines the positive space charge. As the applied field strength increases, the current amplitude grows due to ionization of the V_S^+ centers additionally formed in the phosphor [2, 3]. According to [4–7], the EL spectrum of ELTF emitters is determined by the intracenter emission from Mn^{2+} ions giving rise to the bands peaked at λ_m = 557, 578, 600, 616, and 635–637 nm. This scatter reflects various positions of these ions in a real crystal lattice of ZnS and the possible formation of an α-MnS phase (λ_m = 635 nm [6, 7]). The spectrum may also contain a band at λ_m = 606–610 nm related to the complex centers formed by Mn^{2+} ions and sulfur vacancies [8–10].

The emission observed in the wavelength interval ~(530–540) nm in the absence of IR irradiation in the

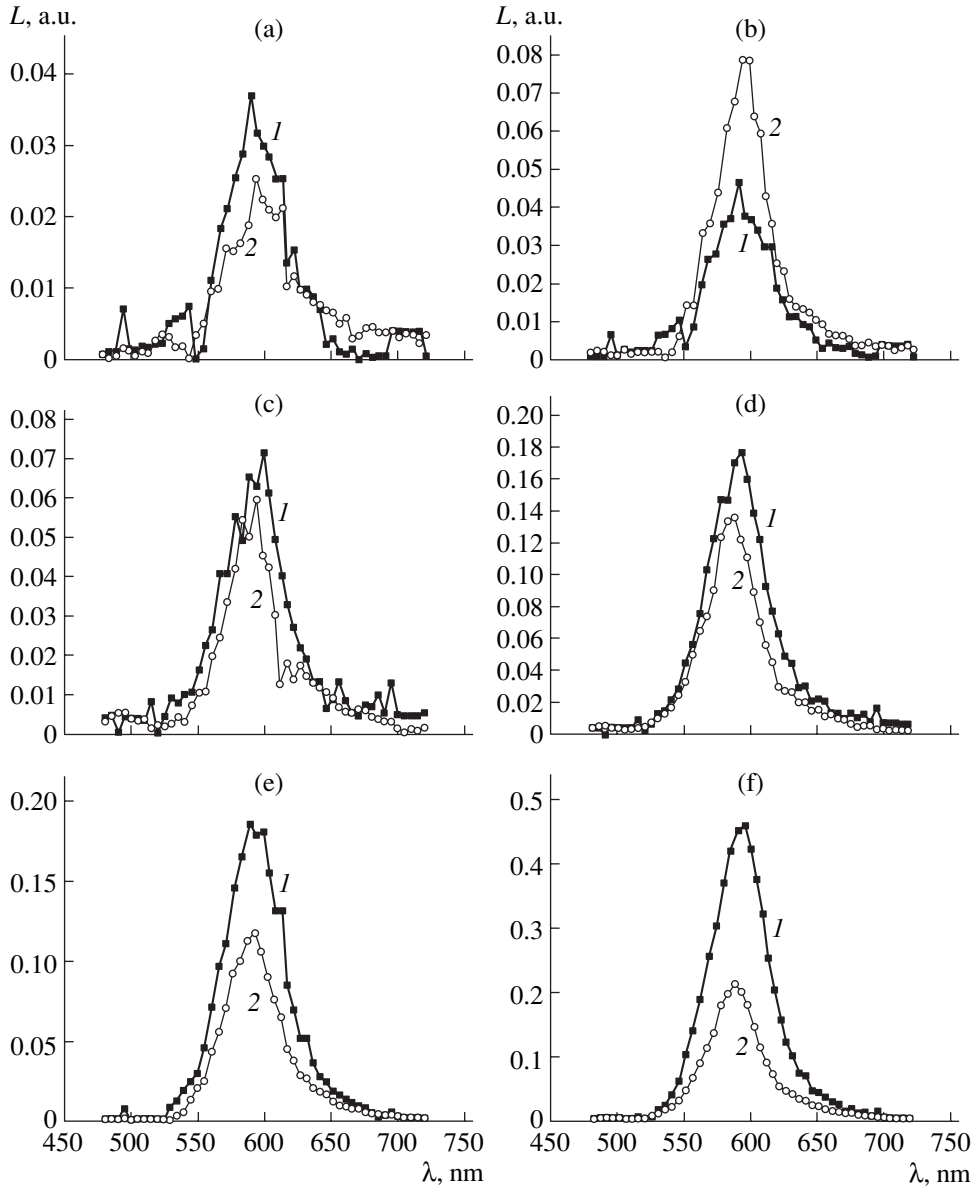

Fig. 1. The EL spectra of ZnS:Mn based emitters measured (*1*) without and (*2*) with IR irradiation in the pause between excitation voltage pulses in (a, b, e) the –Al regime and (c, d, f) the +Al regime: (a, c) region I of the luminance wave; (b, d) region IV of the luminance wave; (e, f) total spectrum. T_s = 100 s.

pause (Figs. 1a–1c and 1e) can be due to a recombination radiation accompanying the trapping of free electrons on deep centers representing doubly charged sulfur vacancies (V_S^{2+}) situated ~1.3 eV above the valence band top [4, 8, 11]. The fact that this emission is more strongly manifested in the –Al regime is related to peculiarities of the ZnS:Mn film technology, whereby a part of the layer adjacent to the upper Al electrode is depleted of sulfur. As a result, a greater number of V_S^{2+} vacancies may appear in this region than in the lower part under equilibrium conditions [2, 3]. A decrease in the relative intensity of emission in this spectral interval observed for regions I and IV of the luminance wave in the EL spectra measured in the –Al regime (Figs. 1a and 1b) upon the IR irradiation is explained by a decrease in the concentration of V_S^{2+} centers as a result of trapping electrons injected from the valence band, with the corresponding increase in the concentration of singly charged V_S^+ centers. This gives rise to the intensity of recombination emission at 640–690 nm observed for regions I and IV in the EL spectra measured in the –Al regime (Figs. 1a and 1b), which is related to the electron transitions from the conduction band or from relatively shallow donor levels to a level formed by V_S^+ with an energy of ≥1.9 eV below the conduction band bottom.

The emission band at $\lambda_m \approx 495$ nm (Figs. 1a, 1b, and 1e) is probably due to the recombination emission from donor–acceptor pairs related to the doubly charged V_S^{2+} vacancies. The quenching of this luminescence band observed in all EL spectra measured in the –Al regime after the IR irradiation can be explained by the aforementioned distribution of structural defects across the phosphor layer, whereby the upper part of this layer is enriched with defects of the sulfur vacancy type. The IR irradiation leads to a decrease in concentration of V_S^{2+} centers and, hence, of the donor–acceptor pairs.

Variations of the aforementioned emission bands are much less manifested in the EL spectra measured for regions II and III and in the total spectra (Figs. 1e and 1f), which is explained by a significant increase in intensity of the main luminescence band related to the intracenter emission from Mn^{2+} ions.

The IR quenching of the main EL peak intensity is probably explained by redistribution of the channels of impact excitation of Mn^{2+} centers and the deep centers related to the sulfur (V_S^+) and zinc (V_{Zn}^{2-}) vacancies. Indeed, according to [3], an increase in the concentration of V_S^+ centers due to the IR irradiation reaches $\sim 1.5 \times 10^{16}$ cm^3 for an equilibrium concentration of these vacancies amounting to $(3–4) \times 10^{16}$ cm^3. This leads to redistribution of the impact excitation events between V_S^+ and Mn^{2+} centers by a factor of 1.37–1.5 in favor of the former type, even without allowance of the lower ionization threshold of the V_S^+ centers (~1.9 eV) as compared to the Mn^{2+} centers (~2.4–2.5 eV) and, probably, of the greater impact excitation cross section of the former centers. An increase in the relative intensity of the main EL peak observed for region IV in the –Al regime (Fig. 1b) can be related to a resonance absorption of the radiation with λ_m = 530 nm by Mn^{2+} ions [7, 8] occurring in the vicinity of V_S^{2+} vacancies in the upper part of the phosphor layer. This leads to an additional decrease in the intensity of emission in the region of ~530 nm observed for region IV and to a growth in intensity of the main EL peak related to the intracenter emission from Mn^{2+} ions (Fig. 1b) [7, 8].

The absence of the influence of IR irradiation on the EL spectra measured in the continuous excitation mode and in the pulse train excitation mode, with the IR irradiation produced during the action of excitation voltage pulses, is explained by the short duration of the pause between the excitation voltage pulses (<10 ms), which is insufficient for the formation of a significant concentration of additional deep vacancy centers V_S^+ at the IR photon flux density used in our experiments.

Conclusions. The results of our investigations show that the IR quenching of electroluminescence in ZnS:Mn-based ELTF emitters can be related to redistribution of the channels of impact excitation of Mn^{2+} centers and the deep centers related to the sulfur vacancies V_S^+ in the forbidden band of ZnS:Mn. The excitation events are redistributed in favor of V_S^+ centers, the concentration of which increases due to the IR irradiation in the pause between excitation voltage pulses. These results confirm the mechanism proposed previously to explain the effect of IR irradiation on the characteristics of ELTF emitters, agree with the estimates of the energy of centers related to the doubly charged sulfur vacancies V_S^{2+} (1.3 eV above the valence band top [2, 3, 11]), and refine the energy of V_S^+ centers (~1.9 eV below the conduction band bottom). The emission band peaked at ~495 nm can be attributed to the recombination radiation from donor–acceptor pairs related to the sulfur vacancies V_S^{2+}.

Acknowledgments. This study was supported by the Presidential Program of Support to the Leading Scientific Schools of Russia, project no. NSh-1482.2003.8.

REFERENCES

1. A. N. Georgobiani and Yu. G. Penzin, Luminestsentsiya **321** (1963).
2. N. T. Gurin, A. V. Shlyapin, O. Yu. Sabitov, and D. V. Ryabov, Pis'ma Zh. Tekh. Fiz. **29** (4), 14 (2003) [Tech. Phys. Lett. **29**, 134 (2003)].
3. N. T. Gurin, A. V. Shlyapin, O. Yu. Sabitov, and D. V. Ryabov, Zh. Tekh. Fiz. **73** (4), 90 (2003) [Tech. Phys. **48**, 469 (2003)].
4. N. T. Gurin, A. V. Shlyapin, and O. Yu. Sabitov, Pis'ma Zh. Tekh. Fiz. **28** (15), 24 (2002) [Tech. Phys. Lett. **28**, 631 (2002)].
5. M. F. Bulanyĭ, B. A. Polezhaev, and T. A. Prokof'ev, Fiz. Tekh. Poluprovodn. (St. Petersburg) **32**, 673 (1998) [Semiconductors **32**, 603 (1998)].
6. M. F. Bulanyĭ, A. V. Kovalenko, and B. A. Polezhaev, in *Proceedings of the International Conference on Luminescence, Moscow, 2001* (FIAN, Moscow, 2001), p. 98.
7. N. D. Borisenko, M. F. Bulanyĭ, F. F. Kodzhesperov, and B. A. Polezhaev, Zh. Prikl. Spektrosk. **55**, 452 (1991).
8. A. N. Gruzintsev, Doctoral Dissertation in Physics and Mathematics (Chernogolovka, 1997).
9. A. N. Gruzintsev, Mikroélektronika **28**, 126 (1999).
10. A. N. Georgobiani, A. N. Gruzintsev, Xu Xurong, and Lou Zidong, Neorg. Mater. **35**, 1429 (1999).
11. *Physics of II-VI Compounds*, Ed. by A. N. Georgobiani and M. K. Sheĭnkman (Nauka, Moscow, 1986) [in Russian].

Translated by P. Pozdeev

Technical Physics Letters, Vol. 30, No. 5, 2004, pp. 396–398. Translated from Pis'ma v Zhurnal Tekhnicheskoĭ Fiziki, Vol. 30, No. 10, 2004, pp. 1–5.

The Effect of Thermal Treatment on the Structure of Tantalum Oxide Films Grown on Titanium

V. A. Zhabrev, Yu. A. Bystrov, L. P. Efimenko*, A. E. Komlev, V. G. Baryshnikov, A. A. Kolomiĭtsev, and V. I. Shapovalov

Institute of Silicate Chemistry, Russian Academy of Sciences, St. Petersburg, 199155 Russia
St. Petersburg State Electrotechnical University, St. Petersburg, 197376 Russia
** e-mail: efimenko@isc1.nw.ru*

Received September 12, 2003; in final form, December 22, 2003

Abstract—We have studied amorphous films of tantalum oxide deposited onto titanium substrate by reactive magnetron sputtering. Subsequent annealing at temperatures above 600°C leads to crystallization with the formation of a β-Ta_2O_5 phase. Thermal treatment in air results in oxidation of the substrate with the formation of a rutile modification of titanium dioxide. © *2004 MAIK "Nauka/Interperiodica".*

Tantalum oxide films exhibit a broad spectrum of useful physical properties, which allows such films to be applied for solving various problems in modern electronics. The electret properties of tantalum oxide are of special interest since it was established [1, 2–4] that a quasi-static electric field can stimulate regenerative biological processes in living tissue. It can be expected that the application of the tantalum oxide films onto titanium clamps and implants [5, 6] will increase the efficacy of osteosynthesis and osteointegration processes. Unfortunately, no systematic data on the physicochemical properties of the Ta_2O_5/Ti system are available.

This Letter reports on the results of investigations of the general laws of crystallization of amorphous films of tantalum oxide grown on titanium substrates by means of reactive magnetron sputtering.

The sample films were obtained and studied in a standard high-vacuum system at a residual gas pressure of 5×10^{-4} Pa. An axial magnetron with a target made of chemically pure tantalum was operated in the dc mode. The setup was equipped with the ion etching facility. The films were grown in an Ar–O_2 atmosphere on substrates kept at a temperature of 300°C. The substrates were made of unpolished sheet titanium and had the dimensions of 12 × 12 mm. By means of optical ellipsometry and spectrophotometry in the visible spectral range, it was established that the films had a thickness of about 0.3 μm.

The chemical composition of the films was studied and their thicknesses determined by electron probe microanalysis (EPMA) on a Camebax setup. The EPMA measurements were performed using TaM_α and TiK_α lines measured using electron acceleration energies of 5 and 10 kV. It was found that the size of the X-ray generation zone for the TaM_α line excited at an electron energy of 5 kV is smaller than the film thickness: the intensity of the TiK_α line from the substrate was on a background level. The chemical composition of amorphous films determined using the 5-kV electron beam corresponded to (29.2 ± 1.8)Ta–(70.8 ± 1.8)O (at. %). Thus, the composition of as-deposited films is close to that of the stoichiometric Ta_2O_5 (28.6Ta–71.4O, at. %). With a 10-kV electron beam, the size of the X-ray generation zone for the TaM_α line exceeds the film thickness, as evidenced by the considerable intensity of the TiK_α line from the substrate.

The spatial resolution for the TaM_α line was evaluated by a conventional method [7]. A comparison of the results of calculations to the real dimensions of the X-ray generation zone for the TaM_α line excited at accelerating voltages of 5 and 10 kV showed that the effective film thickness falls within 0.1–0.4 μm. It should be noted that this estimate is based on the averaged surface density of the substance. Thus, the film thickness estimated by means of EPMA agree with the values obtained by optical methods.

The X-ray phase analysis was performed on a DRON-2 diffractometer using CuK_α radiation. The X-ray diffraction measurements were performed both immediately after deposition and upon additional thermal treatment. The thermal treatment was conducted for 1 h either in air or in vacuum (residual pressure below 10^{-3} Torr). The results of the X-ray diffraction analysis are presented in the table. As can be seen from these data, the as-deposited film is amorphous and the diffractogram displays almost exhaustively the peaks of titanium (Fig. 1a).

After thermal treatment for 1 h at 500°C in air, the film remained amorphous (the diffraction pattern was the same, displaying no new peaks). An increase in the temperature of thermal treatment to 600°C did not

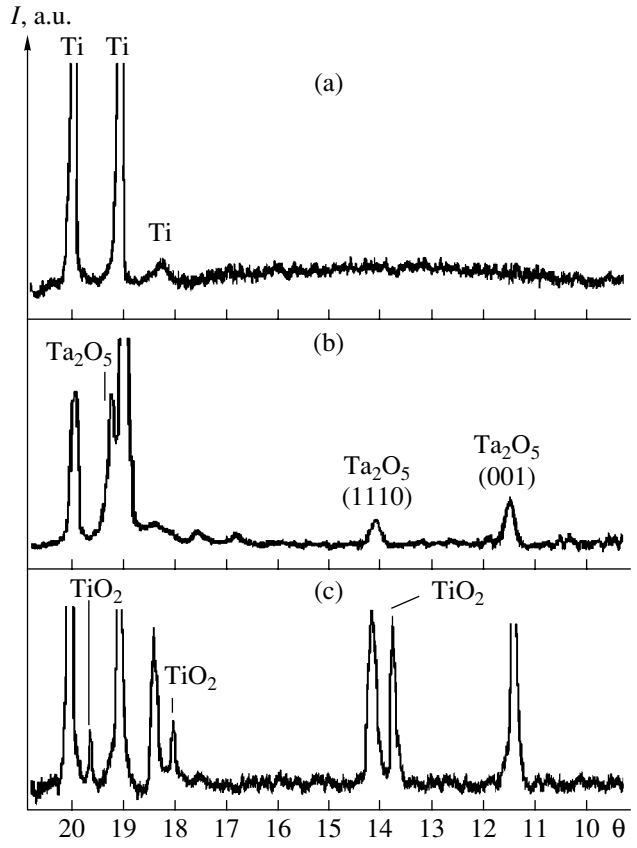

Fig. 1. X-ray diffraction patterns from Ta_2O_5 films on titanium substrate (a) immediately after deposition and (b, c) after subsequent thermal treatment for 1 h at 700°C in vacuum and in air, respectively.

change the overall structure of the Ta_2O_5 film, which still remained amorphous. However, the X-ray diffraction pattern exhibited the peaks of a rutile modification of titanium oxide, which was evidence of oxidation of the titanium substrate. Thermal treatment for 1 h at 700°C either in vacuum or in air resulted in crystallization of the film, which was manifested by a change in the X-ray diffraction pattern. The amorphous background disappeared and the diffractogram exhibited clearly pronounced peaks corresponding to β-Ta_2O_5 (Fig. 1b). The annealing in air, in addition, is accompanied by the oxidation of substrate manifested by intense peaks of TiO_2 in rutile modification (Fig. 1c). The X-ray diffraction patterns showed the presence of a growth texture in the Ta_2O_5 film, with a predominant grain orientation in the ⟨001⟩ direction of the orthorhombic Ta_2O_5 crystal structure. The ratio of intensities of the main peaks of Ta_2O_5 in our samples was $I(001)/I(1.11.0) = 2$, while this ratio in a powdered mixture is 0.85.

The results of X-ray phase analysis of as-deposited and annealed films of tantalum oxide on titanium substrates

Sample treatment	X-ray diffraction data	Film structure
As-deposited	Ti + amorphous phase	Amorphous
500°C, 1 h, air	"	"
600°C, 1 h, air	Ti, TiO_2(rutile), Ta_2O_5	"
700°C, 1 h, air	"	Crystalline
700°C, 1 h, vacuum	Ti, Ta_2O_5	"

The above results are in good agreement with published data on the laws of crystallization in amorphous Ta_2O_5 films grown by various methods on dielectric and semiconductor substrates (single crystal silicon, quartz, glass, ceramics) [8–16]. The annealing of such films at a temperature of 500°C even for a long time (up to 100 h) does not lead to the beginning of crystallization [14]. The treatment at 600°C requires dozens of hours for 20–30 vol % conversion into a crystalline phase [14], while on heating to 700°C, the peaks of crystalline Ta_2O_5 appear already after a 60-s annealing [16]. Thus, the laws of crystallization of Ta_2O_5 films on titanium substrate are analogous to those observed for the dielectric and semiconductor substrates.

Conclusions. We have obtained Ta_2O_5 films of nearly stoichiometric composition on titanium substrates by means of dc magnetron sputtering. It was found that subsequent annealing in an oxygen-containing atmosphere is accompanied by oxidation of the titanium substrate, with the formation of an intermediate layer of titanium oxide in the rutile modification at the heterogeneous interface.

The temperature and time regimes of crystallization observed in this study for Ta_2O_5 films on titanium substrates agree with the data published for analogous films on dielectric and semiconductor substrates. Thus, physicochemical nature of the substrate has no significant influence on the laws of crystallization of amorphous films of tantalum oxide.

REFERENCES

1. M. S. Morgunov, V. M. Muzhdaba, V. N. Tairov, *et al.*, Fiz. Tverd. Tela (Leningrad) **25**, 3431 (1983) [Sov. Phys. Solid State **25**, 1974 (1983)].
2. G. V. Efashkin and A. K. Chepurov, *Electrets Effect and Electrical Relaxation* (MIÉM, Moscow, 1979), pp. 226–237.
3. Z. Wang, J. Wang, Z. Xia, *et al.*, in *Proceedings of the 9th International Symposium on Electrets (ISE 9), Shanghai, 1996*, pp. 784–787.
4. J. Jiang, L. Cui, C. Song, *et al.*, in *Proceedings of the 10th International Symposium on Electrets (ISE-10), Delphi, Greece, 1999*, pp. 171–173.
5. R. A. Silva, M. Walls, B. Rondot, *et al.*, J. Mater. Sci.: Mater. Med. **13**, 495 (2002).

6. H. Matsuno, A. Yokoyama, F. Watari, *et al.*, Biomaterials **22**, 1253 (2001).
7. S. Reed, *Electron Microprobe Analysis* (Cambridge University Press, Cambridge, 1975; Mir, Moscow, 1979).
8. Z.-W. Fu, L.-Y. Chen, and Q.-Z. Qin, Thin Solid Films **340**, 164 (1999).
9. N. Ozer, J. Sol-Gel Sci. Technol. **8**, 703 (1997).
10. F. E. Ghodsi, F. Z. Tepehan, and G. G. Tepehan, Thin Solid Films **295**, 11 (1997).
11. K. Kukli, J. Aarik, A. Aidla, *et al.*, Thin Solid Films **260**, 135 (1995).
12. K. Kukli, M. Ritala, R. Matero, *et al.*, J. Cryst. Growth **212**, 459 (2000).
13. E. Franke, M. Schubert, C. L. Trimble, *et al.*, Thin Solid Films **388**, 283 (2001).
14. P. J. Beckage, D. B. Knorr, and X. M. Wu, J. Mater. Sci. **33**, 4375 (1998).
15. Peng-Heng Chang and Hung-Yu Liu, Thin Solid Films **258**, 56 (1995).
16. A. Pignolet, G. M. Rao, and S. B. Krupanidhi, Thin Solid Films **258**, 230 (1995).

Translated by P. Pozdeev

Technical Physics Letters, Vol. 30, No. 5, 2004, pp. 399–401. Translated from Pis'ma v Zhurnal Tekhnicheskoĭ Fiziki, Vol. 30, No. 10, 2004, pp. 6–11.

Holographic Spectrum Dividers for the UV Spectral Range

V. S. Obraztsov, A. G. Mikhaĭlova, and V. I. Podoba

Research Institute for Complex Testing of Optoelectronic Systems, Sosnovyĭ Bor, Leningrad oblast, Russia

e-mail: onv@niiki.ru

Received September 23, 2003

Abstract—We have theoretically and experimentally studied the possibility of using nonlinear recording of holographic mirrors for creating a spectrum divider capable of spatially separating wavelengths in the spectral region of 290–330 nm. © *2004 MAIK "Nauka/Interperiodica".*

Using holographic optical elements, it is possible to simplify the design, reduce the dimensions, and decrease the weight of optical systems, which is especially important for aerospace on-board instrumentation [1]. A considerable increase in the efficacy of such holographic elements is achieved when one device performs several functions. For example, the receivers of lidars detecting reflected signals at different wavelengths can be simplified by replacing a large-sized system of spectrum division by a device based on a single polychromatic holographic mirror comprising a set of reflection volume phase gratings conjugated in a single layer and ensuring spectral response in the required wavelength range.

Holographic mirrors are usually made of dichromated gelatin (DCG), which makes it possible to obtain holographic optical elements possessing a high diffraction efficiency and good working characteristics. Using well-developed technologies, DCG layers can be used for fabricating mirrors with a good spectral response in the range of wavelengths no shorter than 355 nm [2]. However, many lidar applications require elements capable of operating in a range of wavelength within 290–330 nm [3]. In some cases—for example, in lidars employing the principle of differential absorption [4]—it is also necessary to solve a complicated problem of the spatial separation of light beams with close wavelengths. It was demonstrated [5] that the response of nonlinear holographic mirrors in the above spectral range can be obtained using harmonics of the main diffraction maximum.

This study was devoted to theoretical analysis and experimental verification of the possibility of using nonlinear recording of holographic mirrors for creating a spectrum divider capable of spatially separating wavelengths in the spectral range 290–330 nm.

The experiments were performed with nonhardened DCG layers prepared as described elsewhere [6]. These layers are characterized by a higher sensitivity as compared to that achieved using other known methods [2, 7]. Prior to exposure, the DCG layers were kept for 1.0–1.5 h in air at a relative humidity of 5%. After exposure, the layers were allowed to swell in distilled water at 14–15°C. Then, the DCG layers were dehydrated in isopropyl alcohol solutions with concentrations from 50 to 100%. The final drying was performed for 1 h at 100°C in a thermal box.

The polychromatic holographic mirrors were recorded in crossed beams using an immersion cell with a mirror. The immersion medium was dehydrated kerosene. In order to obtain harmonics in the region of 290–330 nm, the main diffraction maximum for a normally incident light beam must fall (with allowance of the DCG index dispersion) within 600–680 nm. For this purpose, the angle of incidence of a parallel laser beam (λ = 515 nm) on the immersion cell was varied from 18° to 41°. This angular interval was selected taking into account that the DCG layer thickness upon preparation according to the above procedure increases by a factor of 1.12–1.17. Based on the results of calculations using the coupled wave theory [8], the initial DCG layer thickness was selected equal to 23 μm so as to obtain the spectral response of harmonics with a half-width on the order of 2 nm.

Theoretical analysis of the parameters of holographic mirrors was performed for the exposure characteristic of DCG layers approximated by the relation $n(E) = n_0(1 - \exp(-E/E_0))$, where n_0 and E_0 are the parameters of the exposure characteristic corresponding to the maximum amplitude of modulation of the DCG refractive index in the wavelength region of interest and the energy for which the modulation amplitude decreases by a factor of $1/(1 - \exp^{-1})$ relative to the maximum possible value [9]. The n_0 and E_0 values were determined by least squares using equations for the amplitudes of harmonic components of the index modulation profile [7]

$$n_i(z) = n_0 \exp(-E/E_0(1 + b))2I_i(z),$$

where i = 1 or 2 is the order of diffraction, b is the ratio of intensities of the interfering beams (equal to a product of the transmission coefficient of the responsive layer and the reflection coefficient of the mirror), z =

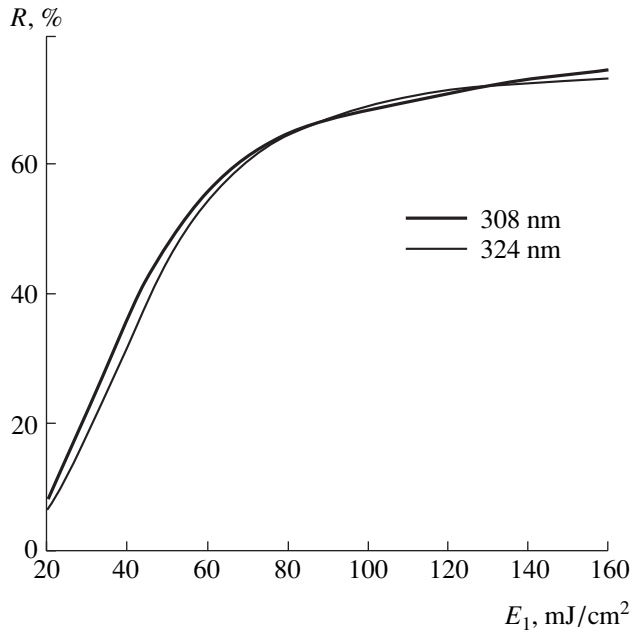

Fig. 1. Calculated plots of the reflection coefficients R of a spectrum divider at $\lambda = 308$ and 324 nm versus the intensity E_1 of light used for recording the first grating (the ratio of exposure energies for the first and second reflection volume gratings is $k = 0.93$). The ratio of intensities of the interfering beams is $b = 0.75$. Experimental data on the absorption coefficient of the developed DCG layer as a function of the exposure energy were approximated as $\alpha_{308}(E) = 5.1 \times 10^{-3} + 5 \times 10^{-5}E - 8.5 \times 10^{-8}E^2$; $\alpha_{324}(E) = 4.9 \times 10^{-3} + 2.7 \times 10^{-5}E - 8.5 \times 10^{-8}E^2$.

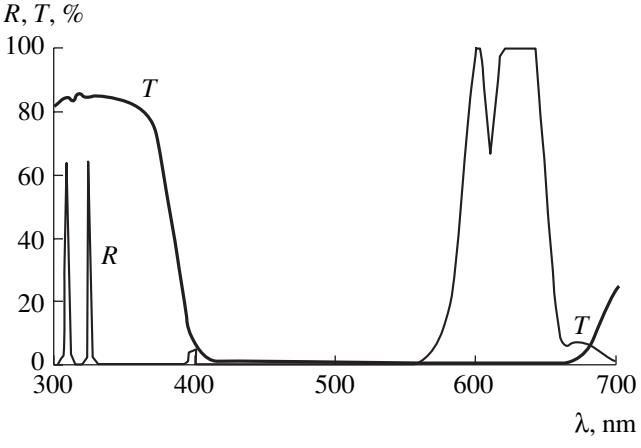

Fig. 2. The spectra of reflection R of the DCG-based spectrum divider and the transmission T of a UFS-5 glass filter.

$2\sqrt{b}\,E/E_0$, and $I_i(z)$ is the modified Bessel function of the ith order.

The values of modulation amplitudes $n_i(z)$ were determined using calibration plots of the optical density of a holographic mirror versus the amplitude of index modulation. The calibration plots were constructed using the Kogelnik formulas for the transmission coefficient of a reflection volume phase grating with a constant absorption coefficient [8]. The absorption coefficient was determined from the results of the optical density measurements outside the diffraction zone. The values of parameters determined using this procedure were $n_0 = 0.176$ and $E_0 = 167.4$ mJ/cm^2.

The exposure characteristic was used for optimization of the construction of a spectrum divider possessing maximum possible reflection coefficients at two wavelengths in the 290–330 nm range. The reflection coefficients were calculated using the Kogelnik formulas for the diffraction efficiency of a reflection volume phase grating with a constant absorption coefficient [8]. The amplitude of modulation of the first harmonics of the index profile was calculated as a function of the exposure energy using the data [7] for two reflection gratings recorded in the DCG layer. The results of calculations showed that the DCG layers employed allow a spectrum divider to be constructed for two wavelengths with reflection coefficients of up to 80% (Fig. 1).

Experimental values of the reflection coefficients of the two-wavelength spectrum dividers measured in the range 290–330 nm did not exceed 72%. Figure 2 shows the reflection spectrum of a device spatially separating the beams of 308 and 324 nm wavelengths. The reflection coefficients R of the mirrors for both wavelengths were 63%. The light beam intensity at the entrance of the immersion cell for recording of the first and second grating was $E_1 = 120$ mJ/cm^2 and $E_2 = 180$ mJ/cm^2 (cf. calculated $R = 71\%$ for both gratings at $E_1 = E_2 = 120$ mJ/cm^2). The beams with $\lambda = 308$ and 324 nm reflected from the spectrum divider were diverged approximately by 5°. The spectral halfwidths of both reflection bands did not exceed 3 nm. The discrepancy of the measured and calculated values of the light intensity for recording of the second grating is related to the effect of interrupted exposure [10].

Since the angles of high diffraction orders in reflection gratings coincide with the angle of the first-order diffraction, the beams of light in the spectral intervals 600–680 and 290–330 nm are superimposed on each other. This disadvantage is readily eliminated by covering the spectrum divider with a UFS-5 glass plate. The transmission spectrum of a 3-mm-thick UFS-5 glass plate is presented in Fig. 2.

Thus, we have developed a method of fabrication of spectrum dividers based on DCG layers capable of spatially separating light beams in the 295–330 nm range. The spectrum dividers are characterized by a high efficiency (the reflection coefficients at both 308 and 324 nm wavelengths exceed 60%) and provide for the spectral filtration with a reflection band halfwidth of less than 3 nm, which is acceptable for some lidar systems. The spectrum dividers can be obtained using DCG layers with thicknesses not exceeding 25 μm. Use of thicker layers complicates the chemicophotographic

procedure without additional gain in the reflection coefficients and the spectral halfwidth of the reflection bands.

REFERENCES

1. D. V. Guerra, G. K. Schwemmer, A. D. Wooten, *et al.*, J. Geophys. Res. **104**, 287 (1999).
2. J. Crespo, M. Pardo, M. A. Satorre, *et al.*, Appl. Opt. **32**, 3068 (1993).
3. S. E. Bisson, J. E. M. Goldsmith, and M. G. Mitchell, Appl. Opt. **38**, 1841 (1999).
4. D. J. Ball, A. E. Dudelzak, F. Rheault, *et al.*, Proc. SPIE **3494**, 223 (1998).
5. Z. N. Kalyashova, T. V. Kalyashov, G. A. Cheremisina, *et al.*, Proc. SPIE **3011**, 279 (1997).
6. Z. N. Kalyashova, Yu. E. Kuzilin, and A. G. Mikhaĭlova, RF Patent No. 2008716, Byull. Izobret., No. 4 (1994).
7. L. T. Blair, L. Solymar, and J. Takacs, Proc. SPIE **1136**, 12 (1989).
8. H. Kogelnik, Bell Syst. Tech. J. **48**, 2909 (1969).
9. D. I. Stasel'ko and A. S. Churaev, Opt. Spektrosk. **57**, 677 (1984) [Opt. Spectrosc. **57**, 411 (1984)].
10. N. Nishida and M. Sakaguchi, Appl. Opt. **10**, 439 (1971).

Translated by P. Pozdeev

Technical Physics Letters, Vol. 30, No. 5, 2004, pp. 402–403. Translated from Pis'ma v Zhurnal Tekhnicheskoĭ Fiziki, Vol. 30, No. 10, 2004, pp. 12–16.

Surface Barrier Sn–$CuInSe_2$ Junctions

Z. D. Kovalyuk, V. B. Orletskiĭ, O. N. Sydor, and V. V. Netyaga

Frantsevich Institute for Problems of Materials Science (Chernivtsy Department), National Academy of Sciences of Ukraine, Chernivtsy, Ukraine

e-mail: chimsp@unicom.cv.ua

Received December 9, 2003

Abstract—Photosensitive Schottky barriers were obtained by thermal deposition of tin onto *p*-type $CuInSe_2$ crystals. The temperature variation of the current–voltage characteristics of these structures is considered. For a direct bias voltage, both space-charge-limited current and thermoelectron emission components are present. Reverse biased structures are characterized by current generation in the space charge region and exhibit soft breakdown. The spectral dependence of a photocurrent (reduced to the incident photon number) shows that the obtained structures behave as wideband photoconverters. © *2004 MAIK "Nauka/Interperiodica".*

Introduction. The ternary semiconductor compound $CuInSe_2$ is widely used for obtaining absorbing layers in high-performance solar cells. This is related to the fact that the bandgap width of this semiconductor ($E_g \sim 1$ eV) falls within the wavelength interval of visible solar radiation and the material is characterized by an extremely high absorption coefficient ($\alpha \geq 10^5$ cm^{-1}) [1–3]. The photoconverters under consideration are based mostly on the heterojunctions between $CuInSe_2$ and CdS. A simple and cheap alternative is offered by structures of the metal–$CuInSe_2$ type.

Our analysis of the available literature showed the absence of communications about investigation of $CuInSe_2$ based Schottky diodes with tin as the barrier material. In this context, we have attempted to obtain such a structure and investigate the dominating mechanisms of current transfer and the main photoelectric characteristics of Sn/*p*-$CuInSe_2$ metal–semiconductor junctions.

Experimental results and discussion. $CuInSe_2$ crystals of the *p*-type were grown by the vertical Bridgman technique. The major carrier density and mobility at room temperature were $p = 6.0 \times 10^{17}$ cm^{-3} and $\mu = 15$ cm^2/(V s) [4]. The samples cut from the ingots had the dimensions $5 \times 5 \times 0.6$ mm. After mechanical polishing and chemical etching of the substrate crystal, a tin film (with a thickness of ≤ 0.5 μm) was deposited by thermal evaporation in vacuum. The ohmic contacts were formed by the thermal vacuum deposition of gold.

It should be noted that, as expected, the deposition of tin onto *n*-type $CuInSe_2$ crystals did not lead to the formation of a rectifying junction. In this case, tin forms a good ohmic contact and can be recommended as an alternative material to replace more expensive indium.

The current–voltage (*J*–*V*) characteristics of the sample structures measured at various temperatures in the range 242–323 K exhibit pronounced diode behavior (e.g., at an 0.7 V bias voltage, the room-temperature direct current is about 500 times the reverse current). In the interval of bias voltages $0 < V < 0.09$ V (Fig. 1a, region I), the double logarithmic *J*–*V* curves obey the Child–Langmuir law [5]

$$J = \frac{4\varepsilon\varepsilon_0}{9L^2}\left(\frac{2q}{m^*}\right)^{1/2} V^{3/2}, \quad (1)$$

where ε is the dielectric constant, ε_0 is the permittivity of vacuum, m^* is the effective mass of the major carrier, and L is the semiconductor thickness in the direction of current transfer.

For bias voltages within $0.09\text{ V} < V < 0.3$ V (Fig. 1a, region II), the current exhibits exponential growth described by the well-known law $J = J_s[\exp(qV/nkT) - 1]$, where the diode coefficient equal to $n \approx 1.6$ in the entire temperature range studied is indicative of the over-barrier current transfer. The saturation current density J_s varies from 6.9×10^{-6} to 2.9×10^{-4} A/cm^2, depending on the temperature.

In the interval $0.3\text{ V} < V < 1$ V (Fig. 1a, region III), the *J*–*V* curve can be described by the quadratic "trap" law [5],

$$J = \frac{9\varepsilon\varepsilon_0\theta\mu}{8L^3}V^2, \quad (2)$$

where μ is the hole mobility, $\theta = (N_v/N_t)\exp(-E_t/kT)$ is the ratio of the free charge to that trapped on shallow attachment levels, N_v is the effective density of states in the valence band, N_t is the density of trapping levels, and E_t is the trapping level energy above to the valence band.

The reverse branches of the *J*–*V* curves can be divided into two parts (Fig. 1b, regions IV and V). For small bias voltages ($V < -0.3$ V), the current is proportional to $|V|^{0.6}$, which reflects generation processes in

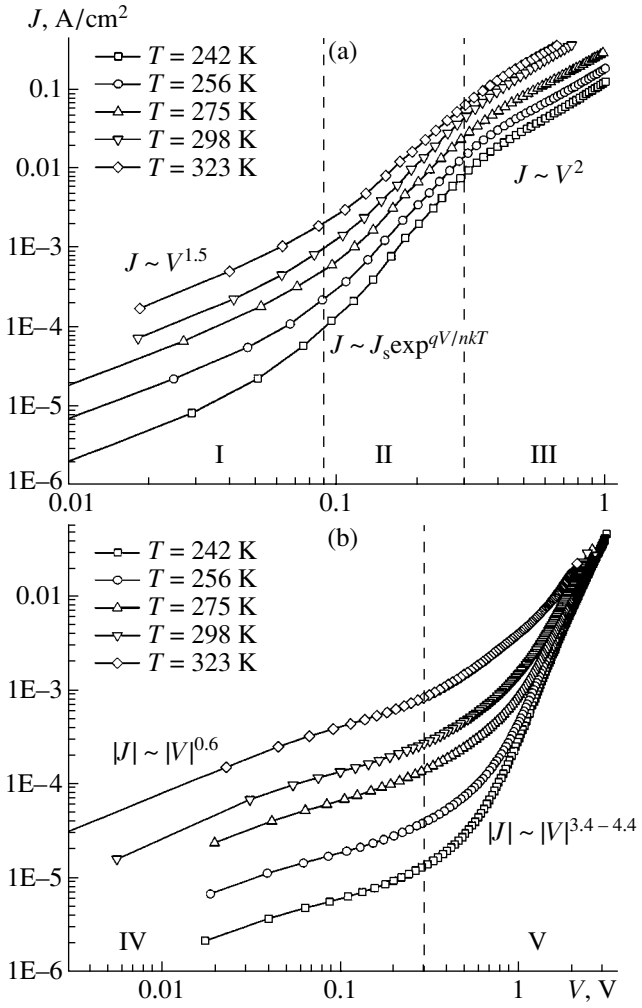

Fig. 1. Direct (a) and reverse (b) branches of the current–voltage characteristics of Sn/*p*-$CuInSe_2$ Schottky barriers measured at various temperatures and constructed in the double logarithmic scale.

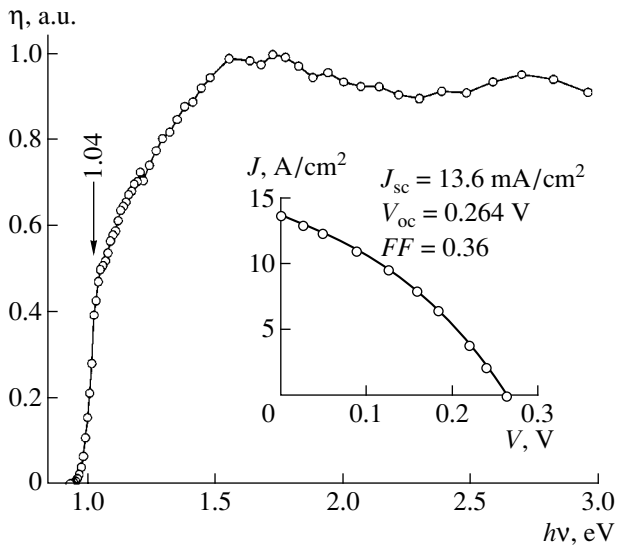

Fig. 2. The typical room-temperature spectrum of the relative quantum efficiency η of photoconversion in Sn/*p*-$CuInSe_2$ Schottky barriers. The inset shows the load curve and indicates the characteristics of the photovoltaic cell.

the space charge region [6]. In the region of greater bias voltages ($|V| > 0.9$ V), the characteristics can be described by the expression $J \sim |V|^{3.4–4.4}$ corresponding to soft breakdown.

The samples with Schottky barriers illuminated from the metal side exhibited a photovoltaic effect. For an incident light intensity of 100 mW/cm^2, the open circuit voltage was about $V_{oc} = 0.26$ V, the short circuit current density was about $J_{sc} = 13.6$ mA/cm^2, and the filling factor was equal to 0.36 (see the inset in Fig. 2). The maximum voltage responsivity at 293 K was 950 V/W, and the current response was 16 mA/W.

Figure 2 shows the typical spectrum of the relative quantum efficiency η of photoconversion at room temperature. The slope of the long-wavelength exponential photosensitivity threshold for the barriers studied (S = 60 eV^{-1}) corresponds to direct optical transitions, while the break at the photon energy $h\nu = 1.04$ eV agrees with the bandgap width E_g of $CuInSe_2$ [2]. The fact that the quantum efficiency keeps increasing for $h\nu > 1$ eV is indicative of suppressed surface recombination. This factor accounts for a wideband photoconversion, with a full width at half maximum $\delta_{1/2}$ of the $\eta(h\nu)$ spectrum being no less than 2 eV.

Conclusions. The values of the open circuit voltage and the short circuit current density obtained even for nonoptimized thicknesses of the metal film and the base semiconductor indicates that the Sn/*p*-$CuInSe_2$ junction is a promising structure for photoconverters operating in the visible and near-IR spectral regions. We believe that optimization of the structure will provide for a further increase in the characteristics presented above, which can be considered as sufficiently good for the initial stage of research and development of these barrier structures.

REFERENCES

1. *Current Topics in Photovoltaics*, Ed. by T. Coutts and J. Meakin (Academic, London, 1985; Mir, Moscow, 1988).
2. A. Rockett and R. W. Birkmire, J. Appl. Phys. **70** (7), R81 (1991).
3. A. M. Gabor, J. R. Tuttle, D. S. Albin, *et al.*, Appl. Phys. Lett. **65**, 198 (1994).
4. P. M. Gorleĭ, Z. D. Kovalyuk, V. B. Orletskiĭ, *et al.*, Zh. Tekh. Fiz. **74** (5), 141 (2004) [Tech. Phys. **49**, 658 (2004)].
5. M. Lampert and P. Mark, *Current Injection in Solids* (Academic Press, New York, 1970; Mir, Moscow, 1973).
6. B. Jagannathan and W. A. Anderson, Sol. Energy Mater. Sol. Cells **44**, 165 (1996).

Translated by P. Pozdeev

Technical Physics Letters, Vol. 30, No. 5, 2004, pp. 404–408. Translated from Pis'ma v Zhurnal Tekhnicheskoĭ Fiziki, Vol. 30, No. 10, 2004, pp. 17–25.

Relationship between the Generalized Lattice Model and the Ginzburg–Landau Theory

A. Yu. Zakharov*, M. A. Zakharov, and O. V. Loginova

Novgorod State University, Novgorod, Russia

** e-mail: ayz@novsu.ac.ru*

Received May 6, 2003; in final form, November 17, 2003

Abstract—It is established that the generalized lattice model of multicomponent condensed systems admits reduction to the Ginzburg–Landau theory, the parameters of which can be expressed via the characteristics of components and their interactions. The condition of mathematical correctness of applying the Ginzburg–Landau approximation to binary systems is found. An example of the concentration profile in a binary solution of components with equal specific volumes is considered. © *2004 MAIK "Nauka/Interperiodica".*

The generalized lattice model of multicomponent condensed systems proposed in [1, 2] and then developed in [3–7] takes into account both the differences in atomic sizes of the components (i.e., short-range parts of the interatomic potentials) and the long-range parts of the interatomic potentials. The equilibrium distributions of components in a given system are described by a set of integral equations, which are rather difficult to use for the calculation of equilibria.

This study was aimed at reducing the generalized lattice model to the Ginzburg–Landau theory.

1. Main equations of the generalized lattice model. Let us assume that the short-range part of the interatomic potential can be taken into account by introducing a limitation from above on the local density $n_i(\mathbf{r})$ of each component ($i = 1, ..., m$; m being the number of components in the system):

$$n_i(\mathbf{r}) \le \frac{1}{\omega_i}, \tag{1}$$

where ω_i is the limiting value of the inverse number density of particles. The latter quantity has the dimension of volume and is identified below with the proper atomic (specific) volume of the ith component.

Since the local fraction of a volume occupied by the ith component is $\omega_i n_i(\mathbf{r})$, the condition that every element of the space is occupied by a particle of some component of the system can be written as

$$\sum_{i=1}^{m} \omega_i n_i(\mathbf{r}) - 1 = 0. \tag{2}$$

The next condition consists in fixing the number of particles in the system. If the number of particles of each component is conserved, we have

$$\int_{(V)} n_i(\mathbf{r}) d\mathbf{r} - N_i = 0. \tag{3}$$

Thus, in the absence of chemical reactions and with neglect of thermal defects in a condensed system, the extrema of thermodynamic potentials have to be determined under conditions (2) and (3), irrespective of the forms of model expressions for these potentials.

The Helmholtz free energy F can be written in the following form:

$$F = \frac{1}{2}\sum_{i,j=1}^{m}\int\int_{(V)} K_{ij}(\mathbf{r}-\mathbf{r}')n_i(\mathbf{r})n_j(\mathbf{r}')d\mathbf{r}d\mathbf{r}' + T\sum_{i=1}^{m}\int n_i(\mathbf{r})\ln\left(\frac{n_i(\mathbf{r})}{n(\mathbf{r})}\right)d\mathbf{r}. \tag{4}$$

Here, the first term represents a configuration part of the free energy, the second is the entropy term, T is the absolute temperature in the energy units (the Boltzmann constant is $k = 1$), and $n(\mathbf{r}) = \sum_i n_i(\mathbf{r})$ is the total number density of particles.

The equilibrium distribution of components is determined proceeding from the requirement of minimum Helmholtz free energy (4) under conditions (2) and (3). Let us introduce the Lagrange functional

$$\mathcal{L}(\{n_i(\mathbf{r})\}, \{\Psi(\mathbf{r})\}, \mu_i) = F - \sum_{i=1}^{m}\mu_i\left[\int_{(V)} n_i(\mathbf{r})d\mathbf{r} - N_i\right] - \int_{(V)}\Psi(\mathbf{r})\left(\sum_{i=1}^{m}\omega_i n_i(\mathbf{r}) - 1\right)d\mathbf{r}, \tag{5}$$

which depends on the functions $n_i(\mathbf{r})$ and $\Psi(\mathbf{r})$ and the parameters μ_i (appearing as undetermined multipliers). A necessary condition for extremum of the free energy is that its functional derivatives with respect to $n_i(\mathbf{r})$ and $\Psi(\mathbf{r})$ and the usual partial derivatives with respect to μ_i are zero. This leads to the set of equations

$$\begin{cases} T\ln\left(\dfrac{n_i(\mathbf{r})}{n(\mathbf{r})}\right) + \displaystyle\sum_{j=1}^{m}\int_{(V)} K_{ij}(\mathbf{r}-\mathbf{r}')n_j(\mathbf{r}')d\mathbf{r}' - \omega_i\Psi(\mathbf{r}) - \mu_i = 0, \\ \displaystyle\sum_{i=1}^{m}\omega_i n_i(\mathbf{r}) - 1 = 0, \\ \displaystyle\int_{(V)} n_i(\mathbf{r})d\mathbf{r} - N_i = 0. \end{cases} \tag{6}$$

The equilibrium distribution of components must obey this set of nonlinear integral equations. Note that all components equally enter into this set of equations.

It should be emphasized that the functions $K_{ij}(\mathbf{r})$ entering into the Helmholtz free energy are not "true" interatomic potentials, because the introduction of proper atomic volumes ω_i forbids atoms to approach one another a distance shorter than

$$a_{ij} \simeq [(\omega_i)^{1/3} + (\omega_j)^{1/3}]. \tag{7}$$

Therefore, the functions $K_{ij}(\mathbf{r})$ represent only the long-range parts of the real interatomic potentials, obtained by truncation of the short-range parts (operative at distances smaller than or comparable with a_{ij}):

$$K_{ij}(\mathbf{r}) = \begin{cases} W_{ij}(\mathbf{r}), & |\mathbf{r}| \geq a_{ij}, \\ 0 & |\mathbf{r}| < a_{ij}, \end{cases} \tag{8}$$

where $W_{ij}(\mathbf{r})$ is the true interatomic potential.

Thus, within the framework of the approach outlined above, the short-range (singular) part of the interatomic potential is manifested via proper atomic volumes of the system components rather than directly contributing to the thermodynamic properties of systems.

2. Passage to the Ginzburg–Landau theory. The system has three characteristic spatial scales, representing atomic sizes a_0, the radius r_0 of long-range parts of interatomic potentials, and the distance b_0 over which the local densities of components exhibit significant variations. We assume that b_0 is the maximum of the three quantities:

$$a_0 \lesssim r_0 \ll b_0. \tag{9}$$

Taking this into account, expressions for the configuration part of free energy (4) can be transformed to

$$F_{\text{config}} = \frac{1}{2}\sum_{i,j=1}^{m}\int\int_{(V)} K_{ij}(\mathbf{r}-\mathbf{r}')n_i(\mathbf{r})n_j(\mathbf{r}')d\mathbf{r}d\mathbf{r}'. \tag{10}$$

For $|\mathbf{r}-\mathbf{r}'| \ll b_0$, we obtain

$$\begin{aligned} n_j(\mathbf{r}') &\approx n_j(\mathbf{r}) + \sum_{s=1}^{3}\frac{\partial n_j(\mathbf{r})}{\partial x_s}(x_s' - x_s) \\ &+ \frac{1}{2}\sum_{s_1,s_2=1}^{3}\frac{\partial^2 n_j(\mathbf{r})}{\partial x_{s_1}\partial x_{s_2}}(x_{s_1}' - x_{s_1})(x_{s_2}' - x_{s_2}), \end{aligned} \tag{11}$$

where x_s and x_s' denote the Cartesian components of vectors $\mathbf{r}$ and $\mathbf{r}'$, respectively. Substituting (11) into (10), integrating with respect to $\mathbf{r}'$ (since all the potentials $K_{ij}(\mathbf{r})$ are central, all the odd momenta are zero), and taking additional integration by parts, we eventually obtain

$$\begin{aligned} F = \int d\mathbf{r}\Bigg\{ &-\frac{1}{12}\sum_{i,j}K_{ij}^{(2)}(\nabla n_i(\mathbf{r}), \nabla n_j(\mathbf{r})) \\ &+ \frac{1}{2}\sum_{i,j}K_{ij}^{(0)}n_i(\mathbf{r})n_j(\mathbf{r}) + T\sum_{i=1}^{m}n_i(\mathbf{r})\ln\left(\frac{n_i(\mathbf{r})}{n(\mathbf{r})}\right)\Bigg\}, \end{aligned} \tag{12}$$

where $K_{ij}^{(p)}$ are certain integral characteristics of the interatomic potentials

$$K_{ij}^{(p)} = \int K_{ij}(\mathbf{r}')|\mathbf{r}'|^p d\mathbf{r}'. \tag{13}$$

Functional (12) has a form similar to that of the Ginzburg–Landau functional, but, in contrast to the latter,

(i) Equation (12) is not restricted to terms of finite orders with respect to the order parameters, and

(ii) all the parameters in Eq. (12) have a clear physical meaning.

Finding the extremum of functional (12) with additional conditions (2) and (3), we readily obtain a set of equations for the equilibrium distribution of components,

$$\begin{cases} \dfrac{1}{6}\displaystyle\sum_{j=1}^{m}K_{ij}^{(2)}\Delta n_j(\mathbf{r}) + \sum_{j=1}^{m}K_{ij}^{(0)}n_j(\mathbf{r}) \\ + T\ln\left(\dfrac{n_i(\mathbf{r})}{n(\mathbf{r})}\right) - \omega_i\Psi(\mathbf{r}) - \mu_i = 0; \\ \displaystyle\sum_{j=1}^{m}\omega_j n_j(\mathbf{r}) - 1 = 0; \\ \displaystyle\int_{(V)} n_i(\mathbf{r})d\mathbf{r} - N_i = 0, \end{cases} \tag{14}$$

where Δ is the Laplace operator.

3. Heterogeneous states in a binary solution. As a simple example of application of the proposed approach, let us consider the problem of determining the concentration profile of a two-component ($m = 2$) solution of components with equal specific volumes ($\omega_1 = \omega_2 = \omega$, $n(\mathbf{r}) = \text{const} = 1/\omega$). Functional (12) depends on a single independent variable $y(\mathbf{r}) = \omega n_1(\mathbf{r}) = \dfrac{n_i(\mathbf{r})}{n(\mathbf{r})}$ representing the local molar fraction of the first component and has the following form:

$$F = \int d\mathbf{r}\left\{-\frac{1}{12\omega^2}K^{(2)}(\nabla y(\mathbf{r}))^2\right.$$

$$+\frac{1}{2\omega^2}[K^{(0)}y^2(\mathbf{r}) - Q^{(0)}y(\mathbf{r}) + K_{22}^{(0)}] \qquad (15)$$

$$\left.+\frac{T}{\omega}[y(\mathbf{r})\ln y(\mathbf{r}) + (1-y(\mathbf{r}))\ln(1-y(\mathbf{r}))]\right\},$$

where

$$K^{(2)} = \sum_{i,j=1}^{2}(-1)^{i+j}K_{ij}^{(2)}, \quad K^{(0)} = \sum_{i,j=1}^{2}(-1)^{i+j}K_{ij}^{(0)},$$

$$Q^{(0)} = 2K_{22}^{(0)} - K_{12}^{(0)} - K_{21}^{(0)}.$$

From this we obtain the necessary condition of mathematical correctness of Ginzburg–Landau approximation (15) for the binary system under consideration,

$$K^{(2)} < 0, \qquad (16)$$

since otherwise functional (15) is not limited from below.

The condition of extremum of the free energy, $\delta F/\delta y(\mathbf{r}) = 0$, yields

$$\frac{1}{6}K^{(0)}\Delta y(\mathbf{r}) + f(y(\mathbf{r})) = 0, \qquad (17)$$

where

$$f(y) = K^{(0)}y - \frac{Q^{(0)}}{2} + \omega T\ln\left(\frac{y}{1-y}\right). \qquad (18)$$

This equation describes the equilibrium distribution of components in the binary solution.

3.1. Compositions of coexisting phases. A necessary condition for the existence of heterophase states in the system under consideration is the nonmonotonic character of the function $f(y)$ in the interval $0 < y < 1$. Indeed, in the bulk of each phase, we have $\Delta y(r) = 0$ and, hence, the function $f(y)$ turns zero for each composition of the coexisting phases, which is possible only if this function is nonmonotonic.

Elementary investigation of the function $f(y)$ shows that, for any values of the parameters $K^{(0)}$ and $Q^{(0)}$ and temperature T, this function has at least one root in the (0, 1) interval. If new roots appear, both the function $f(y)$ and its derivative $f'(y)$ vanish at this point, so that the corresponding critical point must satisfy the following set of equations for the unknown temperature and composition y:

$$\begin{cases} K^{(0)}y - \dfrac{Q^{(0)}}{2} + \omega T\ln\left(\dfrac{y}{1-y}\right) = 0, \\ K^{(0)} + \dfrac{\omega T}{y(1-y)} = 0. \end{cases} \qquad (19)$$

Excluding the temperature, we obtain a closed equation for the critical composition,

$$\frac{Q^{(0)}}{2K^{(0)}} = y - y(1-y)\ln\left(\frac{y}{1-y}\right), \qquad (20)$$

from which it follows that the necessary and sufficient condition for the existence of a critical point (and, hence, of heterophase states) in this model system consists in simultaneously obeying two inequalities,

$$\begin{cases} K^{(0)} < 0, \\ 0 < \dfrac{Q^{(0)}}{2K^{(0)}} < 1. \end{cases} \qquad (21)$$

The first of these conditions is known as the Gorsky–Bragg–Williams (GBW) criterion. It should be emphasized that meeting only the GBW condition is insufficient for the existence of a phase transition. Set of inequalities (21) is equivalent to

$$\begin{cases} K_{22}^{(0)} - K_{12}^{(0)} < 0, \\ K_{11}^{(0)} - K_{12}^{(0)} < 0, \end{cases} \qquad (22)$$

where we take into account that $K_{12}^{(0)} = K_{21}^{(0)}$.

Let us assume that conditions (22) for the existence of a phase transition in the system are satisfied. Since the right-hand part of Eq. (20) monotonically increases in the interval $0 < y < 1$ and has values also confined

between 0 and 1, this equation has a single solution that can be readily obtained by numerical methods.

Consider the simplest partial case of $K_{11}^{(0)} = K_{22}^{(0)}$, in which Eq. (20) can be solved analytically. In this case, $y_c = 0.5$ and the critical temperature T_c is related to y_c as

$$K^{(0)} = -4y_c(1-y_c)\omega T_c. \quad (23)$$

Excluding $K^{(0)}$ and $Q^{(0)}$ from (18), we obtain an equation relating the compositions of coexisting phases to the temperature:

$$f(y) = -4\omega T_c(y-0.5) + \omega T \ln\left(\frac{y}{1-y}\right) = 0. \quad (24)$$

For $T < T_c$, this equation has three roots, $y_1 < y_2 < y_3$, such that $y_2 = 0.5$ and $y_1 + y_3 = 1$. For $T \ll T_c$, the asymptotic expressions for y_1 and y_3 are

$$\begin{cases} y_1 \approx \exp\left(-\dfrac{2T_c}{T}\right), \\ y_3 \approx 1 - \exp\left(-\dfrac{2T_c}{T}\right). \end{cases} \quad (25)$$

Let us introduce a dimensionless temperature, $\tau = (T_c - T)/T_c$ ($|\tau| \ll 1$), and a small parameter $\xi = 0.5 - y$ in the vicinity of the critical point. The two quantities are related as

$$4\xi^2 - 3\tau = 0, \quad (26)$$

which corresponds to the well-known mean-field approximation.

3.2. Concentration profile. First, let us consider the concentration profile in the case of a flat interface (with the abscissa axis directed along the normal to this plane) in the vicinity of the critical temperature. Passing from $y(x)$ to the variable $\xi(x) = 0.5 - y(x)$ ($|\xi(x)| \ll 1$), we can rewrite Eq. (17) as

$$\frac{K^{(2)}}{24\omega T_c}\xi''(x) + \xi(x)\left[-\tau + \frac{4\xi^2(x)}{3}\right] = 0. \quad (27)$$

Upon decreasing the order, we obtain a much simpler relation:

$$\frac{K^{(2)}}{24\omega T_c}[\xi'(x)]^2 - \tau\xi^2(x) + \frac{2}{3}\xi^4(x) + C_1 = 0. \quad (28)$$

The integration constant C_1 can be determined from the condition that $\xi'(x)$ vanishes in the bulk of the phase for the equilibrium composition (26), which yields $C_1 = 3\tau^2/8$. This further simplifiers Eq. (28) to

$$\frac{K^{(2)}}{16\omega T_c}[\xi'(x)]^2 + \left(\xi^2(x) - \frac{3\tau}{4}\right)^2 = 0, \quad (29)$$

the solution of which is

$$\xi(x) = \frac{\sqrt{3\tau}}{2}\tanh\left[2\sqrt{\frac{3\tau\omega T_c}{-K^{(2)}}}x\right]. \quad (30)$$

Note that, according to (16), the parameter $K^{(2)}$ is negative, while the integration constant is taken equal to zero owing to the arbitrary choice of the origin for the coordinate x. Now, we readily obtain a relationship between the characteristic thickness d of the phase boundary and the characteristics of interatomic potentials in the system studied:

$$d \simeq \frac{1}{2}\sqrt{\frac{-K^{(2)}}{3\tau\omega T_c}} \propto \tau^{-1/2}. \quad (31)$$

As expected, the temperature dependence of d corresponds to the effective field approximation.

4. Conclusions. Within the framework of the generalized lattice model of multicomponent condensed systems, we have reduced Helmholtz free energy functional (4) to functional (12) of the Ginzburg–Landau type. Advantages of the latter are as follows:

(i) Expression (12) contains no unknown functions of the general kind (such as interatomic potentials $K_{ij}(\mathbf{r})$); instead, it contains a finite number of their simple characteristics represented by the numerical parameters $K_{ij}^{(p)}$ (13).

(ii) Analysis and solution of set of equations (14) are much simpler than finding a solution of set of integral equations (6).

(iii) The inverse problem of finding the parameters of the theory from experimental data (e.g., from the phase diagrams) using Eqs. (6) is extremely difficult; with functional (12), this task becomes quite realizable.

(iv) Solutions obtained using functional (12) can be used as the initial approximation in solving problems for functional (6).

Using the proposed approach, we have also refined the Gorsky–Bragg–Williams criterion for the existence of phase transitions in a binary system, determined the compositions of coexisting phases at low ($T \ll T_c$) temperatures, and calculated the concentration profile in the vicinity of the critical point ($|T - T_c| \ll T_c$) for a binary solution with equal atomic volumes of the components.

Acknowledgments. The authors are grateful to the referee for his useful remark.

This study was supported in part by the Federal Program "Universities of Russia" (project no. UR.01.01.024), the Russia–Netherlands Cooperation Program (NWO project no. 047.011.2001.011), the Federal Program "Integration" (project no. B0056), and the Russian Foundation for Basic Research (project no. 03-01-00574).

REFERENCES

1. A. Yu. Zakharov and S. V. Terekhov, *Mathematical Problems of Chemical Thermodynamics* (Nauka, Novosibirsk, 1985), p. 173.
2. A. Yu. Zakharov and S. V. Terekhov, Fiz. Met. Metalloved. **59**, 261 (1985).
3. S. V. Terekhov and E. L. Korzun, Zh. Fiz. Khim. **64**, 1203 (1990).
4. S. V. Terekhov, Izv. Akad. Nauk SSSR, Met., No. 5, 42 (1991).
5. M. A. Zakharov, Fiz. Tverd. Tela (St. Petersburg) **41**, 60 (1999) [Phys. Solid State **41**, 51 (1999)].
6. M. A. Zakharov, Fiz. Tverd. Tela (St. Petersburg) **41**, 1609 (1999) [Phys. Solid State **41**, 1476 (1999)].
7. M. A. Zakharov, Fiz. Tverd. Tela (St. Petersburg) **42**, 1234 (2000) [Phys. Solid State **42**, 1270 (2000)].

Translated by P. Pozdeev

Technical Physics Letters, Vol. 30, No. 5, 2004, pp. 409–410. Translated from Pis'ma v Zhurnal Tekhnicheskoĭ Fiziki, Vol. 30, No. 10, 2004, pp. 26–30.

The Electric Conductivity of Nanodimensional Cobalt Oxide in a Porous Glass

V. N. Pak* and O. Yu. Solomatina

Herzen State Pedagogical University, St. Petersburg, Russia

** e-mail: pak@vp7609.spb.edu*

Received December 16, 2003

Abstract—Cobalt(II) oxide was introduced in an amount of 3.5–56.4 mass % into a porous glass by repeated cycles of impregnation with an aqueous solution of cobalt(II) nitrate followed by dehydration and thermal decomposition of the salt. The results of conductivity measurements, in combination with the data on the cobalt oxide volume and the specific area of the porous carrier, reflect the formation of sequential cobalt oxide monolayers on the surface of pore walls. *© 2004 MAIK "Nauka/Interperiodica".*

Porous glasses in which the pore radius can be reliably controlled in the range r = 2–100 nm [1, 2] offer wide possibilities for the investigation of substances in the nanodimensional state. It is important that porous glasses with highly developed pore structure and surface allow the compounds to be introduced in amounts sufficient for the experimental investigation [1–4]. The nanoparticles and monolayers of transition metal oxides in porous glasses are promising materials in which dimensional features of the phase transitions and the optical, magnetic, and sensor properties are well manifested [1, 2, 5–7].

However, peculiarities of the electric conductivity in such systems with a relatively small number of atoms (10^{15}–10^{16} cm^{-2}) of a d element in the oxide formed at the initial stage of filling of the silica gel surface remain unstudied. Determination of the character of conductivity variation in systems not possessing completely formed band structure is of interest because this knowledge may elucidate the basic questions concerning the form and dimensional features of deposited oxides in porous glasses.

The results reported in this Letter demonstrate an unusual stepwise increase in the electric conductivity in the course of cobalt oxide deposition in a porous glass. The experiments were performed on porous glass plates prepared using standard methods [1–4] with dimensions of 10 × 10 × 1 mm, a predominant pore radius of r = 4.5 nm, a porosity of ε = 0.166 cm^3/g, and a specific surface of S = 80 m^2/g. The porous glass was modified by adding cobalt oxide through diffusion impregnation of the plates with an aqueous solution of cobalt(II) nitrate with a concentration of 0.5–1.5 mol/l, followed by dehydration at 120°C and thermal decomposition of the intercalated salt by heating in air at 400°C. Repeated cycles of this treatment allowed the oxide "growth" on the walls of through channels in the porous glass to be performed in a controlled way and reliably monitored by weighing.

The results of spectroscopic measurements confirmed with sufficient confidence the formation of cobalt(II) oxide. Indeed, the electronic absorption spectra of porous glass plates with deposited cobalt oxide (CoO/PG) measured in the diffuse reflectance mode (SF-10 spectrophotometer) display a broad absorption band with a maximum at 540–560 nm corresponding to the d–d transition $^4T_{1g} \longrightarrow {}^4T_{1g}(P)$ in divalent cobalt in octahedral oxygen environment [8]. The X-ray photoelectron spectrum (ES-2401 spectrometer, MgK_α radiation) exhibits an intense Co 2p core-shell electron peak with a binding energy of 781.5–782 eV characteristic of CoO [9].

The nanodimensional state of cobalt oxide deposited in a porous glass is confirmed by the fact that, despite a considerable content (reaching up to 56% of the mass of porous glass), the sample remains X-ray amorphous. This behavior is related to the highly developed surface of the carrier. Indeed, being reduced to a specific surface area of S = 80 m^2/g, the above percentage content corresponds to a surface density of ~6 × 10^{15} oxide formula units per square centimeter.

The dc electric resistance was measured across the CoO/PG samples with clamp electrodes using an electrical scheme described elsewhere [3, 4]. The conductivity was calculated in the first approximation with allowance of the real size of the glass plate. These values are the integral characteristics of CoO/PG samples. The assignment to a conducting component would require model estimates of the effective cross section and length of the distributed oxide, which is outside the scope of this study.

In the first region of the plot of $\log\sigma$ versus the content Q of cobalt oxide in the glass (see figure), the conductivity exhibits a monotonic increase followed by a

1063-7850/04/3005-0409$26.00 © 2004 MAIK "Nauka/Interperiodica"

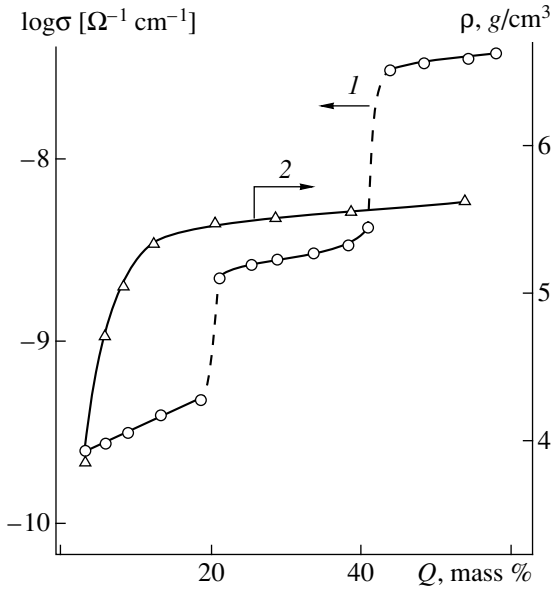

Plots of the (*1*) logarithm of conductivity of CoO/PG plates and (*2*) effective density of the cobalt oxide layer versus percentage content of cobalt oxide in the porous glass.

sharp jump in the region of $Q = 21$–22%. This behavior allowed us to suggest that the initial deposition stage consists in the uniform growth of weakly conjugated two-dimensional islands (clusters) followed by the intense formation of multiple contacts between these islands in the percolation region. The formation of a nonplanar cluster structure seems to be less probable: in such a case, we have to explain why rather distant three-dimensional oxide clusters on reaching $Q \sim 22\%$ suddenly "spread" over the surface to merge and provide for the observed jump in the conductivity.

The formation of a cobalt oxide monolayer at $Q \sim 22\%$ can be indirectly confirmed by comparing the specific surface of the porous glass ($S = 80$ m^2/g) to the volume of oxide. The latter can be reliably determined by the method of capillary filling with water [1, 3, 4] as the difference $\varepsilon_0 - \varepsilon$ between the specific free volumes of the pore space in the initial and modified glass, respectively. These geometric parameters provide for a physically justified estimate of an effective thickness of the deposited oxide layer determined as

$$h = (\varepsilon_0 - \varepsilon)/S. \quad (1)$$

For a cobalt oxide content of $Q = 22.2\%$ corresponding to the σ jump (see the figure), this formula yields $h = 5.1$ Å, which is close to the linear dimensions of a $[CoO_6]$ polyhedron according to the crystallochemical data [10].

If the mechanism and rate of oxide deposition are retained, we expect the appearance of the second step in the $\log\sigma(Q)$ curve in the region of $Q \sim 45\%$. This is just what was observed in experiment (see figure), where a gradual increase in the conductivity (like that in the first step) is followed by a sharp jump in the vicinity of $Q = 45\%$.

Thus, there is ground to believe that "step-by-step" increase in the mass fraction of the cobalt oxide proceeds under the conditions of a strong interaction with the carrier surface preventing coalescence of the deposit. This makes possible "grafting" of the monolayer of cobalt oxide polyhedra (representing essentially the surface cobalt(II) polysilicate) onto the silica gel surface and the subsequent layer-by-layer oxide growth under the aligning action of the first monolayer.

It was also of interest to trace the "dimensional" change in the cobalt oxide density defined as

$$\rho = Q/(\varepsilon_0 - \varepsilon) \quad (2)$$

accompanying the increase in the oxide content in the porous glass (see figure). The low initial value and gradual increase in ρ reflect the enhanced conjugation of $[CoO_6]$ polyhedra in the growing oxide clusters. Completion of the formation of the first oxide monolayer corresponds to reaching a density close to the lower values (5.7–6.7 g/cm^3) published for the bulk CoO [10], while the supermonolayer growth leads to further but slight increase in the ρ value.

REFERENCES

1. G. P. Roskova and T. S. Tsekhomskaya, Fiz. Khim. Stekla **7**, 513 (1981).
2. D. Enke, F. Janovski, and W. Schwieger, Microporous Mesoporous Mater. **60** (1–3), 19 (2003).
3. R. L. Verezhinskaya, T. M. Burkat, V. N. Pak, and V. V. Rychgorskiĭ, Fiz. Khim. Stekla **25**, 688 (1999).
4. V. N. Pak, R. L. Verezhinskaya, and T. M. Burkat, Zh. Fiz. Khim. **76**, 1324 (2002).
5. P. T. Sotomayor, I. M. Raimundo, A. J. G. Zarbin, *et al.*, Sens. Actuators A **74**, 157 (2001).
6. I. V. Golosovsky, I. Mirebeau, J. Andre, *et al.*, Phys. Rev. Lett. **86**, 5783 (2001).
7. D. Sunil, H. D. Gafney, M. H. Rafailovich, *et al.*, J. Non-Cryst. Solids **319**, 154 (2003).
8. C. J. Ballhausen, *Introduction to Ligand Field Theory* (McGraw-Hill, New York, 1962; Mir, Moscow, 1964).
9. C. D. Wagner, W. M. Riggs, L. E. Davis, *et al.*, *Handbook of X-ray Photoelectron Spectroscopy* (Perkin-Elmer, Minnesota, 1978).
10. V. A. Rabinovich and Z. Ya. Khavin, *A Short Handbook on Chemistry*, Ed. by A. A. Potekhin and A. E. Efimov (Khimiya, Leningrad, 1991).

Translated by P. Pozdeev

Technical Physics Letters, Vol. 30, No. 5, 2004, pp. 411–414. Translated from Pis'ma v Zhurnal Tekhnicheskoĭ Fiziki, Vol. 30, No. 10, 2004, pp. 31–38.

The Role of Fast Electrons in the Formation of a Pulsed Volume Discharge at Elevated Gas Pressures

I. D. Kostyrya[a], V. S. Skakun[a], V. F. Tarasenko[a,*], A. N. Tkachev[b], and S. I. Yakovlenko[b,]**

[a] *Institute of High-Current Electronics, Siberian Division, Russian Academy of Sciences, Tomsk, Russia*
[b] *Institute of General Physics, Russian Academy of Sciences, Moscow, Russia*
*e-mail: * vft@loi.hcei.tsc.ru; ** syakov@kapella.gpi.ru*
Received August 8, 2003; in final form, January 16, 2004

Abstract—A volume electric gas discharge was obtained using a pulsed inhomogeneous electric field without a preionization source in various gases (nitrogen, air, helium, neon, argon, krypton) at elevated pressures. In air at atmospheric pressure and nanosecond voltage pulses, the specific energy deposited in the gas amounted up to ~1 J/cm^3. The mechanism of the volume discharge formation is related to the appearance of fast (keV-energy) electrons emitted from plasma formations at the cathode. Fast electrons provide for the effective preionization of the gas in the interelectrode space and favor the formation of volume discharge. Under these conditions, the maximum voltage drop across the discharge gap is achieved in the quasi-stationary stage of discharge. *© 2004 MAIK "Nauka/Interperiodica".*

Introduction. The volume electric discharge in atomic and molecular gases and their mixtures at high pressures is usually formed with preionization in the discharge gap achieved using various sources of ionizing radiation [1]. Such discharge plasmas are widely used in pulsed lasers [2]. However, it is known [3, 4] that a diffuse discharge at atmospheric pressure can also be obtained without preionization by applying nanosecond pulses of inhomogeneous electric field with sharp leading fronts (from a fraction of a nanosecond to a few nanoseconds).

Recently [5–8], we succeeded in obtaining electron beams with record current amplitudes (~70 A in air and up to ~200 A in helium) from a volume discharge in a gap with inhomogeneous electric field. It was suggested [5] and then proved that the electron beam is formed in the stage when the plasma, formed at the cathode, expands to closely approach the anode. The formation of a high-current electron beam at a high pressure was explained by the existence of upper branches in the current–voltage characteristics, determining the criteria of both electron runaway and discharge initiation (Paschen curve) [9, 10]. However, neither causes nor conditions of the volume discharge formation during nanosecond pulses of inhomogeneous electric field have been studied so far.

This study was aimed at elucidating the mechanism of a volume electric discharge formation in a pulsed inhomogeneous electric field of nanosecond duration.

Experimental. The experiments were performed with nanosecond pulse generators of the RADAN type described in detail elsewhere [11, 12]. Generator 1 (RADAN-303 [5]) possessed an output wave impedance of 45 Ω and produced in a matched load a voltage pulse with an amplitude from 50 to 170 kV (at an open circuit voltage of up to 340 kV), a full width at half maximum (FWHM) of ~5 ns, and front width of ~1 ns [11]. Generator 2 (RADAN-220) had an output wave impedance of 20 Ω and produced in the discharge gap a voltage pulse with an amplitude of up to ~220 kV, a FWHM of ~2 ns, and a front width of ~0.3 ns [12].

The gas diode design was the same for both generators, comprising a plane anode and a tube cathode with a small radius of curvature providing for an additional field enhancement near the cathode [7]. In most cases, the cathode was a tube with a diameter of 6 mm made of a 50-μm-thick steel foil. The role of the flat anode was performed by a foil or by a grid with a geometric transparency of 20–70%. The cathode–anode spacing could be varied within 13–20 mm. In some experiments, the discharge gap was placed in a special gas chamber provided with viewing ports and a pumping stage, which allowed the gas to be pumped out and the gas phase composition and pressure in the discharge gap to be controlled. In this study, the experiments with volume discharge formation were performed with air, nitrogen, helium, neon, argon, and krypton.

The signals from collectors, voltage dividers, and shunts were measured using a digital oscillograph of the TDS-684B type with a bandwidth of 1 GHz and a sensitivity of 5 G/s (which corresponds to 5 points/ns). Alternatively, the measurements were performed with an oscillograph of the TDS-334 type possessing an 0.3 GHz bandwidth and a sensitivity of 2.5 G/2s

1063-7850/04/3005-0411$26.00 © 2004 MAIK "Nauka/Interperiodica"

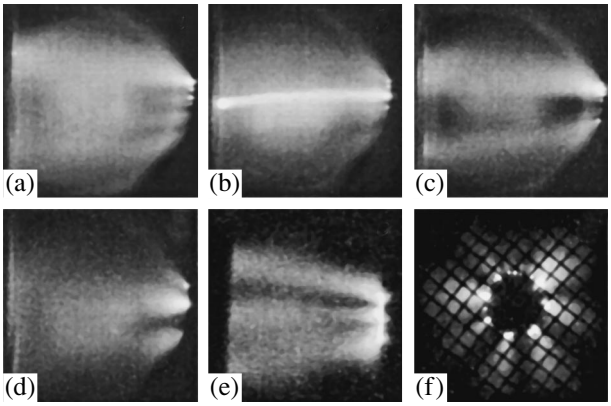

Fig. 1. Photographs of the volume discharge in (a, b) argon, (c, d) krypton, and (e, f) air taken (a–e) from the side and (f) via the anode grid. Regime: generator 2; interelectrode gap width, 16 mm; gas pressure (bar): 1 (a, c, e, f), 0.75 (b), 0.25 (c).

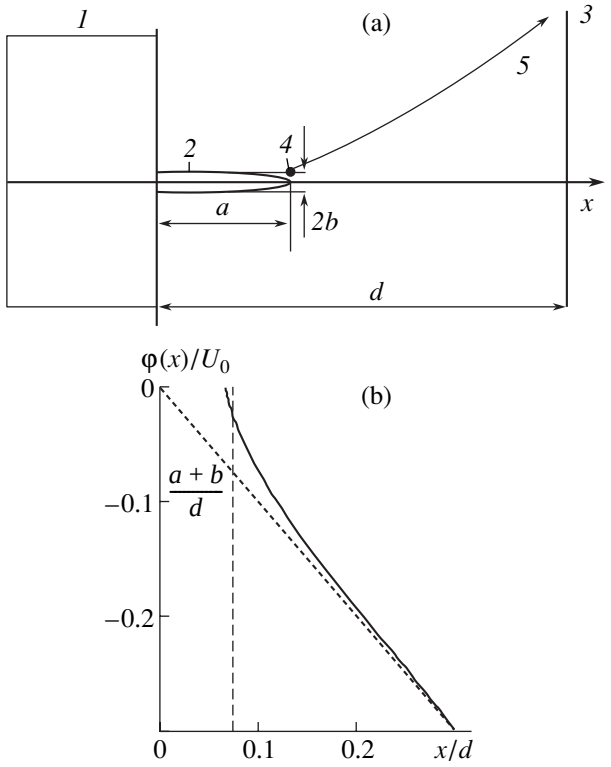

Fig. 2. Schematic diagrams showing (a) the model geometry and (b) the potential distribution as a function of the distance x measured from the cathode plane along the axis of the ellipsoid point (calculations performed for d = 28 mm, a = 1 mm, b = 0.5 mm): (*1*) cathode, $\varphi = 0$; (*2*) plasma, $\varphi = 0$; (*3*) anode, $\varphi = -U_0$; (*4*) region of electron acceleration; (*5*) fast electron trajectory.

(5 points/2 ns). The discharge was photographed using a digital camera.

Experimental results. The measurements of voltage pulses and discharge currents in the gas diode and observations of the discharge shape in the gap gave the following results.

For all gases studied in a broad range of experimental conditions, we observed a volume discharge between the sharp edge of the tube cathode and the plane anode, which had the form of diffuse cones or streamers (Fig. 1). The discharge remained diffuse at various pressures. Bright spots (corresponding to the voltage pulse front) were observed only at the cathode. It should be noted that the volume discharge could be observed both in the regime corresponding to the formation of an intense electron beam with an energy from tens to hundreds of kiloelectronvolts [5–8] and under the conditions when the electron beam was not detected behind the foil.

A decrease in the interelectrode gap width, a change in the cathode geometry, and variation of the gas pressure may lead to the appearance of separate channels (Fig. 1b) on the diffuse discharge background, while nonoptimum conditions (e.g., a small gap width) sometimes favor a transition to the spark regime. At an optimum gap width, an increase in the generator voltage also led to the appearance of bright channels in the volume discharge, while oscillograms reveal a decrease in the applied voltage. Figures 1e and 1f show the photographs of discharge in air, as viewed from the side (for the foil anode) and from the edge (via the grid anode). As can be seen, the discharge has the form of volume streamers originating from bright spots at the cathode.

The discharge current was detected at a very small delay (a fraction of a nanosecond) relative to the moment of voltage application to the discharge gap. The magnitude and duration of the discharge current in the case of a volume discharge depend on the generator characteristics, gap parameters, and the gas type and pressure. For example, generator 1 operating at an open circuit voltage of ~270 kV produced a discharge current with an amplitude of ~2400 A. In a discharge retaining the volume character for 3 ns, the current density at the anode reached up to 3 kA/cm^2, the specific energy deposited in the gas was about 1 J/cm^3, and the specific power supply was 400 MW/cm^3. At a volume discharge stage duration of 5 ns, the anode current density was 1.5 kA/cm^2, the specific power supply was 200 MW/cm^3, and the specific energy deposited in the gas remained equal to ~1 J/cm^3. Under the experimental conditions studied, we also observed a self-sustained discharge in which the interelectrode voltage is maximum in the quasi-stationary stage (which is indicative of a high electron density in the gap during the voltage pulse front).

Analysis of experimental results. Let us consider a solution of the well-known electrostatic problem concerning the potential distribution between a plane anode and the cathode featuring a conducting protrusion (point) having the shape of half an elongated ellipsoid of revolution with the axis perpendicular to the

electrode planes (Fig. 2a) [13]. In this case, the potential distribution is described by the function

$$\varphi(\xi, \zeta) = -\frac{U_0}{d}x(\xi, \zeta)\left\{1 - \left(\ln\left(\frac{1+\varepsilon}{1-\varepsilon}\right) - 2\varepsilon\right)^{-1} \times \left[\ln\left(\frac{\sqrt{1+\xi/a^2}+\varepsilon}{\sqrt{1-\xi/a^2}-\varepsilon}\right) - \frac{2\varepsilon}{\sqrt{1+\xi/a^2}}\right]\right\},$$

where (ξ, ζ) are the parabolic coordinates, U_0 is the potential difference between the plane electrodes, $x = (\xi, \zeta) = (a/\varepsilon)\sqrt{(1+\xi/a^2)(1+\zeta/a^2)}$ is the coordinate along the field, $\varepsilon = \sqrt{1-(b/a)^2}$ is the eccentricity of the ellipsoid, and a and b are its major and minor semiaxes, respectively. This solution is valid for $d - a \gg b$.

Based on the exact solution (Fig. 2b), we can derive the following conclusion. The potential at the point falls over a distance on the order of the radius of curvature (~b). However, the value of this potential drop is determined by the distance from the point tip to cathode (a), rather than by the curvature: $\varphi(a+b) = -U_0(a+b)/d$. Indeed, as the curvature radius tends to zero, the field strength tends to infinity, but the potential drop remains finite: $\varphi(a) = -U_0(a)/d$. This value depends on how far the point tip protrudes (i.e., spaced from the cathode plane).

Let us make some estimates. As can be seen from the photographs (Fig. 1), the size of bright spots at the cathode surface approximately amounts to 1 mm. Assuming that the electron density at the cathode spot is high and this plasma behaves as a good conductor, while the conductivity of plasma around the cathode spots is small, we may believe that the potential distribution is close to that determined in the above model electrostatic problem.

Electrons emitted from the point, having traveled a distance of ~(2–3)b from the point tip, acquire an energy of $\varepsilon_e \approx eU_0a/d$. Shortly (0.5–1 ns) after the voltage pulse application to the interelectrode gap at a peak voltage of $U_0 \approx 100$ kV, the energy of fast electrons will amount to ~2–5 keV. The free path of electrons, $R = (\varepsilon_e/\varepsilon_i)l_i$, increases with ε_e according to a quadratic law (Fig. 3) and amounts to $R \sim 1$ cm for $\varepsilon_e \sim 4$ keV. Here, $\varepsilon_i = 46$ eV is the energy spent per ionization event (i.e., the energy of formation of the electron–ion pair), $l_i = 1/\sigma_i N \sim 0.1$ mm is the electron free path between ionization events, $\sigma_i(\varepsilon_e)$ is the ionization cross section, and $N \approx 2.4 \times 10^{19}$ cm^{-3} is the number density of particles.

According to our experimental data [9], the velocity of an avalanche generated by a fast electron at a given field strength (i.e., at a reduced field strength $E/p \approx U_0/dp \sim 100$ V/(cm Torr)) amounts to $v_d \approx 10^8$ cm/s. Accordingly, the avalanches generated by a fast electron moving directly toward the anode will overlap over a period of time equal to $l_i/v_d \approx 0.1$ ns. This electron will reach the cathode within ~0.5 ns.

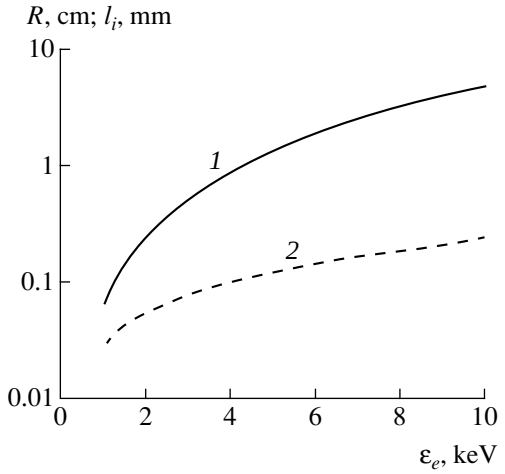

Fig. 3. Plots of (*1*) the electron free path R and (*2*) distance between ionization events l_i versus electron energy ε_e for helium, calculated using the approximation of $\sigma_i(\varepsilon_e)$ from [9].

Of course, electrons acquiring large energies near the protrusion move along curvilinear trajectories. The electric field orientation near the point tip provides for a nearly isotropic emission of electrons in the half-space between the cathode point tip and anode. However, the field drives electrons back to the anode. The sources of numerous overlapping trajectories are in the separate plasma formations at the cathode (Fig. 1). The effect of field screening over a considerable part of the volume takes place when the electron density increases (due the avalanche multiplication) to a critical level of $N_{e.cr} = U_0/4\pi ed^2 \sim 10^{10}$ cm^{-3}.

Conclusions. The obtained experimental data lead to the conclusion that the volume discharge in a pulsed inhomogeneous electric field [7] is formed due to the gas preionization with fast electrons. Fast (keV-energy) electrons appearing at the cathode are accelerated in a strong electric field at the cathode plasma formations. Using a high-pressure volume discharge without an additional preionization source, we achieved a specific power supply of up to 400 MW/cm^3, a discharge current density at the anode up to 3 kA/cm^2, and a specific energy deposited (within 3–5 ns) in the gas up to 1 J/cm^3.

A quasi-stationary stage of the volume discharge is attained at lower values of the initial voltage, which also confirms the formation of a large number of fast electrons.

Acknowledgments. The authors gratefully acknowledge the support from International Scientific-Technological Center, project no. 1270.

REFERENCES

1. Yu. D. Korolev and G. A. Mesyats, *The Physics of Pulse Breakdown in Gases* (Nauka, Moscow, 1991).
2. G. A. Mesyats, V. V. Osipov, and V. F. Tarasenko, *Pulsed Gas Lasers* (Nauka, Moscow, 1991; Opt. Eng., Bellingham, 1995).
3. L. V. Tarasova and L. N. Khudyakova, Zh. Tekh. Fiz. **39**, 1530 (1969) [Sov. Phys. Tech. Phys. **14**, 1148 (1969)].
4. L. P. Babich, T. V. Loĭko, and V. A. Tsukerman, Usp. Fiz. Nauk **160** (7), 49 (1990) [Sov. Phys. Usp. **33**, 521 (1990)].
5. S. B. Alekseev, V. M. Orlovskiĭ, and V. F. Tarasenko, Pis'ma Zh. Tekh. Fiz. **29** (10), 29 (2003) [Tech. Phys. Lett. **29**, 411 (2003)].
6. S. B. Alekseev, V. M. Orlovskiĭ, V. F. Tarasenko, *et al.*, Pis'ma Zh. Tekh. Fiz. **29** (16), 45 (2003) [Tech. Phys. Lett. **29**, 679 (2003)].
7. V. F. Tarasenko, V. M. Orlovskiĭ, and S. A. Shunaĭlov, Izv. Vyssh. Uchebn. Zaved., Fiz. **46** (3), 94 (2003).
8. V. F. Tarasenko, S. I. Yakovlenko, V. M. Orlovskiĭ, *et al.*, Pis'ma Zh. Éksp. Teor. Fiz. **77**, 737 (2003) [JETP Lett. **77**, 611 (2003)].
9. A. N. Tkachev and S. I. Yakovlenko, Pis'ma Zh. Éksp. Teor. Fiz. **77**, 264 (2003) [JETP Lett. **77**, 221 (2003)].
10. A. N. Tkachev and S. I. Yakovlenko, Pis'ma Zh. Tekh. Fiz. **29** (16), 54 (2003) [Tech. Phys. Lett. **29**, 683 (2003)].
11. M. I. Yalandin and V. G. Shpak, Prib. Tekh. Éksp., No. 3, 5 (2001).
12. F. Ya. Zagulov, A. S. Kotov, V. G. Shpak, *et al.*, Prib. Tekh. Éksp., No. 2, 146 (1989).
13. V. V. Batygin and I. N. Toptygin, *Problems in Electrodynamics* (Fizmatgiz, Moscow, 1962; Academic Press, London, 1964).

Translated by P. Pozdeev

Technical Physics Letters, Vol. 30, No. 5, 2004, pp. 415–417. Translated from Pis'ma v Zhurnal Tekhnicheskoĭ Fiziki, Vol. 30, No. 10, 2004, pp. 39–45.

The DD Reaction Yield in the Course of Dielectric Breakdown of Cavitation Bubbles in Dielectric Deuterated Liquids

A. G. Lipson[a], V. A. Kuznetsov[a], and G. H. Miley[b]

[a] *Institute of Physical Chemistry, Russian Academy of Sciences, Moscow, 117915 Russia*

[b] *Department of Nuclear, Plasma, and Radiological Engineering, University of Illinois at Urbana–Champaign, Urbana (IL) 61801, USA*

Revised manuscript received September 11, 2003

Abstract—The emission of neutrons observed during cavitation in dielectric deuterated liquids (C_3D_6O, D_2O) can be semiquantitatively explained within the framework of a proposed acceleration model. This model assumes the appearance of uncompensated charge on the walls of a cavitation bubble, which leads to spark discharge when the bubble reaches a maximum radius. © *2004 MAIK "Nauka/Interperiodica".*

Recently, Taleyarkhan *et al.* [1] published contradictory data on the emission of neutrons and tritium upon the formation and collapse of cavitation bubbles of a large size (r_{max}) in the course of sonoluminescence (SL) in deuterated acetone (C_3D_6O). It should be noted that the neutron yield was originally observed (albeit at a lower intensity) twelve years earlier [2, 3] during a multibubble cavitation induced in D_2O with a titanium vibrator. In contrast to the latter communications, it is ascertained in [1] that, according to the results of calculations, the temperature in collapsing cavitation bubbles (initiated by seeding 14-MeV neutrons in the acoustic field) reached $T \sim 10^7$ K. On this ground, the detected DD reaction products were considered as indicative of nuclear fusion reactions induced by cavitation in deuterated acetone.

Below, we will demonstrate that, within the framework of electric breakdown in cavitation bubbles of a large radius ($r_{max} \sim 1$ mm) in strongly deuterated liquids, one can expect a detectable neutron yield strongly dependent on the maximum bubble size.

Let us proceed from the commonly accepted notion (by analogy with breakdown in solid dielectrics and semiconductors [4]) that the formation of cavitation bubbles (leading to violation of the continuity of a dielectric liquid) is accompanied by electric charging of the bubble walls, whereby the surface acquires uncompensated electric charge. Indeed, the electric conductivity of liquid acetone $\gamma = 6 \times 10^{-8}\ \Omega^{-1}\ cm^{-1}$ at $T = 0°C$ (at $T = 22°C$, γ is about ten times as high) is comparable with that of molecular crystals, the cohesive fracture of which leads to the formation of a mosaic charge with a surface density of 10^{10}–10^{11} electron/cm^2. According to estimates [5], an analogous surface charge density is formed in the course of multibubble cavitation in water.

We will consider the simplest model in which the bottom half of a bubble bears a positive charge and the upper half has a negative charge. In the initial stage of bubble expansion immediately upon formation ($r \geq r_0 = r_{min}$), the pressure inside the bubble is high ($p \sim 10^3$ bar, $T > 10^3$ K). This prevents a gas breakdown inside the bubble on the one hand, and favors rapid charge relaxation on the bubble walls (as a result of a sharp increase in their conductivity at high temperatures) on the other hand. In addition, small spacing of the oppositely charged surfaces hinders the development of cascade processes leading to the spark discharge. Only when $r \longrightarrow r_{max}$, whereby the pressure and temperature in the bubble approach normal ($p \sim 1$ bar, $T = 300$ K), are the conditions of gas (C_3D_6O vapor) breakdown in the bubble realized. It should be noted that analogous breakdown upon breakage of adhesive (cohesive) bonds is observed in solid dielectrics [4].

Since the electrical strength of acetone vapor is 98% of the value for gaseous nitrogen (or air) [6], the electric field strength for the spark breakdown in the bubble is expediently evaluated using the well-known relation for the breakdown in air ($p = 1$ bar) described by the function $E(h)$, where h is the interelectrode distance (for a bubble, $h = 2r_{max}$). Therefore, the maximum energy of positively charged deuterons bombarding the negatively charge wall of the bubble is $E_d = 2Er_{max}$.

As can be seen from Fig. 1, the energies E_d of deuterons accelerated in the spark discharge in bubbles with $r = 0.1$–1.0 mm fall within the interval from 1.8 to 8.9 keV. The number N_d of such deuterons accelerated during the discharge in a single bubble can be estimated as

$$N_d = 4\pi\alpha_i N_L r_{max}^3, \quad (1)$$

1063-7850/04/3005-0415$26.00 © 2004 MAIK "Nauka/Interperiodica"

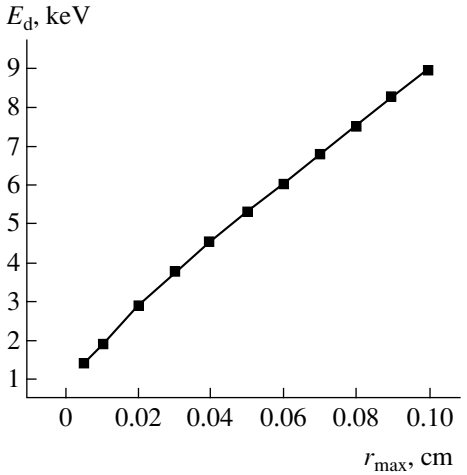

Fig. 1. A plot of maximum deuteron energy versus maximum radius of cavitation bubbles in deuterated acetone constructed using formula (1) and the Paschen law of breakdown in air at $p = 1$ bar [13].

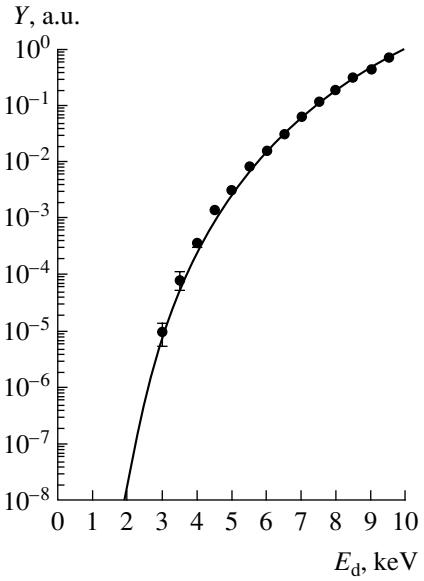

Fig. 2. A plot of the normalized DD reaction yield for a thick target versus the energy of bombarding deuterons (solid curve) constructed according to formula (4) using the Bosch–Halle approximation in the absence of DD reaction enhancement (bare yield); black circles represent experimental data on the $D(d, p)T$ reaction yield from Au target in an accelerator.

where α_i is the degree of ionization of deuterium in the spark discharge at $p = 1$ bar (estimates give $\alpha_i = 2.6 \times 10^{-5}$ [6]) and n_L is the Loschmidt number.

Within the framework of the acceleration model assuming bombardment of the bubble walls by deuterons with the energy E_d from the spark discharge, the total yield of neutrons during cavitation can be expressed as

$$Y_n = N_b N_d \omega_s Y(E_d), \quad (2)$$

where $N_b = 10^3$ is the number of cavitation bubbles in the resonator, $\omega_s = 1.9 \times 10^4$ Hz is the sound frequency [1], and $Y(E_d)$ is the DD reaction yield from a thick target in the course of the wall bombardment by deuterons. For deuterons with the energy E_d, the latter value is determined as [7]

$$Y(E_d) = \int_0^{E_d} N_D \sigma(E_d)(dE/dx)^{-1} dE,$$

where $N_d = 6.4 \times 10^{22}$ cm^{-3} is the concentration of deuterium in C_3D_6O, $\sigma(E_d)$ is the DD reaction cross section as a function of E_d [7], and dE/dx is the drag of deuterons in acetone ($dE/dx \sim v_d$, where v_d is the deuteron velocity [8]). Data on dE/dx in acetone are not available, but we may use in the first approximation the value for metallic $_3Li^7$ [9], since the effective average charge 3 and density ($\rho = 0.87$ g/cm^3) of C_3D_6O almost coincide with the values for metallic Li^7. Note also that $Y(E_d)$ at low energies is approximately described by the known Bosch–Halle relation (Fig. 2) [10].

Thus, using the model of spark discharge in the gap between charged bubble walls, the total yield of neutrons due to cavitation in C_3D_6O under the conditions studied in [1] can be estimated as

$$Y_n = 8\pi\alpha_i n_L N_b \omega_s r_{max}^3 \int_0^{E_d} N_D \sigma(E_d)(dE/dx)^{-1} dE. \quad (3)$$

As can be seen from Fig. 3 constructed for $r_{max} = 0.3$–1.0 mm [1] and $E_d \sim 3.7$–8.8 keV (Fig. 1), the neutron yield Y_n occurs within an interval of $\sim 10^2$–10^7 n/s (for a 4π solid angle), which satisfactorily agrees with the experimental data [1, 11]. As the maximum bubble radius decreases to $r_{max} < 0.01$ cm, the neutron yield sharply drops below the detection level. It should be noted that Y_n was evaluated using the Bosch–Halle approximation for the DD reaction cross section, with neglect of the DD yield enhancement typical of most metals bombarded with low-energy deuterons [12, 13].

The effect of enhanced yield (screening) probably takes place in the course of multibubble cavitation with a titanium vibrator used in the original study [2]. In that experiment, the cavitation bubbles interacted with the surface of a TiD_2 vibrator, which induced a discharge between the bubble wall and the metal surface. It was suggested that the maximum bubble radius in the case of multibubble cavitation with a vibrator is small, falling within 50–100 μm [5]. According to Fig. 1, the energies of deuterons accelerated in the spark discharge between a positively charged bubble wall and Ti surface are $E_d = 1.30$–1.84 keV. According to estimates [5], the number of bubbles supplied per unit time to the vibrator

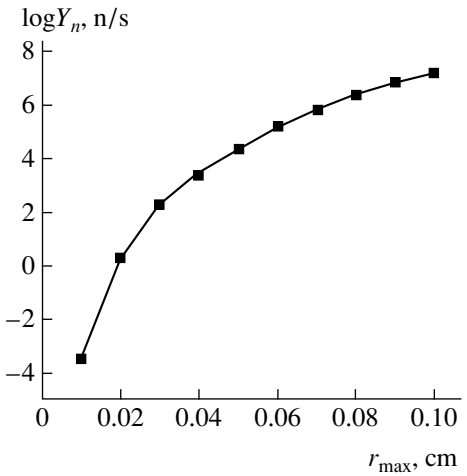

Fig. 3. A plot of the logarithmic neutron yield (for a 4π solid angle) calculated by formula (5) as a function of the maximum radius of cavitation bubbles in deuterated acetone under the conditions studied in [1].

during multibubble cavitation is $N_b \sim 10^6$ s^{-1} and the concentration of deuterium in the target (TiD_2 [3]) is $N_D = 1.13 \times 10^{23}$ cm^{-3}. With allowance for the DD reaction enhancement, $f_{DD} \sim 5 \times 10^2$–$1 \times 10^5$ characteristic of the Ti targets bombarded in glow discharge at $(E_d)_{lab}$ between 1.8 and 1.3 keV [14], we obtain Y_n = 0.2–8.0 n/s (for a 4π solid angle). This estimate satisfactorily agrees with the experimental data (0.5–1.0 n/s) [2, 3].

Thus, we have demonstrated that neutron emission in dielectric deuterated liquids (C_3D_6O, D_2O) can be, in principle, explained within the framework of the acceleration model. It is expected that the neutron yield must be strongly dependent on the bubble radius (i.e., controlled by the acoustic pressure amplitude). It should be noted that further increase in the bubble size (r_{max} > 0.1 cm) in C_3D_6O will probably not lead to additional growth in the neutron yield, which can be hindered either by increasing probability of earlier discharge (e.g., due to asymmetric bubble shape [15]) or by charge leakage.

In the case of multibubble cavitation with a Ti vibrator [2, 3], the observation of a weak neutron emission even for $r_{max} < 0.01$ cm becomes possible due to the DD reaction yield enhancement in metallic targets bombarded with low-energy deuterons [12–14].

Acknowledgments. The authors are grateful to Prof. K. Suslick for fruitful discussions.

REFERENCES

1. R. P. Taleyarkhan *et al.*, Science **295**, 1868 (2002).
2. A. G. Lipson, V. A. Klyuev, B. V. Deryaguin, *et al.*, Pis'ma Zh. Tekh. Fiz. **16** (9), 89 (1990) [Sov. Tech. Phys. Lett. **16**, 763 (1990)].
3. A. G. Lipson, B. F. Lyakhov, E. I. Saunin, *et al.*, Zh. Tekh. Fiz. **63** (7), 187 (1993) [Tech. Phys. **38**, 623 (1993)].
4. B. V. Deryagin, N. A. Krotova, and V. P. Smilga, *Adhesion of Solids* (Nauka, Moscow, 1977).
5. M. A. Margulis, *Sound-Chemical Reactions and Sonoluminescence* (Khimiya, Moscow, 1986).
6. N. A. Kaptsov, *Electrical Phenomena in Gas and Vacuum* (GITTL, Moscow, 1950).
7. H. Yuki, T. Sato, J. Kasagi, *et al.*, J. Phys. G **23**, 23 (1997).
8. K. Eder, D. Semrad, P. Bauer, *et al.*, Phys. Rev. Lett. **79**, 4112 (1997).
9. H. H. Anderson and J. F. Ziegler, *Hydrogen Stopping Powers and Ranges in All Elements* (Pergamon, New York, 1977).
10. Y. S. Bosch and G. M. Halle, Nucl. Fusion **32**, 611 (1994).
11. D. Shapira and M. Saltmarsh, Phys. Rev. Lett. **89**, 104302 (2002).
12. H. Yuki, G. Kasagi, A. G. Lipson, *et al.*, Pis'ma Zh. Éksp. Teor. Fiz. **68**, 785 (1998) [JETP Lett. **68**, 823 (1998)].
13. F. Raiola, P. Migliardi, G. Gyurky, *et al.*, Eur. Phys. J. A **13**, 377 (2002).
14. G. H. Miley and A. G. Lipson, in *Proceedings of the 11th International Conference on Emerging Nuclear Energy Systems, Albuquerque, 2002*, pp. 382–387.
15. Yu. T. Didenko and K. S. Suslick, Nature **418**, 394 (2002).

Translated by P. Pozdeev

Technical Physics Letters, Vol. 30, No. 5, 2004, pp. 418–421. Translated from Pis'ma v Zhurnal Tekhnicheskoĭ Fiziki, Vol. 30, No. 10, 2004, pp. 46–52.

Thermocapillary Deformation of a Locally Heated Liquid Film Moving under the Action of a Gas Flow

E. Ya. Gatapova, O. A. Kabov, and I. V. Marchuk

Kutateladze Institute of Thermophysics, Siberian Division, Russian Academy of Sciences, Novosibirsk, Russia
e-mail: gatapova@ngs.ru; marchuk@itp.nsc.ru; okabov@ulb.ac.be

Received October 17, 2003

Abstract—We propose a two-dimensional model of a steady laminar flow of a liquid film in a channel in the presence of a cocurrent gas flow. An analytical solution for the problem of temperature distribution is obtained for a linear flow velocity profile. The linearized problem of thermocapillary deformation of the film surface caused by local heating at a constant heat flux is solved. It is established that a thermocapillary bump is formed in the region where a thermal boundary layer emerges on the film surface. Additional perturbations, decaying in the upstream direction, can be present on the free surface in front of the bump. A criterion determining this effect is found. *© 2004 MAIK "Nauka/Interperiodica".*

Introduction. The development of microelectronics and, in particular, computer technologies, encounter the problem of thermal stabilization. A promising solution is offered by systems in which heat is transferred from integrations to a thin liquid film flowing in narrow channels under the action of a cocurrent gas flow. The laws of heat exchange and hydrodynamics in such a system were studied in [1] for the cocurrent flows of nitrogen and a cooling fluid (FC-72) in a 0.508-mm-high symmetrically heated channel. The description of stability of the joint motion of a nonisothermal liquid film and a gas is a complicated problem, which has not yet been exhaustively studied [2, 3]. The tangential and normal stresses induced by the gas flow and by thermocapillary forces at the gas–liquid interface give rise to nonlinear deformations, which can significantly influence the heat exchange and may cause breakdown of the liquid film.

This Letter presents the results of investigation of the flow hydrodynamics and heat exchange in a locally heated liquid film moving in a flat channel with cocurrent gas flow under conditions of determining influence of thermocapillary forces.

Formulation of the problem. Let us consider a channel with rectangular cross section in which a layer of viscous incompressible liquid flows under the action of a tangential stress τ induced by a cocurrent gas flow and under the action of gravity when the channel is inclined at an angle φ with respect to the horizontal plane. There is a heat exchange between the liquid and a local source (heater) situated in the substrate (bottom) of the channel. Speaking of "local" heating, we imply that the heat flux density on the bottom surface is a finite function of the coordinate x measured along the channel. We use a Cartesian coordinate system (x, y) with the Oy axis perpendicular to the substrate, the Ox directed along the flow, and the origin placed at the front edge of the heat source. The liquid is characterized by the temperature-dependent surface tension $\sigma = \sigma_0 - \sigma_T(T - T_0)$, where $\sigma_0 > 0$ and $\sigma_T > 0$.

A stationary two-dimensional flow of the liquid film is described by the Navier–Stokes and the energy transfer equations with the boundary conditions corresponding to the wall adherence $u(x, 0) = v(x, 0) = 0$, the local heat source with a constant heat flux density $-\lambda T_y(x, 0) = q_0(\chi(x) - \chi(x - L))$, the kinematic condition $h_x = v(x, h(x))/u(x, h(x))$, the force balance at the interface

$$p - p_a = -\sigma h_{xx}/(1 + h_x^2)^{3/2} + 2\mu(v_y - h_x(u_y + v_x) + h_x^2 u_x)/(1 + h_x^2),$$

$$\mu(2h_x(v_y - u_x) + (1 - h_x^2)(v_x + u_y))/(1 + h_x^2) + \sigma_T T_t - \tau = 0,$$

the heat exchange at the film surface $-\lambda T_n(x, h(x)) = \alpha(T(x, h(x)) - T_a)$, and the initial temperature of the isothermal film $T(-\infty, y) = T_0$. Here, L is the heater length, $\chi(x)$ is the Heaviside function, h is the liquid film thickness, p is the pressure in the liquid, p_a = const is the gas pressure, α is the coefficient of heat transfer at the film surface, T_a = const is the gas temperature, T_0 = const is the initial temperature of the film, and **t** and **n** are the unit vectors in the tangential and normal directions, respectively.

1063-7850/04/3005-0418$26.00 © 2004 MAIK "Nauka/Interperiodica"

Let the constant tangential stress τ and the initial film thickness h_0 be known. We assume the thin layer approximation is valid, that is, $\varepsilon = h_0/L \ll 1$. Below we use the dimensionless variables defined as

$$X = x/L, \quad Y = y/h_0, \quad U = u/\bar{u},$$
$$V = v/\bar{v}, \quad \theta = (T - T_0)/\Delta T,$$

$$\theta_a = (T_a - T_0)/\Delta T, \quad \bar{\theta} = (T(x, h(x)) - T_0)/\Delta T,$$
$$P = (p - p_a)/p_0,$$

$$T = \frac{\tau}{\tau_0}, \quad \bar{h} = \frac{h}{h_0}, \quad \Delta T = \frac{q_0 L}{c_p \Gamma}, \quad p_0 = \frac{\mu \bar{u}}{\varepsilon h_0},$$
$$\tau_0 = \frac{\mu \bar{u}}{h_0}, \quad Ma = \frac{\varepsilon \sigma_T \Delta T}{\mu \bar{u}},$$

$$\bar{u} = \frac{1}{h_0}\int_0^{h_0} u(y)dy, \quad \bar{v} = \varepsilon \bar{u}, \quad C = \frac{\bar{u}\mu}{\sigma_0}\varepsilon^{-3}.$$

Here, Ma is the Marangoni number, C is the analog of the capillary number ($C = 0$ (1) as $\varepsilon \longrightarrow 0$), and Γ is the specific flow rate of the liquid. For a linear flow velocity profile in the film, the average velocity is expressed via the tangential stress as $\bar{u} = \tau h_0/2\mu$ and the dimensionless tangential tension is $T = \tau/\tau_0 = 2$.

Temperature distribution in a locally heated film. Consider the problem of heat transfer for a rigid film ($h = h_0 = \text{const}$) and linear velocity profile with $v = 0$. Denoting $\eta(X) = \chi(X) - \chi(X - 1)$ and using the method indicated in [4], we obtain the following solution to the problem of temperature distribution:

$$\theta(X, Y) = \left(1 + \frac{1}{Bi} - Y\right)\varepsilon\frac{c_p\Gamma}{\lambda}\eta(X) + \theta_a$$
$$+ \sum_{i=1}^{\infty} G_i \psi_i(Y) \exp(-\xi_i^2 X)\frac{1}{\xi_i^2}\left[Bi\theta_a\psi_i(1)\right. \qquad (1)$$
$$\left. - \varepsilon\frac{c_p\Gamma}{\lambda}\psi_i(0)\left(\eta(0) + \int_0^X \exp(\xi_i^2 X)\frac{\partial\eta(X)}{\partial X}dX\right)\right],$$

where $Bi = \alpha h_0/\lambda$ is the Biot number; $\psi_i(Y) = \sqrt{Y}\,J_{-1/3}\left(\frac{2}{3}\sqrt{2\varepsilon Pe}\,\xi_i Y^{3/2}\right)$ and ξ_i ($i = 1, \ldots, \infty$) are the eigenfunctions and eigenvalues of the Sturm–Liouville problem; and $J_\nu(\xi)$ is the Bessel function of the first kind. The coefficients G_i are determined from the condition of orthogonality of the eigenfunctions. Note that solution (1) is valid for any function η possessing an integrable generalized derivative.

A solution to linearized equation for the film thickness. A nonzero temperature gradient on the film surface gives rise to the thermocapillary effect, while a tangential stress deforms the film. If the temperature distribution over the film surface is known—for example, from the analytical solution or from experimental data—the magnitude of these surface deformations can be determined as follows. Using the Navier–Stokes equations, the conditions of continuity, and the boundary conditions, we obtain the following equation for the film thickness in a dimensionless form:

$$\frac{\bar{h}^3}{3}\left(\varepsilon C^{-1}\bar{h}_{XXX} - \varepsilon\frac{\rho g h_0}{p_0}\cos\varphi\,\bar{h}_X + \frac{\rho g h_0}{p_0}\sin\varphi\right)$$
$$+ \frac{\bar{h}^2}{2}\varepsilon(T - Ma\bar{\theta}_X) = \varepsilon\gamma, \qquad (2)$$

where γ is the dimensionless flow rate.

Let us assume that $\bar{h}(X) = 1 + h_1(X)$, where $|h_1| \ll 1$. Linearizing Eq. (2) and neglecting the term $\varepsilon h_1 Ma\bar{\theta}_X = O(\varepsilon^3)$ in the left-hand part (i.e., assuming that the thermocapillary tangential stress is significantly smaller than the tangential stress ($Ma \ll 1$) caused by the gas flow), we arrive at the following linear equation,

$$h_{1XXX} - C\frac{\rho g h_0}{p_0}\cos\varphi\,h_{1X}$$
$$+ 3C\left(T + \frac{\rho g h_0}{\varepsilon p_0}\sin\varphi\right)h_1 = f(X), \qquad (3)$$

where $f(X) = 3C(\gamma - T/2 + Ma\bar{\theta}_X/2) - \rho g h_0 C\sin\varphi/\varepsilon p_0$. Note that we cannot ignore the thermocapillary forces in the right-hand part, where this term is of a lower order of smallness: $\varepsilon Ma\bar{\theta}_X/2 = O(\varepsilon^2)$. For a horizontal channel, we have $\gamma = 1$, $T = 2$, and Eq. (3) simplifies to

$$h_{1XXX} - C\rho g h_0 h_{1X}/p_0 + 3CTh_1 = 3CMa\bar{\theta}_X/2.$$

A solution to Eq. (3) is given by a convolution of the functions $F(X)$ and f [5],

$$h_1(X) = \int_{-\infty}^{\infty} F(X - \xi) f(\xi) d\xi,$$

where $F(X)$ is the fundamental solution of the corresponding homogeneous equation. The form of the fundamental solution depends on the sign of the discriminant D of the characteristic polynomial. If $D > 0$, the latter polynomial has a single real root and two conjugated complex roots; therefore, the fundamental solu-

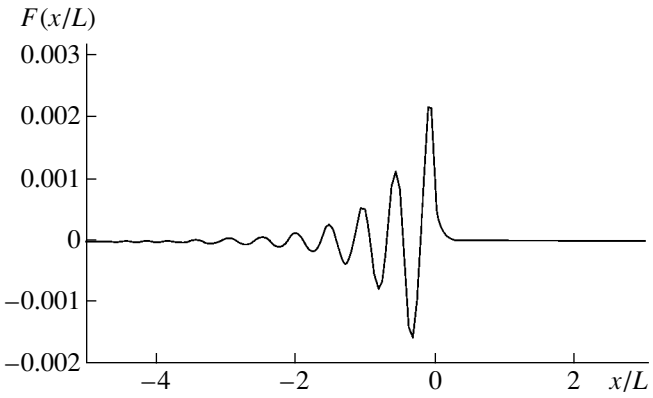

Fig. 1. The fundamental solution calculated for FC-72 fluid at T_0 = 17°C, Re = 0.04, φ = 5°, and τ = 0.024 kg/(s^2 m).

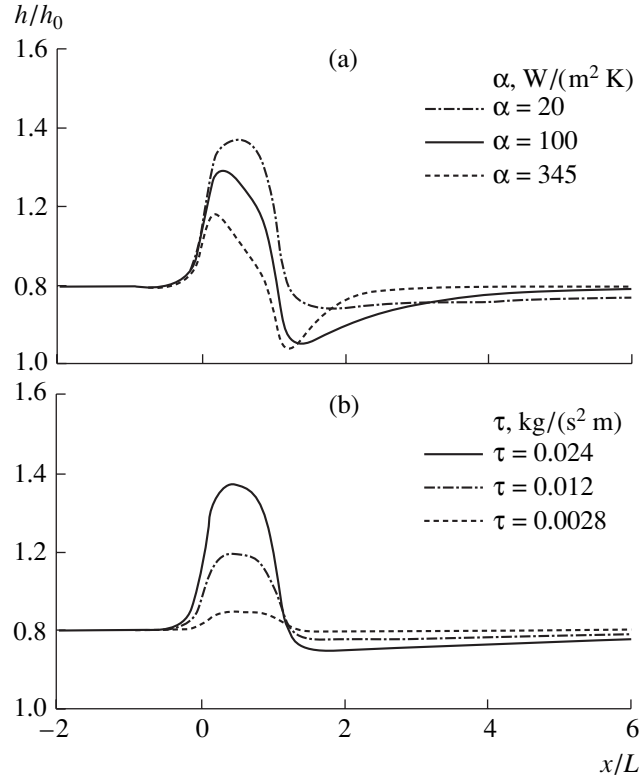

Fig. 2. Thermocapillary deformation of the free surface of FC-72 fluid at $T_a = T_0$ = 17°C, L = 6.7 mm, Re = 1, q = 1000 W/m^2, and φ = 0° (the heater is situated in the region between x/L = 0 and 1 on the abscissa axis): (a) film profiles for various heat-transfer coefficients α, h_0 = 0.00017 m, and τ = 0.024 kg/(s^2 m); (b) film profiles for various tangential stresses τ and α = 20 W/(m^2 K).

tion to the left of the origin is a periodic function. For D = 0, all roots are real and two of them coincide, and for D < 0, all roots are real and have different values. In the two last cases, the fundamental solution is not a periodic function.

For D > 0, we obtain

$$\tau + \rho g h_0 \sin\varphi > \rho g h_0 \frac{2}{3}\frac{h_0}{l_\sigma}\left(\frac{\cos\varphi}{3}\right)^{3/2}, \qquad (4)$$

where $l_\sigma = \sqrt{\sigma_0/\rho g}$ is the capillary length. In this case, the free surface of liquid exhibits a thermocapillary bump and may feature additional perturbations in front of the bump, decaying in the upstream direction. The decaying profile on the free surface is present when the forces driving the film are dominating over the hydrostatic forces. The perturbations will always be present at large channel inclination angles (φ = 90°). The capillary perturbations are more appreciable for small Reynolds numbers (Re = 0.04) and a relatively strong influence of the gas flow (Fig. 1). In the absence of gravity, the discriminant of the characteristic polynomial is positive and the fundamental solution acquires the form

$$F(X) = (\chi(X)\exp(-AX) + 2\chi(-X)\exp(AX/2) \times \cos(\pi/3 + \sqrt{3}AX/2))/3A^2,$$

where $A = (3CT)^{1/3}$. Perturbations of the free surface decaying in the upstream direction take place for any τ > 0.

Figure 2 shows variation of the relative film thickness along the channel. These profiles were calculated for various values of the heat-transfer coefficient and various tangential stresses. A positive temperature gradient in the region of the heater gives rise to a thermocapillary tangential stress directed toward the main flow. The film thickness in the region over the heater increases. Past the heater, the temperature decreases with the distance along the flow. In this region, the thermocapillary force is directed along the flow and the film thickness decreases relative to the initial value. A minimum film thickness corresponds to the maximum heat-transfer coefficient. The latter region is most dangerous from the standpoint of film breakdown. Note that surface perturbations decaying in the upstream direction are missing in Fig. 2 because condition (4) is not satisfied.

At a constant Re value, an increase in the tangential stress (corresponding to a growth in the gas flow rate) leads to a decrease in the initial film thickness, which enhances the thermocapillary effect. For a relatively high heat flux density on the heater and a weak heat transfer to the gas phase, calculations predicts the formation of a thermocapillary bump up to 30–50% of the initial film thickness. A bump on this order of magnitude was observed experimentally [6] and predicted theoretically [7] for a liquid film falling under the action of gravity over the surface of a vertical plate.

Acknowledgments. This study was supported by the Federal Program "Integration of Science and Higher School in Russia for 2002–2006" (project nos. I0734 and Ya0114) and the Russian Foundation for Basic Research (project no. 02-02-16478).

REFERENCES

1. A. Bar-Cohen, G. Sherwood, M. Hodes, and G. L. Solbreken, IEEE Trans. Compon., Packag. Manuf. Technol., Part A **18**, 502 (1995).
2. S. P. Aktershev and S. V. Alekseenko, Russ. J. Eng. Thermophys. **6**, 307 (1996).
3. O. A. Kabov, V. V. Kuznetsov, I. V. Marchuk, *et al.*, Poverkhnost, No. 9, 84 (2001).
4. M. D. Mikhailov, Int. J. Eng. Sci. A **10**, 577 (1972).
5. V. S. Vladimirov, *Equations of Mathematical Physics* (Nauka, Moscow, 1981; Dekker, New York, 1971).
6. O. A. Kabov, J.-C. Legros, I. V. Marchuk, and B. Sheid, Fluid Dynamics, No. 3, 521 (2001).
7. I. V. Marchuk and O. A. Kabov, Russ. J. Eng. Thermophys. **8**, 17 (1998).

Translated by P. Pozdeev

Technical Physics Letters, Vol. 30, No. 5, 2004, pp. 422–425. Translated from Pis'ma v Zhurnal Tekhnicheskoĭ Fiziki, Vol. 30, No. 10, 2004, pp. 53–60.

The Activation Law for One-Dimensional Maps

I. A. Khovanov*, D. V. Dumskiĭ, and N. A. Khovanova

Saratov State University, Saratov, Russia

** e-mail: igor@chaos.ssu.runnet.ru*

Received November 20, 2003

Abstract—The activation dynamics of one-dimensional maps is considered. It is shown that the activation law describing the average time required for attaining a given boundary has the form of the error function (erfc), whereas approximation using the exponential law gives much worse results. In addition, it is demonstrated that linear analysis can be applied to a substantially nonlinear problem. *© 2004 MAIK "Nauka/Interperiodica".*

Investigation of the breakdown of metastable states is among the basic problems encountered in many fields of science [1]. Here, by a metastable state is implied a stable state in the presence of fluctuations capable of inducing deviations from stability. This problem is closely related to that of determining the first time when the system trajectory attains a given boundary [1]. An answer to this question usually has the form of an activation law describing the rate of decay of the given metastable state (or the average time for attaining the boundary of the basin of attraction of the corresponding stable state) and the average time of attaining the boundary as functions of the noise level (or the temperature).

An archetype of the activation law is offered by the Arrhenius (exponential) law [1]

$$\langle \tau \rangle \propto \exp\left(\frac{E}{D}\right); \tag{1}$$

where $\langle \tau \rangle$ is the average time of the activation process, E is a quantity determining the activation energy frequently called potential barrier height (for potential systems) or quasi-potential height (for nonpotential systems) [2, 3], and D is the noise intensity or the temperature. The Arrhenius law is valid for a large variety of activation processes and deviation from this relation is considered as an anomaly, evidencing a complicated activation dynamics. This law underlies the construction of many theories describing noise-induced dynamics.

This Letter presents the results of a numerical study of the activation behavior of a one-dimensional map. It is shown that the activation law is well approximated by the error function (erfc), while the exponential approximation gives much worse results. In addition, the possibility of using a linearized map for the analysis of activation dynamics is considered.

For maps, as well as for the flow systems, an exponential activation law can be derived within the low-noise approximation. Various schemes of obtaining the exponential law are described in [4]. The most general approach is based on the construction of a quasi-potential of the given system and, in fact, makes use of the concept of least action or, in other words, the theory of large fluctuations [3, 4]. This very approach is employed below. The main idea of this study consists in a comparative analysis of the activation energy S, obtained by considering expanded maps (see below) within the framework of the theory of large fluctuations, and the energy E determined from a numerical calculation of the average time of attaining a boundary in the map with noise.

We consider the fluctuation dynamics of two one-dimensional maps arising in relation to the problem of stabilization of unstable orbits of a chaotic attractor in the logistic map [5]. The first map describes the procedure of stabilization of a fixed point x^* of period 1 using the Ott–Grebogi–Yorke (OGY) method [6] in the presence of Gaussian random forces ξ_n:

$$\begin{aligned} x_{n+1} &= (r + \Delta r_n)x_n(1 - x_n) + D\xi_n, \\ \Delta r_n &= r\frac{(2x^* - 1)(x_n - x^*)}{x^*(1 - x^*)}, \quad x^* = 1 - \frac{1}{r}. \end{aligned} \tag{2}$$

Here, D is the intensity of fluctuations; ξ_n is the Gaussian random process with zero average ($\langle \xi_n \rangle = 0$), delta-correlated autocorrelation function $\langle \xi_n \xi_{n+k} \rangle = \delta(k)$, and unit dispersion ($\langle \xi_n^2 \rangle = 1$); and Δr is the control perturbation of the parameter r.

The second map describes stabilization of the point x^* by the adaptive method (ADP) [7],

$$\begin{aligned} x_{n+1} &= rx_n(1 - x_n) + \Delta x_n + D\xi_n, \\ \Delta x_n &= (x_n - x^*), \quad x^* = 1 - \frac{1}{r}, \end{aligned} \tag{3}$$

where Δx is the control perturbation of the coordinate x.

1063-7850/04/3005-0422$26.00 © 2004 MAIK "Nauka/Interperiodica"

Let us fix the parameter $r = 3.8$. In what follows, systems (2) and (3) will be referred to as the OGY and ADP maps, respectively. Peculiarities of the deterministic dynamics of these systems were recently considered in [5]. It should be noted that fixed points x^* are attractors of maps (2) and (3). Their basins of attraction have different structures: the basin of x^* in the OGY map is fractal, while that in the ADP map is smooth. The ADP map has a single optimum path of escape from the basin of attraction of the fixed point, while the OGY map has several virtually equiprobable pathways for the escape [5]. Thus, we will study two maps with different structures of their phase spaces and different fluctuational dynamics.

First, let us consider the case for which the activation law in the form of the error function can be readily obtained. This situation corresponds to the problem concerning the escape of the system trajectory from a small ϵ vicinity ($\epsilon \ll 1$) of the fixed point of the OGY map. Since the vicinity is small, we can formally replace (2) by a linearized map

$$x_{n+1} = ax_n + D\xi_n, \tag{4}$$

where $a = (\partial x_{n+1}/\partial x_n)\big|_{x_n = x^*}$ is the derivative of the right- hand part of the map with respect to the variable. For the OGY map, the derivative a is zero. Therefore, the average time of attaining the boundary is completely determined by that for the Gaussian delta-correlated noise and, hence, can be expressed as

$$\langle \tau \rangle = \frac{1}{\operatorname{erfc}(\epsilon/\sqrt{2D})}, \tag{5}$$

where $\operatorname{erfc}(x) = (2\pi)^{-1/2}\int_x^\infty \exp(-y^2)dy$. Relation (5) corresponds to the inverse probability for the map to occur outside the interval $x^* \pm \epsilon$; the probability is determined based on the stationary Gaussian distribution for the random process ξ_n.

Figure 1 shows the logarithmic plots of $\langle \tau \rangle$ versus D calculated using formula (5) in comparison to the results of numerical simulation using map (2). In the latter case, we selected the initial conditions at the point x^* and determined the time for which the map escaped from the ϵ vicinity of this point. Then, the map was again placed at the initial point x^* and the time of attaining the boundary was determined once more, and so on. As a result, we obtained an array of times that was averaged to determine $\langle \tau \rangle$. Figure 1 shows that theoretical and simulated curves coincide. For comparison, the dashed line in Fig. 1 shows the approximation

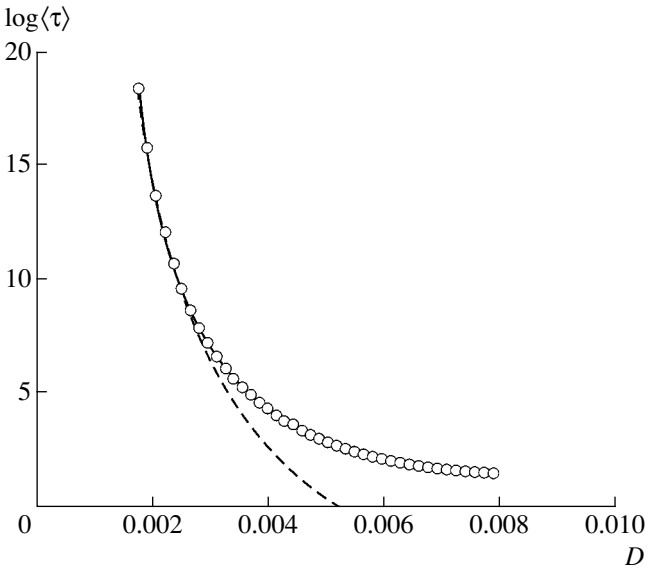

Fig. 1. The logarithmic plots of the average time $\langle \tau \rangle$ of attaining the boundaries $x^* \pm \epsilon$ versus the noise intensity D for the OGY map ($\epsilon = 0.01$): open circles represent the numerical simulation using map (2); solid line shows the results of calculation using formula (5); dashed line corresponds to the exponential approximation using formula (1).

constructed using formula (1). At a small intensity of noise, this approximation is satisfactory, but, as the noise intensity grows, the error exhibits a sharp increase. Thus, the approximation using the error function (erfc) gives the best result. In this function, the argument is a quantity proportional to the amplitude (rather than the energy). It should be noted that the calculated error dispersion between the results of numerical simulation and approximation (5) was close to zero.

Formula (5) was obtained by linearization of the initial map in the vicinity of the fixed point. As is known, the error of a linearization procedure is small if the function is close to a straight line. For the map (2) under consideration, however, the function $x_{n+1} = f(x_n)$ differs from a straight line in arbitrarily small ϵ vicinity of x^*, because this point is the maximum of a parabola. Thus, the linearization procedure has proved to be successful for a substantially nonlinear function. Then, an additional question arises concerning the size of this "linear" region, which will be considered below.

Going outside the framework of the linear approximation, we replace ϵ in formula (5) by $\sqrt{E}$ (E is the activation energy):

$$\langle \tau \rangle = \frac{C}{\operatorname{erfc}\left(\dfrac{\sqrt{E}}{\sqrt{2D}}\right)}. \tag{6}$$

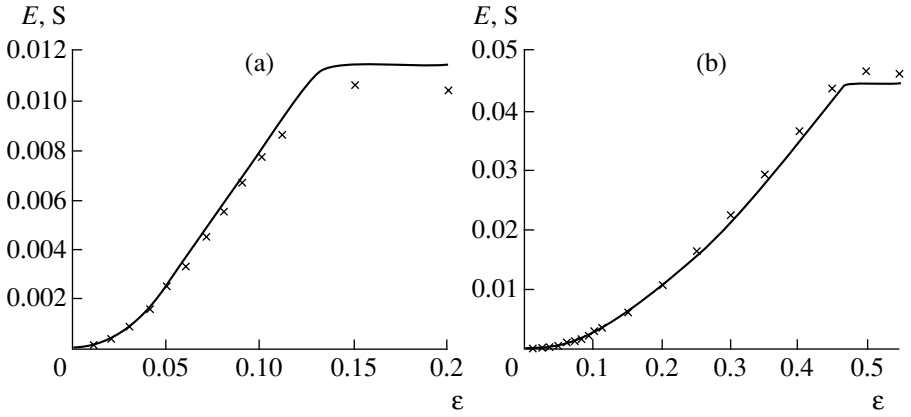

Fig. 2. Plots of the activation energy E (crosses) calculated using formula (6) and the quasi-potential S (solid line) determined by solving the boundary-value problem (7) versus the distance to the boundary $x^* \pm \epsilon$ for the (a) OGY and (b) ADP maps.

Let us study the possibility of evaluating the average time of attaining the boundary using approximation (6), where C is a certain preexponential factor. The investigation consists in determining the activation energy from a numerically calculated dependence of the average time of attaining the boundary, $\langle\tau\rangle$, on the noise intensity D. This energy is compared to the value obtained in the calculation of a quasi-potential $S(x)$ of the map. The quasi-potential can be determined by solving the boundary-value problem for the expansion of a map of the type [2, 3, 5]

$$\begin{aligned} x_{n+1} &= f(x_n) + y_n/g(x_n), \\ y_{n+1} &= y_n/g(x_n) \end{aligned} \tag{7}$$

with the initial condition at the point ($x_0 = x^*$, $y_0 = 0$) and the boundary conditions $x_k = x^* \pm \epsilon$, where k in the general case tends to infinity (but can remain finite).

Map (7) determines the fluctuational trajectories originating from the fixed point x^* and terminating at the boundary $x^* \pm \epsilon$. The coordinate y_n corresponds to the fluctuational force. Determining fluctuational trajectories is a boundary-value problem having, in the general case, an infinite number of solutions or none at all. The optimum paths are determined from the condition of minimum of the functional of action S corresponding to the activation energy,

$$S = \sum_{n=0}^{k} y_n^2, \tag{8}$$

where the y_n values are calculated along the fluctuational trajectories.

Figure 2 shows the results of calculations of the activation energy using approximation of the numerical dependence of $\langle\tau\rangle$ on D by formula (6) in comparison to the quasi-potential S. As can be seen, formula (6) provides for a good result for both OGY and ADP maps. The activation energy increases to reach saturation at a certain value of ϵ corresponding to the distance from x^* to the boundary of the basin of attraction. It should be noted that the same good coincidence can also be obtained by using an exponential approximation of the initial part of the dependence of $\langle\tau\rangle$ on D, because in the first order of expansion with respect to the small parameter, erfc is approximated by the exponential function. However, such an exponential approximation has a form different from relation (1):

$$\langle\tau\rangle \propto \exp\left(\frac{C_1\sqrt{E}}{D}\right), \tag{9}$$

where C_1 is a constant factor. Analogous results were obtained for the chaotic attractor: the average time of attaining the boundary of the basin of attraction is approximated by erfc.

Thus, we may ascertain that formula (6) describes the activation law for one-dimensional maps.

Let us return to the question concerning the maximum value of ϵ for which formula (5) remains valid. This maximum can be determined by studying the behavior of the preexponential factor C in formula (6): as long as this factor is close to unity, formula (5) will remain valid. Analysis of the behavior of $C(\epsilon)$ showed that the maximum size of the ϵ vicinity is 0.09, which is a rather large value. This result indicates that an analysis performed within the framework of the linear approach can provide good results for a substantially nonlinear problem.

In conclusion, it should be noted that the problem of theoretical justification of using formula (6) for description of the activation law is still open. Analysis of the behavior of the preexponential factor C and its relation to the type of map also remained outside the framework of this study. The above results can be used

for classification of the form of activation dynamics based on the experimental data.

Acknowledgments. This study was supported by the INTAS Foundation, grant no. 01-867.

REFERENCES

1. C. Gardiner, *Handbook of Stochastic Methods for Physics, Chemistry, and Natural Sciences* (Springer, Heidelberg, 1983; Mir, Moscow, 1986).
2. R. Graham and T. Tel, Phys. Rev. Lett. **66**, 3089 (1991).
3. P. Grassberger, J. Phys. A **22**, 3283 (1989).
4. P. D. Beale, Phys. Rev. A **40**, 3998 (1989); P. Reimann and P. Talkner, Phys. Rev. E **51**, 4105 (1995).
5. I. A. Khovanov, N. A. Khovanova, and P. V. E. McClintock, Phys. Rev. E **67**, 051102 (2003).
6. E. Ott, C. Grebogi, and J. Yorke, Phys. Rev. Lett. **64**, 1196 (1990).
7. S. Boccaletti, C. Grebogi, Y.-C. Lai, *et al.*, Phys. Rep. **329**, 103 (2000).

Translated by P. Pozdeev

Technical Physics Letters, Vol. 30, No. 5, 2004, pp. 426–428. Translated from Pis'ma v Zhurnal Tekhnicheskoĭ Fiziki, Vol. 30, No. 10, 2004, pp. 61–65.

The Anisotropic Effect of a Weak Magnetic Field on the Photoconductivity of C_{60} Single Crystals

Yu. I. Golovin, D. V. Lopatin*, R. K. Nikolaev, and A. V. Umrikhin

Tambov State University, Tambov, Russia

Institute of Solid State Physics, Russian Academy of Sciences, Chernogolovka, Moscow oblast, Russia

** e-mail: lopatin@tsu.tmb.ru*

Received May 13, 2003; in final form, December 17, 2003

Abstract—The effect of crystal orientation on the photogeneration of free charge carriers was studied for C_{60} single crystals in a weak magnetic field. The photoconductivity sharply depends on the orientation of magnetic field with respect to the crystallographic directions, showing a 5–8% increase for seven axes of the C_{60} crystal. *© 2004 MAIK "Nauka/Interperiodica".*

Fullerenes and their derivatives are considered as the base materials for advanced nanotechnologies and products for nanoelectronics, nanolithography [1], effective switching devices for liquid crystal structures [2], nanosensors [3], etc. Important for such applications, the electron-optical properties of molecular crystals are formed predominantly by the exciton states [4]. The photoexcitation of C_{60} molecules gives rise to Frenkel excitons (comprising electron and hole in the same molecule) and charge transfer (CT) excitons (a pair of opposite charges localized in different, most frequently adjacent, molecules) [5].

The role of the crystal field in the formation of electron-optical properties of C_{60} crystals is still insufficiently studied. It was found [6] that a magnetic field with an induction of $B < 1$ T effectively modifies the photoconductivity of fullerites, which is manifested by an up to 15% increase in the photocurrent I_f for fullerites exposed to the magnetic field. The magnetic field dependence of the photocurrent increment $\Delta I_f(B)$ exhibits saturation at $B_0 \sim 0.1$ T. It was demonstrated [6, 7] that the electron-optical properties of C_{60} single crystals can be controlled using the field-induced changes in the spin state of CT excitons.

The aim of this study was to elucidate the role of the crystal orientation in the process of free carrier photogeneration in C_{60} single crystals exposed to a magnetic field.

The experiments were performed on C_{60} single crystals of high-purity (99.95%) grown at the Institute of Solid State Physics (Chernogolovka). The samples selected for the experiments exhibited a regular faceting, which allowed the orientation of crystallographic planes in the fcc phase to be unambiguously determined. The photoconductivity was excited by the light of a xenon lamp (DKSSh-200). The photoconductivity excitation spectra were measured by passing the light through a large-aperture grating monochromator with a dispersion of 0.6 nm/mm. The photoconductivity was characterized by the photocurrent I_f measured using indium contacts glued with a silver paste to one of the crystal faces. The voltage applied between the contacts was varied within 20–40 V. In order to avoid photooxidation, the sample was placed in an evacuated and hermetically sealed quartz ampule. The constant magnetic field with an induction of 0.4 T was generated by an electromagnet.

Figure 1 shows the typical photoconductivity excitation spectrum of a C_{60} single crystal measured with and without an applied magnetic field. As can be seen,

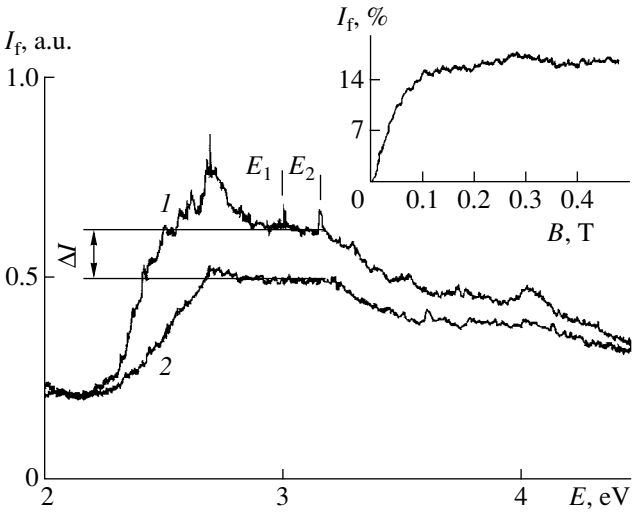

Fig. 1. The spectra of photoconductivity excitation in C_{60} single crystals measured (*2*) without and (*1*) with applied magnetic field ($B = 0.4$ T). The inset shows a plot of the photocurrent increment ΔI_f versus magnetic induction B (data from [6]).

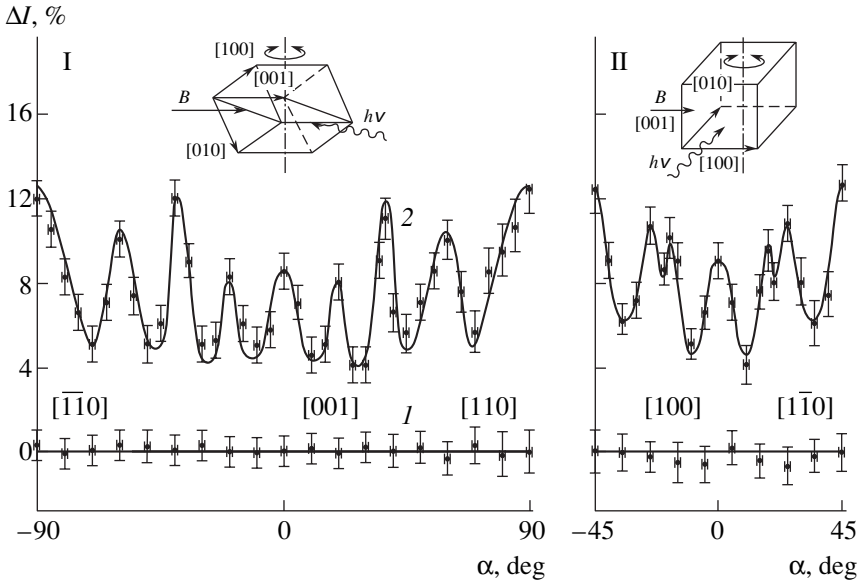

Fig. 2. Plots of the photocurrent increment ΔI versus angle of rotation α of the magnetic induction vector **B** relative to the crystallographic axes: (*1*) $B = 0$; (*2*) $B = 0.4$ T. The insets show the experimental geometry for (I) {110} plane and (II) {100} plane.

the photoconductivity exhibits a 5–15% increase in the magnetic field of $B = 0.4$ T in the photon energy interval from 2.5 to 4.5 eV. Expansion of the spectra into Lorentz components revealed, by analogy with [8], three optical transitions at photon energies of 2.64, 3.07, and 3.87 eV. Analysis of the spectra of C_{60} films showed that the transition at 3.07 eV can be assigned to a CT exciton [8]. In addition, exposure to the magnetic field gave rise to local photoconductivity peaks in C_{60} single crystals, observed at $E_1 = 2.91$ eV and $E_2 = 3.11$ eV, which have also been attributed to the CT excitons [7].

Subsequent experiments were devoted to the effect of magnetic field on the photoconductivity measured in a broad range of photon energies covering the entire exciton band of exciton generation (2.75–3.3 eV). In the course of rotation of the magnetic induction vector in the interval of angles from –90° to +90° about the $[1\bar{1}0]$ axis, we observed eight directions in which the photoconductivity exhibited a 5–8% increase as compared to the value measured without an applied field (Fig. 2). This pattern was mirror-symmetric relative to the [001] direction. When the magnetic induction vector was rotated in the interval of angles from –45° to +45° about the [001] axis, we observed six directions in which the photoconductivity exhibited a 6–8% increase.

Taking into account that the excitation of photoconductivity in our experiments was performed in the exciton band, it would be expedient to consider the mechanism of the anisotropic effect of the applied magnetic field assuming that the field affects the exciton mechanisms of free charge carrier production in the samples. This is confirmed by the fact that the photoconductivity excited in C_{60} single crystals by light with photon energies within 3.5–4.5 eV exhibited a constant increment independent of the magnetic field orientation relative to the crystallographic directions.

According to Kazaoui *et al.* [5], there are at least two significant CT exciton states in fullerites. The discovery of more than two directions featuring an increase in the photoconductivity allows us to suggest that there is a larger number of CT exciton states in the system studied. Analysis of the mutual orientation of the crystal axes and the magnetic induction vector showed that the photoconductivity increments were observed when the field vector coincided with the line connecting the centers of two adjacent C_{60} molecules in the fcc lattice. Assuming that each direction of the field-induced increase in the photoconductivity corresponds

The arrangement of electron and hole in the C_{60} crystal lattice for various CT exciton states

Plane	Position 1	Position 2	α, deg
{110}	(0, 0, 0)	(0, 0, 1)	0
	(0, 0, 0)	(1, 1, 2)	20
	(0, 0, 0)	(1/2, 1/2, 1)	38
	(0, 0, 0)	(1, 1, 1)	60
	(0, 0, 0)	(1/2, 1/2, 0)	90
{100}	(1/2, 0, 1/2)	$(2, \bar{1}/2, 1/2)$	18
	(0, 0, 0)	$(2, \bar{1}, 0)$	26

Note: Positions 1 and 2 correspond to the centers of molecules on which hole and electron are localized, respectively.

to a molecular excitation of its own and taking into account the equivalence of crystallographic directions, we may speak of seven CT exciton states (see table).

In conclusion, we have established that the photoconductivity of C_{60} single crystals is sensitive to the crystal orientation relative to the applied magnetic field. New CT exciton states have been found, which significantly influence the electron-optical properties of C_{60} single crystals.

Acknowledgments. This study was supported by the Russian Foundation for Basic Research (project nos. 02-02-17571 and 03-02-06181), the Federal Targeted Program "Fullerenes and Atomic Clusters," and the Program "Universities of Russia" (project no. UR.01.01.013).

REFERENCES

1. Yu. A. Ossipyan and V. V. Kveder, Materialovedenie, No. 1, 2 (1997).
2. L. P. Rakcheeva and N. V. Kamanina, Pis'ma Zh. Tekh. Fiz. **28** (11), 28 (2002) [Tech. Phys. Lett. **28**, 457 (2002)].
3. V. I. Trefilov, D. V. Shchur, B. P. Tarasov, *et al.*, *Fullerenes—The Foundation of Materials of Future* (ADEF, Kiev, 2001), p. 147.
4. M. Pope and C. E. Swenberg, *Electronic Processes in Organic Crystals* (Clarendon, Oxford, 1982; Mir, Moscow, 1985), Vol. 1, p. 545.
5. S. Kazaoui, N. Minami, Y. Tanabe, *et al.*, Phys. Rev. B **58**, 7689 (1998).
6. Yu. A. Ossipyan, Yu. I. Golovin, D. V. Lopatin, *et al.*, Phys. Status Solidi B **223** (3), R14 (2001).
7. Yu. I. Golovin, D. V. Lopatin, R. K. Nikolaev, *et al.*, Dokl. Akad. Nauk **387** (6), 1 (2002) [Dokl. Phys. **47**, 849 (2002)].
8. T. L. Makarova and I. B. Zakharova, Fiz. Tverd. Tela (St. Petersburg) **44**, 478 (2002) [Phys. Solid State **44**, 500 (2002)].

Translated by P. Pozdeev

Technical Physics Letters, Vol. 30, No. 5, 2004, pp. 429–431. Translated from Pis'ma v Zhurnal Tekhnicheskoĭ Fiziki, Vol. 30, No. 10, 2004, pp. 66–70.

Modification of the Shape of Large Germanium Nanoislands on Silicon Surface by Low-Energy Ion Bombardment

A. I. Stognij*, N. N. Novitskii, O. M. Stukalov, A. I. Demchenko, and V. I. Khit'ko**

Research Institute of Radio Materials, Minsk, Belarus

Institute of Solid State and Semiconductor Physics, National Academy of Sciences of Belarus, Minsk, Belarus

*e-mail: * stognij@ifttp.bas-net.by; ** novitski@ifttp.bas-net.by*

Received July 25, 2003; in final form, November 24, 2003

Abstract—Germanium nanoislands on silicon substrates were irradiated by hydrogen and argon ions with energies below 350 eV. In the initial stage, ion bombardment leads to the division of large islands into several small islands irrespective of the ion type. The resulting surface is more homogeneous than the initial and is stable with respect to further ion irradiation. *© 2004 MAIK "Nauka/Interperiodica".*

Structures with quantum dots are of considerable interest for nanoelectronic semiconductor devices [1, 2]. One type of such structures is offered by silicon substrates with germanium nanoislands formed by means of molecular beam epitaxy (MBE) [3–4]. The formation of islands is caused by the relaxation of elastic stresses arising as a result of the lattice misfit and the difference of thermal expansion coefficients at the deposit–substrate interface. However, for some reasons (e.g., because of the presence of defects in the substrate, deposit, and at the interface), the process of stress relaxation results in the appearance of nanoislands having different shapes and dimensions. In order to obtain a more homogeneous pattern, it is possible to use additional thermal treatments, whereby increasing thermal stresses provide for a more complete relaxation of elastic stresses [5]. Unfortunately, such thermal treatments act upon the whole structure and simultaneously activate other, undesired processes (e.g., diffusion) at the silicon–germanium interface.

This Letter suggests using a post-growth irradiation of structures by low-energy ion beams in order to provide for the formation of a more homogeneous pattern of germanium islands on the silicon surface. Use of the ion bombardment instead of thermal annealing allows additional stresses to be developed only in the surface regions exposed to the beam. The low-energy ion action proceeds under controlled energy conditions, while the use of ions with different masses allows the ion sputter processes and the range of ions implanted into substrate to be controlled as well [6].

Figure 1a presents the typical image of the initial surface studied in an atomic force microscope (AFM). Figures 1b and 1c show variations observed on this surface upon bombardment with argon ions for 4 and 8 min, respectively; Figs. 1d–1f show the same patterns upon irradiation of a sample with hydrogen ions for 2, 5, and 8 min, respectively. The method of obtaining germanium nanoislands on silicon by MBE is described in detail elsewhere [4]. The working structures with germanium nanoislands on a 100-mm-diam single crystal silicon wafer for this study were kindly provided by Dr. D. Grützmacher. The experiments were performed on adjacent pieces cut from the wafer.

The sample surface images were obtained using a Femtoskan-001 atomic force microscope (Advanced Technology Center, Moscow State University) with a 5×5-μm scanned field area. The AFM was operated in the contact regime using silicon cantilevers of the CSC12 type obtained from the MicroMash Company (www.spmtips.com). The insets in Fig. 1 show the surface relief cross sections in the regions of selected largest germanium nanoislands scanned as indicated in the corresponding images.

The samples were irradiated with low-energy ions produced by a cold hollow cathode ion source based on a two-stage self-sustained low-pressure gas discharge [7]. The irradiation conditions were as follows: residual pressure, below 2×10^{-5} Torr; working gas pressure, 4×10^{-4} Torr; ion energy, below 350 eV (according to the retarding-field characteristics of a three-grid energy analyzer); ion beam current density, 0.08 mA/cm^2; substrate temperature during irradiation, not exceeding 20°C.

Analysis of the AFM images showed that ion bombardment for 2–4 min leads to the division of large islands into three to four small islands irrespective of the ion type, after which the process of island splitting terminates. This is especially clearly pronounced on the AFM images of samples irradiated for 2–8 min with hydrogen ions (Figs. 1d–1f), where no coarse islands with a height of up to 30 nm are observed (in contrast to the initial surface prior to irradiation). The maximum

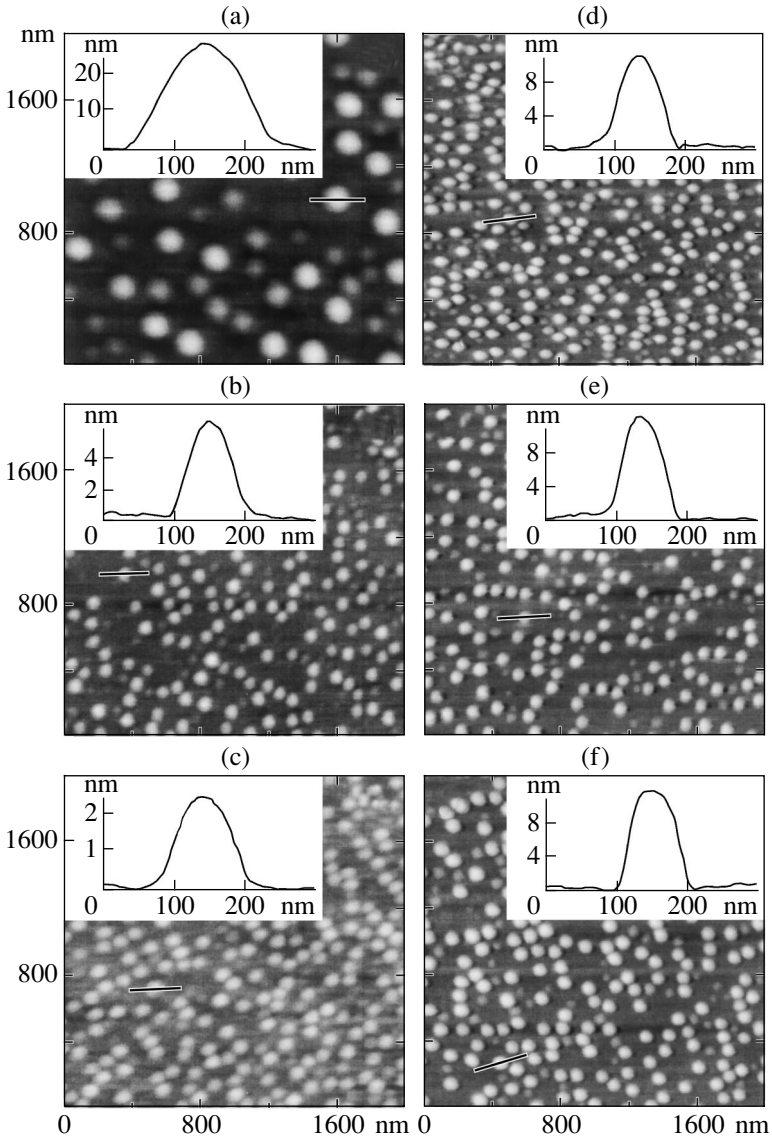

Fig. 1. Typical AFM images showing (a) the initial sample morphology and profiles and (b–f) their evolution in the course of bombardment with (b, c) argon and (d–f) hydrogen ions. See the text for explanations.

island height on the ion-irradiated surface does not exceed 12 nm and the number of islands increases three to four times.

The action of argon ions is more complicated. According to Figs. 1b and 1c the splitting of large islands during the first minutes of irradiation (as well as in the following) is accompanied by significant sputter of the surface. In the course of splitting and afterwards, both large and small islands keep decreasing in the height and smear in the plane, while the substrate surface free of islands acquires increased roughness. According to the published data [8], the surface erosion by hydrogen ions can be ignored because of their small mass, energy, and low irradiation doses employed. However, this cannot be done with respect to argon ions, the more so that the sputtering yield of germanium is 0.2–0.3 atom/ion, which is more than two times the sputtering yield of silicon from a flat crystal surface. As a result, the rate of germanium sputtering from islands is 1–2 nm/min greater than that of silicon from the substrate surface, which is consistent with the rate of decrease in the height of coarse islands (cf. Figs. 1b and 1c).

Thus, irradiation with low-energy hydrogen and argon allows a more homogeneous pattern of germanium nanoislands on silicon to be obtained. This result is achieved already in the initial stage of irradiation due to the division of coarse islands into three to four smaller islands. The reasons for the coarse islands to divide can be related to additional stresses developed under the action of ion bombardment in the surface layers of coarse islands. Since the islands initially occur in

a nonequilibrium state, the additional stresses are sufficient to stimulate the relaxation of excess total stress via division of the islands. Subsequent ion irradiation does not substantially modify the relaxed surface (except for the continuous sputtering with argon ions).

Acknowledgments. The authors are grateful to Dr. D. Grützmacher (Laboratory for Micro- and Nanotechnology, Paul Scherrer Institute, Switzerland) for kindly providing the samples of working structures and for his useful remarks.

REFERENCES

1. N. N. Ledentsov, V. M. Ustinov, V. A. Shchukin, *et al.*, Fiz. Tekh. Poluprovodn. (St. Petersburg) **32**, 385 (1998) [Semiconductors **32**, 343 (1998)].
2. K. Alchalabi, D. Zimin, G. Kostoroz, and H. Zogg, Phys. Rev. Lett. **90**, 026104 (2003).
3. G. Medeiros-Ribeiro, A. M. Bratkovski, T. I. Kamins, *et al.*, Science **279**, 353 (1998).
4. O. Leifeld, R. Hartmann, E. Müller, *et al.*, Nanotechnology, No. 10, 122 (1999).
5. O. G. Schmidt, C. Lange, K. Ebert, *et al.*, Appl. Phys. Lett. **71**, 2340 (1997).
6. A. I. Stognij, N. N. Novitskii, and O. M. Stukalov, Pis'ma Zh. Tekh. Fiz. **29** (2), 6 (2003) [Tech. Phys. Lett. **29**, 43 (2003)].
7. A. I. Stognij and S. V. Koryakin, Prib. Tekh. Éksp., No. 6, 64 (2000).
8. V. S. Smentkowski, Prog. Surf. Sci. **64**, 1 (2000).

Translated by P. Pozdeev

Technical Physics Letters, Vol. 30, No. 5, 2004, pp. 432–434. Translated from Pis'ma v Zhurnal Tekhnicheskoĭ Fiziki, Vol. 30, No. 10, 2004, pp. 71–77.

Thermocapillary Deformation of a Nonisothermal Flowing Liquid Film

Yu. O. Kabova

Lavrentiev Institute of Hydrodynamics, Siberian Division, Russian Academy of Sciences, Novosibirsk, Russia
e-mail: kabova@hydro.nsc.ru

Received September 8, 2003; in final form, December 11, 2003

Abstract—A criterion determining the onset of perturbations in front of the thermocapillary bore in a locally heated flowing liquid film is found and a formula for evaluation of the critical Reynolds number is obtained.

Introduction. Kabov [1] observed and experimentally studied the formation of a spatial self-organized structure in a thin liquid film flowing in a gravity field and locally heated from the side of substrate. Subsequently [2–4], thermocapillary deformations in liquid films flowing under nonisothermal conditions were studied by various methods. In common for all these experiments was the formation of a thermocapillary bore in the liquid near the upper edge of the heater, with a trough observed in front of the bore. The shape of the thermocapillary wave profile was previously studied in [3, 5, 6]. This study was aimed at finding a criterion for the onset of perturbations in front of the thermocapillary bore in a flowing liquid film.

Formulation of the problem. Let us consider established flow in a viscous incompressible liquid film on a flat surface inclined at an angle Θ relative to the horizontal plane. The Cartesian coordinate system (x, y) is oriented so that the Oy axis is perpendicular to the substrate plane, while the Ox axis is directed downstream. A heater with the length L in the flow direction and the center at the origin is situated in the substrate plane. The liquid is characterized by the dynamic viscosity coefficient μ and the surface tension σ, both linearly dependent on the temperature: $\mu(T) = \mu_0 - \mu_T(T - T_0)$ (μ_0, μ_T = const > 0); $\sigma(T) = \sigma_0 - \sigma_T(T - T_0)$ (σ_0, σ_T = const > 0).

The motion of the liquid film is described by the Navier–Stokes and the energy transfer equations; the conditions of thermal balance on the substrate surface and at the gas–liquid interface are written in the general form as $kT_y - b_1(T - T_1(x)) = -q$ at $y = 0$ and $kT_y + b_2(T - T_2(x)) = 0$ at $y = H$. Here, k is the thermal conductivity, b_1 and b_2 are the heat exchange coefficients on the film interfaces, q is the preset heat flux, $T_1(x)$ is the substrate temperature, $T_2(x)$ is the ambient temperature at a certain distance from the corresponding interfaces, T_0 is the initial temperature of the liquid, and ρ is the density of the liquid. The problem setting, the derivation of equation describing a thin flowing film (see Eq. (1) below), and the obtaining of a generalized analytical expression determining of the boundary film thicknesses $h_\pm$ as functions of the preset flow rate Γ, variable viscosity, and the temperature are described in detail elsewhere [6].

Considering the case of local heating when $T_1(x) = T_2(x) = T_0$ and $q(x) \neq 0$ only on the interval $x \in (-L/2, L/2)$, we obtain the boundary conditions for the film thickness, $h_+ = h_- = 1$, and the functions $\gamma(x, h) \longrightarrow 1/2$ and $\varphi(x, h) \longrightarrow 1/3$ for $x \longrightarrow \pm\infty$, so that the dimensionless flow rate is $G = C/3$. Let us linearize a differential equation for the film thickness h,

$$\varphi h^3(h''' - Ah' + C) - h^2\gamma \mathrm{Ma}\tilde{\theta}' = G, \qquad (1)$$

where $\tilde{\theta} = \theta|_{y=h}$. Here, the dimensionless similarity criteria A and C and the Marangoni number Ma are defined as

$$A = \frac{gH_0^2\cos\Theta}{lU^2} = \frac{\cos\Theta}{Fr} \geq 0,$$

$$C = \frac{gH_0\sin\Theta}{U^2} = \frac{\sin\Theta}{\varepsilon Fr} > 0,$$

$$\mathrm{Ma} = \frac{\sigma_T[T]H_0}{Ul\mu_0},$$

where the scales of dimensional quantities (film thickness H_0, liquid flow velocity U, length l, and the temperature deviation from average $[T]$) are given by the formulas

$$H_0 = \left(\frac{3\Gamma\mu_0}{\rho g\sin\Theta}\right)^{1/3}, \quad U = \frac{\mu_0}{\rho H_0}, \quad l = \left(\frac{\sigma_0 H_0^2}{\rho U^2}\right)^{1/3},$$

$$[T] = \sup_x |T_0 - T_2| + \sup_x \frac{q(x)H_0}{k}.$$

Let the film thickness be expressed as $h(x) = 1 + z(x)$, where $z(x)$ is the new unknown function. For a suffi-

ciently low rate of film heating such that Ma $\ll 1$, we can assume that $|z|$, $|z'|$, and $|z'''| \ll 1$ to obtain a linear approximation of Eq. (1):

$$z''' - Az' + 3Cz = \Pi(x, z)$$
$$= \mathrm{Ma}\tilde{\theta}'\left(\frac{\gamma}{\varphi}\right)\Big|_{z=0} - C\left(1 - \frac{1}{3\varphi}\Big|_{z=0}\right) \quad (2)$$

with the boundary conditions

$$z \longrightarrow 0 \quad \text{for} \quad x \longrightarrow \pm\infty. \quad (3)$$

The problem described by Eqs. (2) and (3) admits an exact solution given by the formula

$$z(x) = \int_{-\infty}^{\infty} \Pi(\xi)F(x-\xi)d\xi,$$

where $F(x)$ is the fundamental solution of the corresponding homogeneous equation satisfying the condition $F(x) \longrightarrow 0$ for $x \longrightarrow \pm\infty$. Let $\lambda_1, \lambda_2, \lambda_3$ be the roots of the characteristic polynomial of this equation. As can be readily checked, one of these values (e.g., λ_1) is negative: $\lambda_1 = -a < 0$. Then, according to the Vieta theorem, $\lambda_{2,3} = a/2 \pm \sqrt{a^2/4 - 3C/a}$. As is known, strict inequality

$$\frac{9C^2}{4} - \frac{A^3}{27} \le 0 \quad (4)$$

implies that λ_2 and λ_3 are real positive quantities and their values can be expressed via $|\lambda_1| = a$. Then, the aforementioned fundamental solution $F(x)$ is as follows:

$$F(x) = \frac{a}{8a^3 + 3C}\left\{\chi(x)e^{-ax} - \chi(-x)\frac{\sqrt{a}}{\sqrt{a^3 - 12C}}[(\lambda_3 + a)e^{\lambda_2 x} - (\lambda_2 + a)e^{\lambda_3 x}]\right\}. \quad (5)$$

In the case of equality in (4), we have $\lambda_{2,3} = a/2$ and

$$F(x) = \frac{4}{9a^2}\left\{\chi(x)e^{-ax} - \chi(-x)e^{ax/2}\left[\frac{2x}{3a} - 1\right]\right\}, \quad (6)$$

where $\chi(x)$ is the Heaviside function. Finally, if condition (4) fail to be valid, we have two complex roots $\lambda_{2,3} = a/2 \pm ib$ with $b = \sqrt{12C - a^3}/2\sqrt{a}$. In this case, the fundamental solution has the following form:

$$F(x) = \frac{4}{9a^2 + 4b^2} \times \left\{\chi(x)e^{-ax} - \chi(-x)e^{ax/2}\left[\cos(bx) - \frac{3a}{2b}\sin(bx)\right]\right\}. \quad (7)$$

Note that, for $C = 0$ (which corresponds to $\Theta = 0$), no solution of the linearized equation satisfying condition (3) can be constructed. This situation reflects the fact that construction of a thin layer approximation involves the transverse length scale H_0 related to the flow rate Γ. For zero substrate inclination angle ($\Theta = 0$), $\Gamma = 0$ and the entire construction becomes senseless. As can be readily demonstrated in this case, the nonlinear problem also has no finite solution obeying the boundary conditions. For $C = 0$, Eq. (2) acquires the form

$$z''' - Az' = \frac{\mathrm{Ma}}{1+z}\tilde{\theta}'\frac{\gamma(x, 1+z(x))}{\varphi(x, 1+z(x))},$$

and any solution of this equation also satisfies the integral equation

$$z(x) = \mathrm{Ma}\int_{-\infty}^{\infty}\left(\frac{\tilde{\theta}'(x-\xi)}{1+z(x-\xi)}\right) \times \frac{\gamma(x-\xi, 1+z(x-\xi))}{\varphi(x-\xi, 1+z(x-\xi))}F_2(\xi)d\xi,$$

where

$$F_2(x) = \frac{1}{A}\left(-1 + \frac{e^{-\sqrt{A}x}}{2} + \frac{e^{\sqrt{A}x}}{2}\right)\chi(x) + C_1 + C_2e^{-\sqrt{A}x} + C_2e^{\sqrt{A}x}$$

and C_1, C_2, and C_3 are certain constants. Since we seek a finite solution $e \le h \le E$ and know that (by the physical meaning) $e_1 \le \gamma/\varphi \le E_1$, the function $z(x)$ must satisfy the inequality

$$|z(x)| \ge \frac{\mathrm{Ma}e_1}{E}\int_{-\infty}^{\infty}|\tilde{\theta}'(x-\xi)||F_2(\xi)|d\xi.$$

In order to meet condition (3), it is necessary that

$$\int_{-\infty}^{\infty}|\tilde{\theta}'(x-\xi)||F_2(\xi)|d\xi \xrightarrow[x\to\pm\infty]{} 0,$$

which is valid only if $F_2(x) \longrightarrow 0$ for $x \longrightarrow \pm\infty$. The last condition cannot be satisfied with any set of C_1, C_2, and C_3 constants. Therefore, the nonlinear problem under consideration admits no finite solutions meeting boundary conditions (3).

The fundamental solutions given by formulas (5) and (6) generate solutions of two types having no qualitative differences. In the case of solution (7), the function $F(x)$ for $x < 0$ represents a decaying periodic function with the period b (Fig. 1). The corresponding plot of $z(x)$ exhibits the main thermocapillary bore preceded by a trough and a weakly pronounced ridge upstream, above which the perturbations decay (see Fig. 2, where these features are denoted *1–3*, respectively). In the case of different real roots, the function $F(x)$ determined by formula (5) is monotonic for $x < 0$ and the

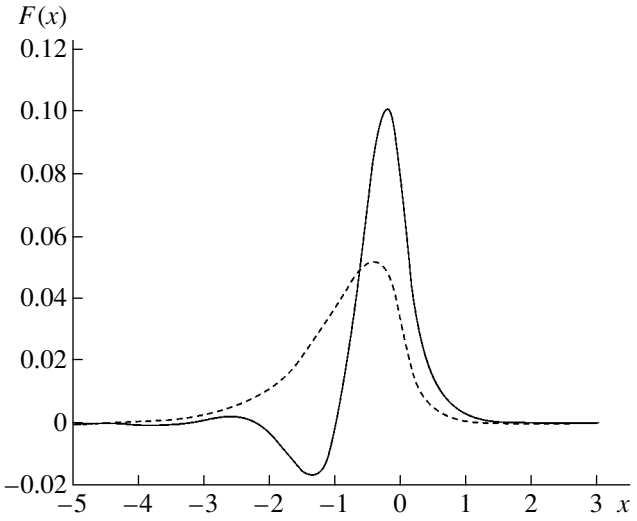

Fig. 1. Fundamental solutions $F(x)$ for $9C^2/4 - A^3/27 < 0$, $A = 10$, $C = 3.8$, Ma = 0.1 (dashed curve) and $9C^2/4 - A^3/27 > 0$, $A = 0$, $C = 10$, Ma = 0.1 (solid curve).

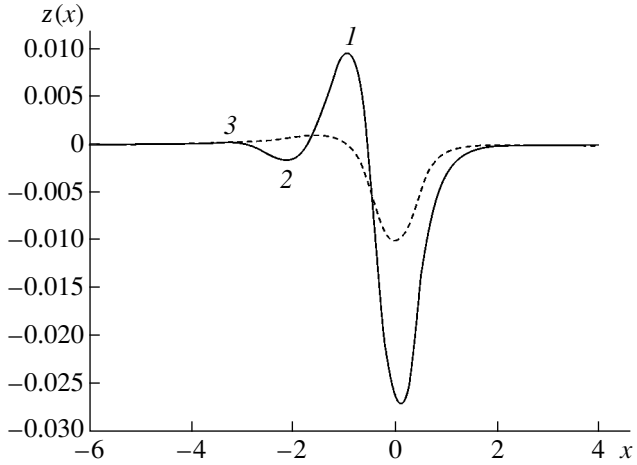

Fig. 2. Solutions of the boundary-value problem formulated by Eqs. (2) and (3), generated by the fundamental solutions $F(x)$ for $9C^2/4 - A^3/27 < 0$, $A = 10$, $C = 3.8$, Ma = 0.1 (dashed curve) and $9C^2/4 - A^3/27 > 0$, $A = 0$, $C = 10$, Ma = 0.1 (solid curve): (*1*) main thermocapillary bore; (*2*) trough; (*3*) weakly pronounced ridge.

solution $z(x)$ has none of the features mentioned above. Constructing the solution $z_0(x)$ of a linearized problem with the right-hand part $\Pi(x, z)$, we may calculate the sequential approximations $z_i(x)$ ($i = 1, 2, \ldots$) with the right-hand parts of the type $\Pi_i(x, z) = \Pi_{i-1}(x, z_{i-1})$, thus obtaining an iterative algorithm for solving the nonlinear problem. Moreover, a solution of the nonlinear problem is also a convolution of the fundamental solution with a certain right-hand part somewhat different from that in the linear case. Therefore, there is ground to believe that condition (4), separating the types of solutions of the linear problem, is also valid in the nonlinear case in a certain region of parameters.

Thus, a condition for the absence of a trough in front of the thermocapillary bore in a flowing liquid film has the form (4), which is equivalent to

$$60.75\frac{\sin^2\Theta}{\cos^3\Theta} \le \frac{\rho g H_0^2}{\sigma_0}.$$

This inequality implies that the trough in front of the bore is absent, provided that the inclination angle is below a certain critical value. In other words, the condition for the absence of a trough in front of the thermocapillary bore is that $\mathrm{Re} \ge \mathrm{Re}_*$, where the critical Reynolds number Re_* is a function of the substrate slope and the properties of the liquid:

$$\mathrm{Re}_* = \frac{(60.75)^{3/2}}{3}\left[\frac{\rho\sigma_0^3}{g\mu_0^4}\right]^{1/2}\frac{\sin^4\Theta}{\cos^{9/2}\Theta}.$$

For the vertical substrate, perturbations in front of the thermocapillary bore in the liquid arise for any sufficiently small Reynolds number, because the condition of their absence appears as $\mathrm{Re} \longrightarrow \infty$. The results reported in [2–4] were obtained for a vertical substrate in a broad range of Reynolds numbers (Re = 0.09–2). The appearance of a trough in front of the thermocapillary bore in the entire range of Re values confirms the conclusions of this study.

Acknowledgments. This study was supported by the Russian Foundation for Basic Research (project no. 02-02-16478) and the Presidential Program of Support for the Leading Scientific Schools (project no. NSh-902.2003.1).

REFERENCES

1. O. A. Kabov, Teplofiz. Aéromekh. **5**, 597 (1998).
2. B. Scheid, O. A. Kabov, C. Minetti, *et al.*, in *Proceedings of the 3rd European Conference on Thermal Sciences, Heidelberg, 2000*, Vol. 1, pp. 651–657.
3. O. A. Kabov, J.-C. Legros, I. V. Marchuk, *et al.*, Izv. Ross. Akad. Nauk, Mekh. Zhidk. Gaza, No. 3, 200 (2001).
4. D. V. Zaitsev, O. A. Kabov, and A. R. Evseev, Exp. Fluids **34**, 748 (2003).
5. V. V. Kuznetsov, Russ. J. Eng. Thermophys. **10**, 107 (2000).
6. Yu. O. Kabova and V. V. Kuznetsov, Prikl. Mekh. Tekh. Fiz. **43** (6), 134 (2002).

Translated by P. Pozdeev

Technical Physics Letters, Vol. 30, No. 5, 2004, pp. 435–437. Translated from Pis'ma v Zhurnal Tekhnicheskoĭ Fiziki, Vol. 30, No. 10, 2004, pp. 78–82.

Magnetothermo-emf of a One-Dimensional Superlattice

D. V. Zav'yalov and S. V. Kryuchkov

Volgograd State Pedagogical University, Volgograd, Russia

e-mail: sed@fizmat.vspu.ru

Received October 20, 2003

Abstract—The longitudinal magnetothermo-emf of a one-dimensional semiconductor superlattice has been studied in the quasi-classical limit ($\tau^{-1} \ll \Omega \ll \mu$, where τ is the charge carrier relaxation time, Ω is the cyclotron frequency, and μ is the chemical potential). It is established that oscillations caused by the Landau quantization are modulated by oscillations related to a finite width of the conduction band. Conditions under which such a modulation is especially clearly manifested are determined. © *2004 MAIK "Nauka/Interperiodica".*

The kinetic characteristics of conductors may exhibit oscillations depending on the strength H of an external magnetic field applied to the sample. This phenomenon is analogous to the magnetic moment oscillations in the de Haas–van Alphen effect [1], but, in contrast to the latter, the oscillations of kinetic coefficients are caused by the influence of magnetic field on the process of charge carrier scattering [2, 3]. In particular, the longitudinal magnetothermo-emf of a metal with an arbitrary Fermi surface was studied in [4]. However, previous investigations were restricted to wide-band-gap materials in which the main contribution to the effect is due to electrons occurring in the vicinity of the extrema in the conduction band.

In recent years, there has been growing interest in nanostructures and semiconductor superstructures [5]. Such materials may possess a small width of the conduction band (characterized by a halfwidth of $\Delta \leq 10^{-1}$ eV), which may give rise to a number of specific properties. In this context, we have studied the effect of a finite width of the conduction band on the magnetothermo-emf of a semiconductor superlattice (SL) in the case of charge carrier scattering on impurities.

Let us restrict the consideration to the quasi-classical limit, whereby $\tau^{-1} \ll \Omega \ll \mu$, where μ is the chemical potential, $\Omega = eH/(m^*c)$ is the cyclotron frequency, τ is the charge carrier relaxation time, and m^* is the effective electron mass in the plane perpendicular to the SL axis (we use the system of units in which $\hbar = 1$). Let a magnetic field be directed along the OZ axis coinciding with the SL axis. In this case, the electron energy is determined by the relation (see, e.g., [6])

$$\varepsilon = \Omega\left(n + \frac{1}{2}\right) + \frac{eH}{2mc}\sigma_z + \Delta(1 - \cos(p_z d)), \qquad (1)$$

where m is the free electron mass, σ_z is the Pauli matrix, and d is the SL lattice. We will also assume that the sample is sufficiently pure so that $T\tau \gg 1$ (τ is the electron relaxation time).

In the quasi-classical limit adopted, the probability of scattering is [4]

$$W(\varepsilon) = \frac{n_i|U|^2 eH}{2\pi c}\int dp_z' \sum_{n'} \delta(\varepsilon - \varepsilon_\sigma(p_z', n')), \qquad (2)$$

where n_i is the impurity concentration. For the sake of simplicity, the scattering matrix element U will be assumed constant. This is possible, provided that the depth of the impurity level is much greater than the SL potential variation per SL period d: in this case, the wave function of an electron localized at the impurity will be the same as that in a homogeneous crystal.

We assume the electron–impurity interaction to be spin-independent and transfer this dependence formally to the chemical potential: $\varepsilon_\sigma(p_z, n) - \mu = \varepsilon(p_z, n) - \mu_\sigma$, $\mu_\sigma = \mu + eH\sigma_z/(2ms)$. Transforming expression (2) with the aid of the Poisson formula, we obtain

$$W = W_0\left[1 + \frac{eH}{\pi^2 c\nu(\varepsilon)} \times \mathrm{Re}\left\{dp_z' \sum_{k=1}^{\infty} \int_{-1/2}^{\infty} \delta(\varepsilon - \varepsilon(p_z', n'))\exp(2\pi i k n')dn'\right\}\right], \qquad (3)$$

where $W_0 = \pi n_i|U|^2\nu(\varepsilon)$ is the scattering probability independent of the magnetic field strength and $\nu(\varepsilon)$ is the density of energy states. Then, passing to the integration with respect to the energy, we obtain the expression for the relaxation time

$$\tau(\varepsilon) = \tau_0\left[1 - \frac{m^*(\varepsilon)}{\pi^2\nu(\varepsilon)} \times \sum_{k=1}^{\infty} \mathrm{Re}\left\{\exp(-i\pi k)\exp\left(i\frac{2\pi k\varepsilon}{\Omega}\right)\Psi(\Omega, k)\right\}\right], \qquad (4)$$

1063-7850/04/3005-0435$26.00 © 2004 MAIK "Nauka/Interperiodica"

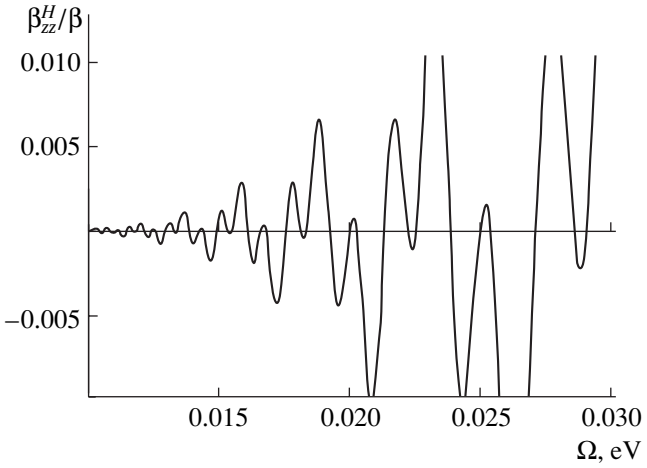

Fig. 1. A plot of the magnetothermo-emf versus magnetic field strength for an SL with μ = 0.3 eV and Δ = 0.2 eV (kT = 0.005 eV, $m^* = m$).

where

$$\Psi(\Omega, k) = \int dp_z \exp(-2\pi i/\Omega\Delta[1-\cos(p_z d)]) = d^{-1}\exp(-2\pi ik\Delta/\Omega)J_0(2\pi k\Delta/\Omega).$$

The component of the tensor of the thermoelectric coefficient in the field configuration $\nabla T \parallel \mathbf{E} \parallel \mathbf{H} \parallel OZ$ is calculated as [1]

$$\beta_{zz} = -\frac{e}{3T}\int v_z^2(\xi, \varphi, \theta)\tau(\xi)\nu(\xi) \times \frac{\xi d\xi}{4T\cosh^2(\xi/2T)}\frac{d\varphi\sin(\theta)d\theta}{4\pi}, \quad (5)$$

where $v_z^2(\xi, \varphi, \theta) = \Delta d\sin(p\sin(\theta)d)$ and p is determined by solving the equation

$$\varepsilon = \frac{p^2}{2m^*}\cos^2(\theta) + \Delta(1-\cos(p\sin(\theta)d)). \quad (6)$$

Since this equation cannot be solved analytically, the integration with respect to θ is performed by numerical methods (the integration over φ yields 2π because the Fermi surface of the SL is symmetric relative to the magnetic field direction). However, the quantity $v_z(\xi, \varphi, \theta)$ does not bear the field dependence of interest and, hence, expression (5) can be rewritten as

$$\beta_{zz} = -\frac{e}{3T}\int \bar{v}_z^2(\xi)\tau(\xi)\nu(\xi)\frac{\xi d\xi}{4T\cosh^2(\xi/2T)}, \quad (7)$$

where

$$\bar{v}_z^2(\xi, \varphi, \theta) = \int v_z^2(\xi, \varphi, \theta)\sin(\theta)\frac{d\varphi d\theta}{4\pi}.$$

Substituting formula (4) into expression (7), integrating over ξ, and averaging over the spin, we eventually obtain

$$\beta_{zz} = \beta_{zz}^0 + \beta_{zz}^H, \quad (8)$$

where

$$\beta_{zz}^0 = -\frac{e\pi^2}{9}T\frac{d(\bar{v}_z^2(\mu)\tau_0(\mu)\nu(\mu))}{d\mu}$$

is the thermoelectric coefficient in the absence of a magnetic field. The second term in relation (8) is

$$\beta_{zz}^H = \frac{2em^*(\mu)}{3\pi^2}\bar{v}_z^2(\mu)\tau_0(\mu)\mathrm{Re}\left\{\sum_{k=1}^{\infty} i\cos\left(\pi k\frac{m^*(\mu)}{m}\right) \times \exp\left(\frac{2\pi ik\mu}{m^*(\mu)\Omega}\right)\Psi(\Omega, k)\Psi_1\left(\frac{2\pi^2 Tk}{\Omega}\right)\right\}, \quad (9)$$

where

$$\Psi_1(x) = \frac{\pi}{2\cosh(x)}(x\cosh(x)-1).$$

Separating the real part in expression (9), we obtain

$$\beta_{zz}^H = \beta\sum_{k=1}^{\infty}\cos\left(\pi k\frac{m^*}{m}\right)\sin\left(\frac{2\pi k}{\Omega}(\mu-\Delta)\right) \times J_0\left(\frac{2\pi k\Delta}{\Omega}\right)\Psi_1\left(\frac{2\pi^2 Tk}{\Omega}\right), \quad (10)$$

where

$$\beta = -\frac{4em^*}{3d^2}\bar{v}_z^2(\mu)\tau_0(\mu).$$

As can be seen from formula (10), the oscillatory term β_{zz}^H in the SL magnetothermo-emf significantly differs from an analogous expression for wide-bandgap materials [4]. First, the presence of a factor in $J_0(x)$ must lead to additional oscillations in β_{zz}^H. This circumstance is explained by the presence of a new period of carrier motion along the SL axis. The new oscillations are especially clearly manifested in the range of fields where $\Omega \approx 2\pi^2 T$ (Fig. 1). If, in addition, $\mu - \Delta \ll \Omega$, the oscillations are described only by trigonometric functions because $\Delta \gg \Omega$ and $J_0(x) = \sqrt{\frac{2}{\pi x}}\cos\left(x - \frac{\pi}{4}\right)$ (Fig. 2).

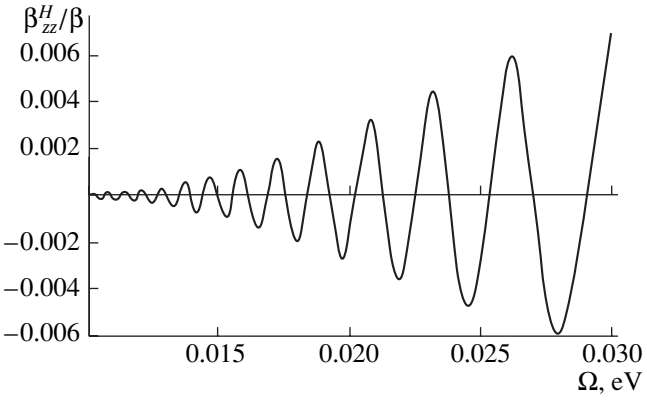

Fig. 2. A plot of the magnetothermo-emf versus magnetic field strength for an SL with $\mu = 0.201$ eV and $\Delta = 0.2$ eV ($kT = 0.005$ eV, $m^* = m$).

Second, the oscillation additive to β_{zz} vanishes if the chemical potential μ is equal to halfwidth Δ of the SL conduction band. Note that, in the case under consideration, a determining role is played by electrons with the energy $\varepsilon \approx \mu$ ($\varepsilon - \mu \ll T$). For $\mu = \Delta$, such electrons are characterized by $\partial^2\varepsilon(\mathbf{p})/\partial p_z^2 = 0$ and the longitudinal effective mass $m_\parallel \longrightarrow \infty$.

REFERENCES

1. A. A. Abrikosov, *Fundamentals of the Theory of Metals* (Nauka, Moscow, 1987; North-Holland, Amsterdam, 1988).
2. E. N. Adams and T. D. Holstein, J. Phys. Chem. Solids **10**, 254 (1959).
3. A. A. Abrikosov, Zh. Éksp. Teor. Fiz. **56**, 1391 (1969) [Sov. Phys. JETP **29**, 746 (1969)].
4. A. A. Varlamov and A. V. Pantsulaya, Pis'ma Zh. Éksp. Teor. Fiz. **49**, 152 (1989) [JETP Lett. **49**, 178 (1989)].
5. Zh. I. Alferov, Fiz. Tekh. Poluprovodn. (St. Petersburg) **32**, 3 (1998) [Semiconductors **32**, 1 (1998)].
6. V. N. Lutskiĭ, M. I. Kaganov, and A. Ya. Shik, Zh. Éksp. Teor. Fiz. **92**, 721 (1987) [Sov. Phys. JETP **65**, 406 (1987)].

Translated by P. Pozdeev

Technical Physics Letters, Vol. 30, No. 5, 2004, pp. 438–440. Translated from Pis'ma v Zhurnal Tekhnicheskoĭ Fiziki, Vol. 30, No. 10, 2004, pp. 83–88.

The Dynamics of Self-Organization of Hexagonal Pore Arrays during Anodic Etching and Oxidation of Semiconductors and Metals

V. I. Emel'yanov[a], V. V. Igumnov[a], and V. V. Starkov[b]

[a] *Moscow State University, Moscow, Russia*

[b] *Institute for Problems of Microelectronic Technologies, Russian Academy of Sciences, Chernogolovka, Moscow oblast, Russia*

Received November 5, 2003

Abstract—The dynamics of self-organization in the **q** space of hexagonal pore arrays during anodic oxidation of aluminum and anodic etching of silicon for various times has been traced by means of the Fourier transform of micrographs obtained by scanning electron microscopy of the resulting porous surfaces of Al_2O_3 and silicon. The results of application of the nonlinear defect-deformation theory of self-organized hexagonal pore arrays to the description of this dynamics are considered on a qualitative level. © *2004 MAIK "Nauka/Interperiodica".*

Introduction. The physical mechanism of the spontaneous formation of pore arrays during the anodic etching and oxidation of semiconductors and metals is still a subject of discussion [1, 2]. Recently, we suggested a defect-deformation (DD) mechanism explaining the spontaneous formation of self-ordered pore arrays and experimentally observed a quasi-hexagonal order in the arrangement of pores on the etched surface of silicon [3]. A linear DD theory of the formation of pore arrays was developed in [4]. Recently [5], we modified the symmetry of the anodic pore array in silicon from quasi-hexagonal to one-dimensional by applying external mechanical stress and interpreted this effect in terms of the DD mechanism.

On the other hand, it is known that the anodic oxidation of aluminum [6] and etching of InP [7] lead to the formation of virtually ideal hexagonal pore arrays. In this context, we have performed a comparative study of the dynamics of formation of hexagonal pore arrays in Al_2O_3 and silicon. The possible factors responsible for distinctions in the degree of coherency of the hexagonal pore arrays in Al_2O_3, InP, and Si are discussed based on the DD mechanism.

Experimental results. Figure 1 shows scanning electron microscopy (SEM) images of the surface of Al_2O_3 (contacting with Al substrate) and the corresponding two-dimensional (2D) Fourier spectra $F(k_x, k_y)$ for three times t_{ox} of the anodic oxidation of aluminum [6]. For $t_{ox} = 0.5$ h, the spectrum comprises a circular ring (plateau) of finite thickness featuring 12 maxima (Fig. 1a). As the treatment time increases to $t_{ox} = 4$ h, the ring decreases in width and retains only six maxima (Fig. 1b). These spectra correspond to quasi-hexagonal pore arrays (see the SEM micrographs in Figs. 1a and 1b). Finally, at $t_{ox} = 16$ h, the ring becomes a circle and the spectrum consists of six narrow equidistant maxima, which corresponds to the ideal hexagonal pore array (Fig. 1c).

SEM images of a silicon surface etched for two different times t_{etch} and the corresponding 2D Fourier spectra were reported in [4, Fig. 5]. For $t_{etch} = 10$ min, the spectrum represented a circular plateau of a finite width with 12 maxima (eight of which merged into four pairs), which corresponded to a disordered pore array [4, Fig. 5a]. When the treatment time was increased to $t_{etch} = 30$ min, the plateau thickness remained unchanged, but only six maxima were retained, which corresponded to a quasi-hexagonal pore array [4, Fig. 5b]. Further etching did not change this pattern [4].

DD mechanism. According to the DD mechanism [3–5], the symmetry and periodicity of the pore array repeat these of a seeding DD structure arising on the sample surface as a result of the DD instability development in a near-surface defect-rich "film" with a thickness h (for details, see reviews [8, 9]). When the density (or the rate of generation) of interstices or vacancies formed in the course of etching or oxidation exceeds a certain critical level, the surface features the formation of a DD lattice at an increment of λ_q. The density of defects, $n_d(\mathbf{r})$, and the surface relief ζ in this lattice vary according to the law $n_d(\mathbf{r})$, $\zeta(\mathbf{r}) = n_\mathbf{q}$, $\zeta_\mathbf{q}\exp(i\mathbf{qr} + \lambda_q t)$, where $\mathbf{q}$ is the lattice vector lying in the surface plane (interstices accumulate at the ridges, and vacancies, at the dents of the surface relief).

We have developed a nonlinear theory based on the kinetic equations for the Fourier amplitudes $n_\mathbf{q}$ [4], according to which self-organization of the seeding DD structure in the **q** space proceeds in four stages. In the first (linear) stage, lattices with the wave vectors $\mathbf{q}_m$ cor-

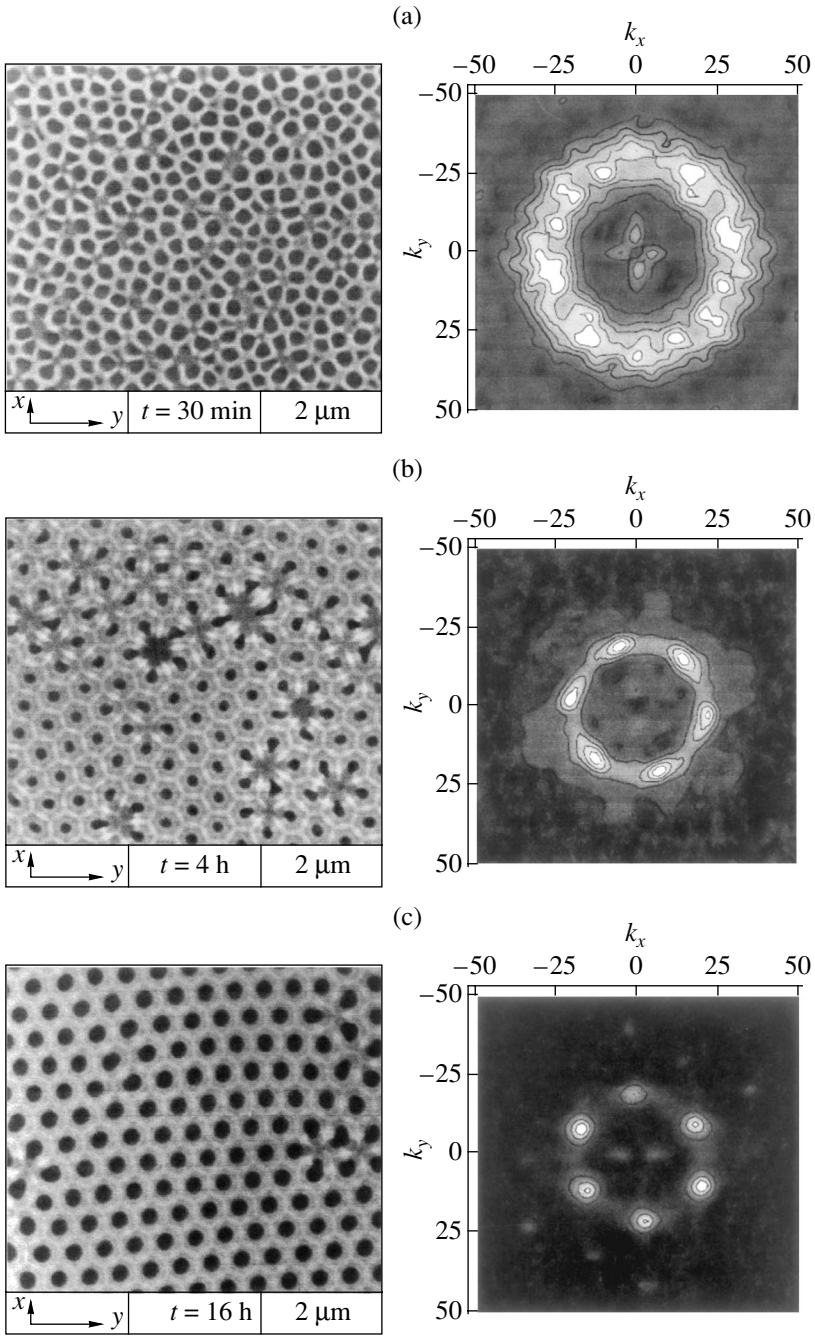

Fig. 1. SEM micrographs of the surface of Al_2O_3 contacting with aluminum substrate for three times of anodic oxidation [6] and the corresponding 2D Fourier spectra $F(k_x, k_y)$: (a) 30 min; (b) 4 h; (c) 16 h (see the text for explanations).

responding to maximum increments λ_{q_m} are separated from the initial chaotic set of fluctuational DD lattices with the vectors **q** randomly distributed with respect to both magnitude and direction. Besides these (dominating) lattices, there is increasing continuum of DD lattices with randomly oriented wave vectors and the moduli in the vicinity of q_m in the gain band $\lambda_q > 0$ [4]. The Fourier spectrum of such a structure has the form of a ring with a width corresponding to the gain bandwidth.

In the second stage, the wave vectors with equal length of the dominating DD lattices exhibit nonlinear interaction and form equilateral triangles (triads) randomly oriented on the surface. Each triad corresponds to a hexagonal DD structure with a random orientation.

In the third stage, the nonlinear interaction of triads leads to their orientational ordering. This corresponds

to a collapse of the angular spectrum of DD modes, which has a threshold character with respect to the defect density. The resulting orientation of triads is selected due to spontaneous symmetry breakage or due to the intrinsic elastic anisotropy of the surface. The Fourier spectrum of such a DD structure with identically oriented triads represents a ring of finite thickness with six equidistant maxima. Each pair of maxima occurring at the ends of the same diameter corresponds to one of the three lattices comprising a triad.

In the fourth stage, the nonlinear interaction of the DD lattices leads to a threshold collapse of the DD mode spectrum in the scalar space, whereby the ring width in the Fourier spectrum becomes equal to zero. The resulting spectrum appears as a circle with six equidistant maxima and corresponds to the ideal cellular hexagonal DD structure. The third and fourth stages may proceed simultaneously.

The spectra reported in [4, Figs. 1 and 5] correspond to different stages of the above temporal evolution of the DD structure in the **q** space. In the case of aluminum, Fig. 1a corresponds to the second stage, and Fig. 1b, to the third and, partly, fourth stage; finally, Fig. 1c reflects the end of the fourth stage of this evolution. In the case of silicon, the pattern in [4, Fig. 5a] corresponds to the second and, partly, third stage, while [4, Fig. 5b] reflects the end of the third stage.

Discussion of results. The difference in the form of the final spectra (and in the degree of coherence of the corresponding pore arrays) can be explained by different scenarios of synchronization of the DD structures and the pore array during the anodic treatment of aluminum and silicon. In the course of the anodic oxidation of aluminum, the seeding DD structure forms and evolves on the surface of aluminum contacting with the oxide layer, while the pores nucleate at this contact surface and grow into the bulk of oxide. Therefore, the pore array at the contact surface may continuously (up to the end of the fourth stage) adjust to the DD structure evolving on the metal surface. The final pore array is essentially a replica of the final DD distribution and, hence, possesses the ideal hexagonal symmetry (Fig. 1c).

According to the DD mechanism [3–5], the distance between the pores is of the order of the defect film thickness $2h$. In aluminum, the h value can represent the vacancy diffusion length, while in semiconductors, this can be the thickness of the space charge region. Indeed, a correlation between the pore spacing and the space charge region size in silicon has been established in a broad range of donor (N_D) and acceptor (N_A) concentrations: 10^{14} cm^{-3} < $N_{D,A}$ < 10^{20} cm^{-3} [10]. Since the space charge region ("film") moves in the course of etching with the interface between porous and intact semiconductor regions, the DD structure together with the synchronized pore array may also complete the fourth stage of self-organization. This will result (similarly to the case of oxidation) in the formation of the ideal coherent pore array (the case of InP).

In silicon, etching proceeds at the sites of the accumulation of vacancies in the DD structures and, in the stage of deep pores, probably ceases to depend on further evolution of the DD structure. Therefore, the final distribution of pores in silicon corresponds to the distribution of DD cells in the early stage of their evolution and, accordingly, possesses a low degree of coherency.

REFERENCES

1. D. Crouse, Y. H. Lo, and A. E. Miller, Appl. Phys. Lett. **76**, 49 (2000).
2. D. N. Goryachev, L. V. Belyakov, and O. M. Sreseli, Fiz. Tekh. Poluprovodn. (St. Petersburg) **34**, 1130 (2000) [Semiconductors **34**, 1090 (2000)].
3. B. I. Emel'yanov, K. I. Eremin, and V. V. Starkov, Kvantovaya Élektron. (Moscow) **32**, 473 (2002).
4. V. I. Emel'yanov, K. I. Eremin, V. V. Starkov, and E. Yu. Gavrilin, Laser Phys. **13**, 1442 (2003).
5. V. I. Emel'yanov, K. I. Eremin, V. V. Starkov, and E. Yu. Gavrilin, Pis'ma Zh. Tekh. Fiz. **29** (6), 19 (2003) [Tech. Phys. Lett. **29**, 226 (2003)].
6. H. Masuda, K. Yada, and A. Osaka, Jpn. J. Appl. Phys. **37**, L1340 (1998).
7. S. Langa, V. Christophersen, J. Carstensen, *et al.*, Phys. Status Solidi A **197**, 77 (2003).
8. V. I. Emel'yanov, Microelectron. Eng. **69**, 435 (2003).
9. V. I. Emel'yanov, Kvantovaya Élektron. (Moscow) **28**, 2 (1999); V. I. Emel'yanov and I. M. Panin, Fiz. Tverd. Tela (St. Petersburg) **42**, 1026 (2000) [Phys. Solid State **42**, 1058 (2000)].
10. V. Lehman, R. Stengl, and A. Luigart, Mater. Sci. Eng. B **69–70**, 11 (2000).

Translated by P. Pozdeev

Technical Physics Letters, Vol. 30, No. 5, 2004, pp. 441–443. Translated from Pis'ma v Zhurnal Tekhnicheskoĭ Fiziki, Vol. 30, No. 10, 2004, pp. 89–95.

Determining Parameters of a Multilayer Heterostructure by Joint Analysis of the X-ray Rocking Curves Measured for Various Crystallographic Planes

A. A. Lomov[a,*], M. A. Chuev[b], and G. V. Ganin[a]

[a] *Shubnikov Institute of Crystallography, Russian Academy of Sciences, Moscow, 117333 Russia*
[b] *Institute of Physics and Technology, Russian Academy of Sciences, Moscow, Russia*
* *e-mail: a.lomov@ns.crys.ras.ru*
Received November 13, 2003

Abstract—The X-ray rocking curves of (004), (113), and (115) planes of a pseudomorphous $In_xGa_{1-x}As/GaAs(001)$ heterostructure with a single 12-nm-thick quantum well were measured by double-crystal X-ray diffractometry. The joint fitting of the X-ray diffraction curves for various crystallographic planes has been performed for the first time, which provides more reliable information about the thickness, deformation, and amorphization of layers in the heterostructure studied. *© 2004 MAIK "Nauka/Interperiodica".*

Introduction. Investigations of the structure of near-surface layers of single crystals and multilayer crystalline systems receive much attention in basic science and applications. Among the modern surface diagnostic techniques, high-resolution X-ray diffractometry occupies a special position, because this method is capable of strain and amorphization profiling in depth. Originally, this task was successfully solved in [1, 2]. Later, the problem of restoring the desired parameters was encountered in the context of uncertainty arising as a result of the loss of information about the phase of a diffracted wave [3, 4]. It was demonstrated [5] that the number of solutions corresponding to the same shape of the X-ray rocking curves is 2^N, where N is the number of sublayers into which the subsurface layer is divided. In order to reduce the number of possible solutions, it is common practice to use a priori information or data obtained by phase sensitive methods [6, 7]. In [8, 9], the inverse task of the strain and amorphization profile restoration was solved using the χ^2 method. The results showed satisfactory agreement between theory and experiment for χ^2 values close to unity, which corresponds to mathematically justified criteria of selecting correct solutions [10].

The complete set of X-ray diffraction reflections contains exhaustive information about distortions of the sample structure. Therefore, the problem of uncertainty elimination can be successfully solved by modeling a greater number of reflections from various families of crystallographic planes. This is a standard approach to the crystal structure determination [11]. In [12, 13], different orders of reflection were used for the characterization of multilayer structures and superlattices. However, simultaneous fitting of the diffraction curves of various reflections was never used before for the investigation of surface layers of single crystals.

This study is devoted to the development of a method for restoration of the strain and amorphization profiles by means of joint fitting of the X-ray rocking curves measured for various crystallographic planes. The proposed method is demonstrated by application to a pseudomorphous $In_xGa_{1-x}As/GaAs(001)$ heterostructure with a single quantum well.

Experiment. A single $In_xGa_{1-x}As$ quantum well with a thickness of $l = 12$ nm and an indium content of $x = 0.08$ was grown by molecular beam epitaxy on the surface of a GaAs(001) single crystal substrate oriented 3° off the [110] axis. In order to eliminate the diffusion of impurities and defects from substrate into the epitaxial $In_xGa_{1-x}As$ layer, the sample surface was preliminarily coated with a 0.5-μm-thick buffer layer of GaAs. Finally, the quantum well was covered with a 100-nm-thick GaAs layer.

The X-ray rocking curves were measured using $\theta/2\theta$ scans with a 6′–10′ slit positioned in front of the detector. The experimental geometry is depicted in Fig. 1. With allowance of the asymmetry coefficient $\beta(\psi)$ influencing the dynamical diffraction, the scans were performed in the $\theta/(1 + \beta)\theta$ mode [9]. The probing radiation was produced by an X-ray tube with a copper anode. We studied the symmetric Bragg diffraction from (004) planes and the non-complanar diffraction from (113) and (115) planes. When mounting the sample crystal in the non-complanar symmetric geometry, special attention was paid to provide for the adjustment corresponding to $\beta = 1$.

Results and discussion. Figure 2 shows the experimental X-ray rocking curves (depicted by vertical bars) measured for the (004), (113), and (115) planes of a

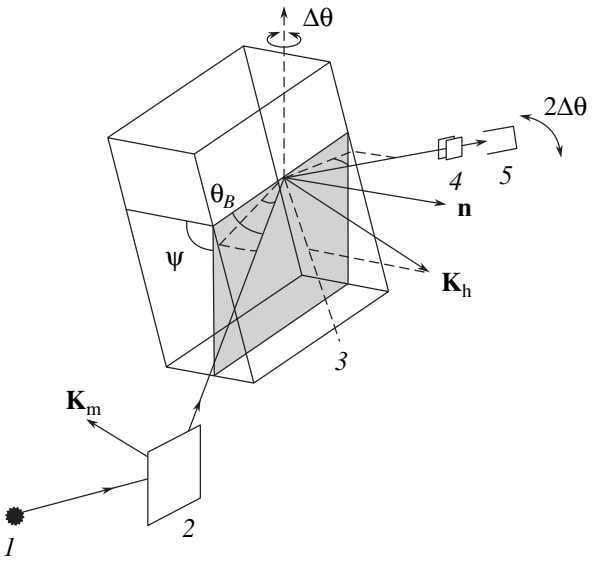

Fig. 1. The experimental geometry: (*1*) X-ray source; (*2*) monochromator crystal; (*3*) sample; (*4*) slits; (*5*) detector; (**n**) normal to the sample surface; ($\mathbf{K}_m$, $\mathbf{K}_h$) reciprocal lattice vectors of the monochromator and sample, respectively; (θ_B) Bragg's angle.

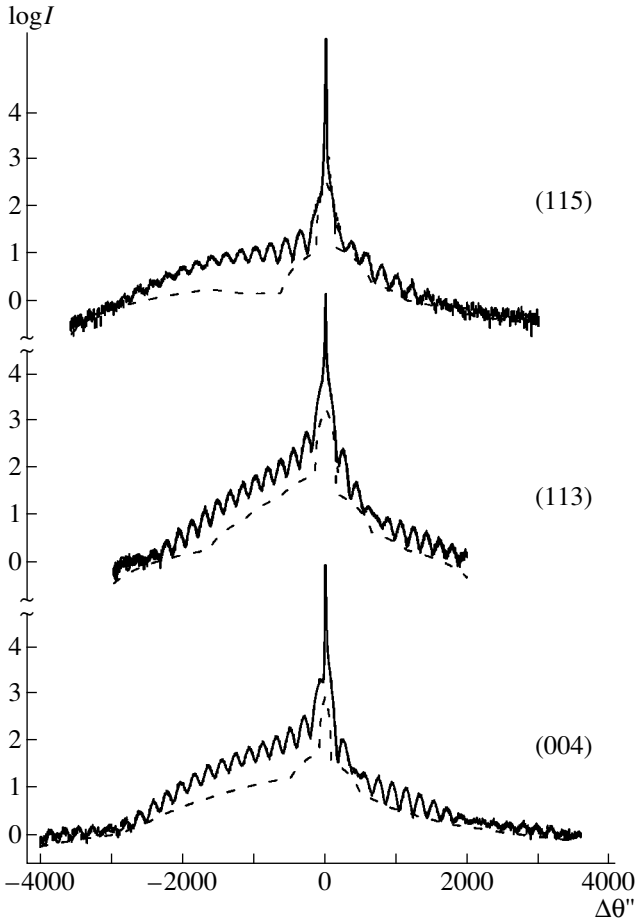

Fig. 2. Experimental X-ray rocking curves for the (004), (113), and (115) reflections of an $In_xGa_{1-x}As/GaAs(001)$ heterostructure with a single 12-nm-thick quantum well (vertical bars) in comparison to the theoretical curves (sold lines) and noncoherent diffuse background (dashed lines).

sample structure. The curves exhibit a large number of oscillations typical of multilayer systems consisting of high-quality layers separated by sharp interfaces. It should be noted that the curves markedly differ from one another.

In the first stage of analysis, the X-ray rocking curves for each reflection were separately treated using a procedure described elsewhere [8, 9]. The initial approximation was based on the structural parameters of the growth model. The fitting was performed by varying the thicknesses of all sublayers l_j (j is the layer number), the normal strain component $\Delta a_j^{\perp}/a$ (a is the substrate lattice parameter), and the amorphization factor $f_j^{(h)}$ as determined by the static Debye–Waller factor w_j:

$$f_j^{(h)} = \exp(-w_j^{(h)}) = \exp(-\langle(\mathbf{K}_h\mathbf{u})^2\rangle_j), \qquad (1)$$

where $\mathbf{K}_h$ is the reciprocal lattice vector for a given *hkl* reflection and **u** is the vector of chaotic displacement of atoms from regular positions. The amorphization factor describes a decrease in reflectivity of the given sublayer as a result of the crystal lattice imperfection. The fitting of X-ray rocking curves was performed with allowance of diffuse scattering [9].

Figure 2 also shows the theoretical curves (solid lines) calculated within the framework of the dynamical X-ray diffraction theory and the intensities of diffuse scattering (dashes lines). The values of structural parameters determined using a four-layer model with separate analysis of the X-ray rocking curves for the (004), (113), and (115) reflections are given in the table. As can be seen, the parameters restored upon separate analysis of the experimental curves have close values corresponding to the growth conditions. However, the differences between these values exceed the rms errors. The introduction of additional sublayers into the model somewhat reduced the χ^2 value but at the expense of increasing uncertainties of the parameters.

The differences in the values of parameters (see table) independently restored from the X-ray rocking curves measured for various crystallographic planes is explained by the following factors. First, since the direct contribution of a quantum well to the diffraction intensity is small, the X-ray rocking curve shape is primarily determined by the coherent shift (caused by the thin quantum well) of atomic planes of a relatively thick upper GaAs layer relative to the substrate. This displacement results in an additional phase shift between the amplitudes of X-ray scattering from the upper GaAs layer and the substrate and, hence, in the appearance of numerous oscillations on the tails of the diffraction curve. The resulting diffraction pattern is determined by the shift $\Delta u \approx (\Delta a_j^{\perp}/a)l_j$, whereby the two parameters of the quantum well appear as coupled.

The parameters of layers of a sample heterostructure determined by independent analysis of X-ray rocking curves for various crystallographic planes

Layer	*hkl* = 004, χ^2 = 2.51			*hkl* = 113, χ^2 = 2.52			*hkl* = 115, χ^2 = 2.41		
	l_j, nm	$\Delta a_j^{\perp}/a$, %	f_j	l_j, nm	$\Delta a_j^{\perp}/a$, %	f_j	l_j, nm	$\Delta a_j^{\perp}/a$, %	f_j
1	99.1(1)	–0.002(1)	1.00(1)	99.7(1)	–0.002(1)	0.95(1)	99.6(1)	–0.000(1)	0.86(1)
2	11.9(1)	0.88(1)	0.99(1)	11.6(1)	0.85(1)	0.99(1)	12.4(2)	0.83(1)	0.86(2)
3	498(3)	0.000(1)	0.97(1)	501(1)	0.000(1)	0.95(1)	501(1)	0.000(1)	0.94(3)
Substrate			0.97(1)	Substrate		0.92(1)	Substrate		0.97(3)

Second, the values of the static Debye–Waller factors $f_j^{(h)}$ for various reflections are determined, according to formula (1), by the scalar product of vectors $\mathbf{K}_h$ and $\mathbf{u}$ and, hence, are naturally different.

In order to eliminate the discrepancy of parameters obtained by fitting, we have developed a special procedure for the joint analysis of various sets of experimental data. The experimental X-ray rocking curves of the (004), (113), and (115) reflections were analyzed within the framework of the χ^2 method with variations of the same parameters: the thicknesses of sublayers l_j and the crystal lattice distortions $\Delta a_j^{\perp}/a$. In the simplest approximation of isotropic distribution of the chaotic displacement $\mathbf{u}$, the factors $f_j^{(h)}$ are determined by the modulus of the corresponding vector K_h and the rms displacement $u_{0j} = \langle \mathbf{u}^2 \rangle_j$. The proposed fitting procedure is based on the variation of u_{0j} values. This procedure was realized by a computer program for the joint fitting of three diffraction curves of various reflections. Using the model with a single set of parameters, we succeeded in simultaneously describing the X-ray rocking curves of the (004), (113), and (115) reflections with $\chi^2 = 2.7$. As a result, the values of parameters of the heterostructure were refined; in particular, the quantum well was characterized by l_2 = 11.7(1) nm, $\Delta a_2^{\perp}/a$ = 0.89(1)%, and $u_{02} = 0.007(2)a$.

Conclusions. By jointly fitting the parameters of three X-ray rocking curves, it is possible to restore the profiles of $\Delta a_j^{\perp}/a$ and u_{0j} in the vicinity of a quantum well and, simultaneously, to evaluate the anisotropic distribution of the chaotic displacement $\mathbf{u}$ both in the plane and in the normal direction. The results will be published in a forthcoming paper.

Acknowledgments. The authors are grateful to Yu.F. Sadof'ev for kindly providing the samples for investigation and to V.A. Bushuev for his interest in this study and constant attention.

This study was supported by the Ministry of Industry, Science, and Technology of the Russian Federation (State Contract no. 37.029.1.1.0034) and by the INTAS Foundation (grant no. 01-0190).

REFERENCES

1. P. J. Burgeat and D. Taupin, Acta Crystallogr., Sect. A **24**, 99 (1968).
2. R. N. Kyutt, P. V. Petrashen, and L. M. Sorokin, Phys. Status Solidi A **60**, 381 (1980).
3. P. V. Petrashen', Fiz. Tverd. Tela (Leningrad) **16**, 2168 (1974) [Sov. Phys. Solid State **16**, 1417 (1974)].
4. V. S. Speriosu, M. A. Nicolet, J. L. Tandon, *et al.*, J. Appl. Phys. **57**, 1377 (1985).
5. A. M. Afanas'ev and S. S. Fanchenko, Dokl. Akad. Nauk SSSR **287**, 1395 (1986) [Sov. Phys. Dokl. **31**, 280 (1986)].
6. J. A. Golovchenko, B. W. Batterman, and W. L. Brown, Phys. Rev. B **13**, 2524 (1976).
7. A. M. Afanas'ev and V. G. Kon, Zh. Éksp. Teor. Fiz. **74**, 300 (1978) [Sov. Phys. JETP **47**, 154 (1978)].
8. A. M. Afanas'ev, M. A. Chuev, R. M. Imamov, *et al.*, Kristallografiya **42** (3), 514 (1997) [Crystallogr. Rep. **42**, 467 (1997)].
9. A. M. Afanas'ev, R. M. Imamov, A. A. Lomov, *et al.*, Mikroélektronika **32** (2), 83 (2003).
10. H. Cramer, *Mathematical Methods of Statistics* (Princeton Univ. Press, Princeton, 1946; Mir, Moscow, 1975).
11. B. K. Vainshtein, *Modern Crystallography*, Vol. 1: *Symmetry of Crystals. Methods of Structural Crystallography* (Nauka, Moscow, 1979; Springer, New York, 1981).
12. A. A. Darhuber, J. Stangl, V. Holy, *et al.*, Thin Solid Films **306**, 198 (1997).
13. R. N. Kyutt, T. V. Shubina, S. V. Sorokin, *et al.*, J. Phys. D **36**, A166 (2003).

Translated by P. Pozdeev